Bragg Scattering on SAR Imagery

A study on detecting Bragg Scattering on Sentinel-1 SAR Imagery over Water Reservoirs in Ghana using Google Earth Engine and Machine Learning

Master Thesis

C.S.H. van Meurs

Delft University of Technology

TU Delft

Bragg Scattering on SAR Imagery

A study on detecting Bragg Scattering on Sentinel-1 SAR Imagery over Water Reservoirs in Ghana using Google Earth Engine and Machine Learning

by

C.S.H. van Meurs

Student Name	Student Number
Cato van Meurs	4569253

Supervisor - 1: Prof. dr. ir. N.C. van de Giesen
Supervisor - 2: Prof. dr. ir. S.C. Steele-Dunne
Faculty: Faculty of Civil Engineering, Delft

Cover: Sentinel-1 SAR Image of Kpong Reservoir, Ghana on the 27th of August, 2021
Style: TU Delft Report Style, with modifications by Daan Zwaneveld

TU Delft

Preface

Before you lies my master thesis on Bragg scattering and the classification and delineation of small and medium water reservoirs in Ghana, using Sentinel-1 SAR imagery and Google Earth Engine.

I would like to sincerely thank my supervisor, Prof. dr. ir. Nick van de Giesen from the Water Resource Management department of the TU Delft, for his help and patience during this process. Similarly, I would like to thank Prof. dr. ir. Susan Steele-Dunne from the Geoscience and Remote Sensing department of the TU Delft for her participation in my thesis committee.

I would like to very much thank my mum and dad for their love, support and encouragement. The same goes for my brothers, Boris and Jan-Bram, for being my friends and confidantes, and my partner Mike for sticking with me during the past five years. And lets not forget about our dog Dushi, with whom I shared a passion for small to medium sized open-water bodies.

Similar words of thanks should be extended to my friends, both the ones I've known since high school and the friends I made here in Delft, with a special shout-out to my friend Feike, who cooked for me, watched Star Trek with me and provided me with the a Marxist view on every socio-economic developments, for nearly every week during the past eight years.

C.S.H. van Meurs
Delft, July 2025

Summary

In the semi-arid regions of sub-Saharan Africa, the reliance on water reservoirs, both small and large, natural and man-made, is great. These reservoirs are often poorly monitored, both in regard to hydro-climatic variables and in terms of water abstraction. Especially for the ungauged basins there is a large need for increased monitoring [94]. The usage of continuous, clear and reliable satellite imagery could help bridge this gap between the need for information and the available imagery. In this context, Sentinel-1 SAR imagery could fulfill this need, especially given its independence from cloud-free conditions, a problem that is present with the optical Sentinel-2 and Landsat imagery. Bragg scattering poses a challenge to the continuity and reliability of the Sentinel-1 SAR imagery: presenting itself as patches with a backscatter intensity similar to the shore and surrounding area, thus making delineation of the water body difficult.

This research thus aims to provide insight into the detection of Bragg scattering over water reservoirs, using the remotely sensed Sentinel-1 SAR data. For this purpose, an open-source code was written that utilizes the freely available Sentinel-1 SAR imagery and the Google Earth Engine platform to execute the classification methodology developed during this research.

The results of this research show that the used method, manner in which data was collected and coding provide reasonably accurate results. Through this research the complexity of Bragg scattering detection was demonstrated: the unbalanced quantity of reference data - due to the low frequency of Bragg scattering occurring, made it difficult to train a classifier that is not biased towards the majority class. Applying an outline-finding algorithm made detection significantly easier, but made the classification process less robust, and was thus not pursued. Usage of a superpixel-based approach, rather than using a pixel-based approach, significancy lessens problems encountered with speckle but leads to increased computation times. To allow the classifier to differentiate between patches of Bragg scattering, unaffected water and surrounding shore, both the VV and VH polarizations were used, as well as Gray Level Co-Occurace Matrix (GLCM) features

Through analysis of results, it has shown that a Random Forest classifier yields the best results, with an Overall Accuracy and Kappa Coefficient score of respectively 0.983 and 0.968. In combination with the SNIC method employed and the computation of mean, median and standard deviation values of each superpixels, it was found that the following bands were of largest importance to the quality of the output: the Sum Average, Correlation and Cluster Shade, as well as the normal VH and VV bands. Especially in the VH polarization, these features showed to be relatively insensitive to Bragg scattering. Apart from the accuracy assessment performed by usage of a confusion matrix, a visual review of the classification result was performed. This confirmed the previous statement that there is a slight tendency for the classifier to be biased towards the majority classes.

Taking all this into consideration, a variety of recommendations were made to the effect of improving the methodology and results of further classification research. Further research was recommended into the possibility of using different forms of accuracy assessment, including the usage of a weighted confusion matrix. The exploration of different manners to assess accuracy is of special importance given the imbalance of the training and validation data available.

Additionally, further research was recommended into the effects of applying speckle filters - e.g. Lee or Refined Lee - early into the process of image processing. Also, further research could be pursued into the filed of using Deep Learning techniques for the detection of Bragg scattering on radar imagery, Sentinel-1 specifically. Past analysis of Deep Learning in regards to water reservoir delineation and LULC (Land Use and Land Cover) classification has shown Deep Neural Networks (DNNs) and Convolutional Neural Networks (CNNs) to be more than capable in handling complex landscapes.

Contents

Nomenclature

Abbreviations

Abbreviation	Definition
ANN	Artifical Neural Network
ASI	Agenzia Spaziale Italiana
ASM	Angular Second Moment
CanVec	Canadian Hydrographic Dataset
CNN	Convolutional Neural Network
CORR	Correlation
CSK	COSMO-SkyMed
DEM	Digital Elevation Model
DENT	Difference Entropy
DISS	Dissimilarity
DN	Digital Numbers
DNN	Deep Neural Network
DVAR	Difference Variance
ECRINS	European Catchment and Rivers Network System
EM	Electromagnetic
ENT	Entropy
ESA	European Space Agency
FCL	Fully Connected Layer
FN	False Negative
FP	False Positive
GD	Gradient Descent
GDP	Gross domestic product
GEE	Google Earth Engine
GIS	Geographic Information System
GLCM	Gray Level Co-Occurance Matrix
GLWD	Global Lakes and Wetlands Database
GNSS	Global Navigation Satellite System
GRanD	Global Reservoir and Dam Database
GRD	Ground Range Detected
HH	Horizontal Transmitting Horizontal Receiving
HV	Horizontal Transmitting Vertical Receiving
IDM	Inverse Difference Moment
IMCORR1	Information Measure of Correlation 1
IMCORR2	Information Measure of Correlation 2
inSAR	Interferometric Synthetic Aperture Radar
ITCZ	Inter Tropical Convergence Zone
IWS	Interferometric Wide Swath
JAXA	Japan Aerospace Exploration Agency
LULC	Land Use and Land Cover
MAXCORR	Maximum Correlation Coefficient
ML	Machine Learning
MODIS	Moderate Resolution Imaging Spectro-Radiometer
MSD	Meteorological Services Department
MSE	Mean Squared Error
MW	Microwave

Abbreviation	Definition
NHD	National Hydrography Dataset
NN	Neural Network
NOAA	National Oceanic and Atmospheric Administration
OA	Overall Accuracy
OBIA	Object Based Image Classification
PA	Producers Accuracy
PROM	Cluster Prominence
ReLU	Rectified Linear Unit
RF	Random Forest
RLOS	Radar Line of Sight
RMSE	Root Mean Squared Error
SAR	Synthetic Aperature Radar
SAVG	Sum Average
SENT	Sum Entropy
SHADE	Cluster Shade
SLIC	Simple Linear Iterative Clustering
SNIC	Simple Non-Iterative Clustering
SNN	Shallow Neural Network
SRTM	Shuttle Radar Topographic Mission
SVAR	Sum Variance
SVM	Support Vector Machine
SWBD	SRTM Water Body Data
TN	True Negative
TP	True Positive
UA	Users Accuracy
UER	Upper East Region
UN	United Nations
VAR	Variance
VH	Vertical Transmitting Horizontal Receiving
VV	Vertical Transmitting Vertical Receiving

1 Introduction

1.1. Background

In the management of sub-Saharan's water resources, (small) reservoirs play a vital role. This is especially the case for the Volta Basin. In the range of water reservoirs out there - small, medium, large - it is the small reservoirs specifically that are of key importance to local communities, being relied upon for irrigation, fishing, livestock watering and other uses. Due to the wide range of uses, these small reservoirs have large potential. They contribute to food security and increase income of the local citizenry [116]. And although these small reservoirs surely offer benefits, there have been increasing concerns about their downsides, such as the higher evaporation rates or problems regarding sedimentation [7].

A comprehensive, cost-effective way of monitoring these reservoirs is required if the actual impact is to be studied. Due to the large number of small reservoirs, ground surveys are expensive, time consuming and labor-intensive. Hence, studies have been performed that employ Remote Sensing, using both optical and radar imagery. Using optical imagery for the monitoring of (small) reservoirs is well established, especially in the Volta Basin [44, 43]. Delineation of water surface area based on optical imagery is a relatively straightforward task, but carries the serious drawback of being limiting to cloud-free days. SAR imagery has the ability to penetrate cloud and smoke cover and allows the acquiring of images to happen independent of daylight [97, 129]. Applying SAR imagery to monitor reservoirs throughout the Volta Basin has been studied through Envisat ASAR imagery, RADARSAT imagery and, more recently, using Sentinel-1 images [8, 89].

Monitoring using SAR data is usually a reliable method, as smooth open water acts as a specular reflector, reflecting a large part of the radar signal away and hence resulting in radar backscatter intensities that are much lower compared to surrounding land, easily allowing for the delineation of open water. Problems arise when Bragg scattering - induced by wind - comes into play. The interaction between wind and open water results in waves that increase the backscatter intensity received over the open water. Similar problems occur over tail ends of the small reservoirs, where vegetation increases backscatter. In that sense, it is clear that no method exist that is completely weather-independent to monitor (small) reservoirs [29, 74].

Yet, automation of reservoir monitoring process is important in the analysis of reservoir dynamics, which in turn allows for better planning and management of the reservoirs. Because Bragg scattering is currently affecting our SAR imagery, this requires the SAR imagery to be manually inspected and vetted, to see if the imagery is usable for delineating reservoirs.

By deriving a method in which Bragg scattering can be flagged on SAR imagery, this would already allow us to automatically select images that are so much affected by Bragg scattering that we can flag them as unusable, without manually inspecting them. Additionally, if a classifier can be designed that is able to differentiate between Bragg scattering, unaffected water and surrounding shore in a manner that is sufficiently accurate, this would allow us to delineate a reservoir effectively even when Bragg scattering is present, simply by vectorizing the classification results and grouping the relevant classes.

Hence, it is is the aim of this study to develop classification techniques to detect Bragg scattering in SAR imagery, which will allow for improved delineation algorithms. For this study, SAR imagery from the Copernicus Sentinel-1 mission have been acquired over Ghana and processed through the Google Earth Engine platform.

1.2. Research Objective

The objective of this study was to develop a SAR based algorithm that is able to detect Bragg scattering patches over open-water reservoirs in Ghana. Based on this main objective, four specific sub-objectives have been formulated:

(i) *Make an overview of existing delineation algorithms and SAR satellite missions*

(ii) *Explore which polarizations and (texture) metrics register Bragg scattering*

(iii) *Test the developed delineation and classification algorithm(s) based on Sentinel-1 imagery*

(iv) *Explore if the developed delineation and classification algorithm(s) can be deployed in the GEE environment*

1.3. Research Questions

Based on the objectives stated above, the following research questions and sub-questions have been formulated:

Can Bragg scattering be detected on Sentinel-1 SAR imagery in order to allow for a higher degree of automation in the monitoring of water reservoirs in Ghana?

1. Have other algorithms for Bragg scattering detection been developed and, if any, to what degree were they successful?
2. What other (texture) metrics are relevant for the detection of Bragg scattering?
3. Which (combination of) polarizations and derived metrics provide the best results?
4. What is the accuracy and what are the limitations of the classification/detection algorithm(s) of the Sentinel-1 imagery?

1.4. Thesis Outline

This thesis is divided into a preface, summary and seven chapters. After this introduction more background information related to this study and SAR is given in chapter 2. In chapter 3 the underlying theory is discussed. Then, the methods and data are discussed in chapter 4, followed by the results in chapter 5, a discussion in chapter 6 and conclusions and recommendations in chapter 7.

In chapter 2 more background related to this study is provided. In section 2.1 the study area specifically will be discussed, followed by a review on reservoirs in 2.2, specifically their history and relevance in the area. In section 2.3 a further review of SAR technology is given, providing information on their general workings, configuration, spatial resolution, polarizations and the Copernicus Sentinel-1 missions specifically. Lastly, information on the Google Earth Engine is provided in section 2.4.

In chapter 3, the theory underlying the research is discussed. In section 3.1, scattering mechanisms are discussed. In section 3.2, information on surface water detection in literature and previous research is considered. Further literature and previous research on reservoirs in radar imagery is discussed in chapter 3.3. Lastly, a review on image segmentation and classification is provided in section 3.5.

In chapter 4 the data used in this study and the developed methodology are discussed. The chapter starts with section 4.1, giving a general introduction. Section 4.2 discusses the study area over which the data has been gathered and for which the algorithms have been trained. In section 4.3 the reference data, including the HydroLAKES database, Sentinel-1 imagery and climate data are discussed. Section 4.4 moves over to the methodology and discusses the conceptual model.

Chapter 5 provides the results of the research, with a quick introduction in section 5.1 and a section on the performance of the different classifiers in section 5.2. In section 5.3, hyper-parameter tuning is discussed. In section 5.4, the relative band importance is reviewed and in section 5.5, the final

performance of the random forest classifier is discussed. Finally, the quality of the computed outline and surface area are discussed in section 5.6 .

In the discussion in chapter 6, section 6.1 discusses the usage of Sentinel-1, with subsection on the performance of the model and the potential of Sentinel-1 data in the given context. In section 6.2 a reflection on the results is provided, specifically focusing on the Sentinel-1 data, the pre-processing steps, speckle filtering, the use of data for classification, the use of SNIC superpixels and the use of the outline-finding algorithm respectively.

Chapter 7 consists of the conclusions and recommendations, with the conclusions presented in section 7.1, going into detail on what the potential of Sentinel-1 SAR data is in the context of mapping Bragg scattering over reservoirs in Ghana, and to which extent the GEE environment is appropriate for this research. In section 7.2 the recommendations are made. Specific recommendations are made for the development of the methodology and recommendations for further research.

2

Background

In this chapter, background information relevant to the study is provided. Firstly, information and context on the study area are provided in section 2.1. Secondly, section 2.2 discusses reservoirs, their sizes, distribution and relevance in the sub-Saharan context. Next, section 2.3 provides an overview on SAR technology and lastly section 2.4 discusses the relevant background to the used platform of Google Earth Engine (GEE).

2.1. Study Area

This research has been performed for the West-African country of Ghana as a study area. The country has a total land area of approximately $240\,000\ \mathrm{km}^2$ and a total water area of $8520\ \mathrm{km}^2$. The population counts approximately 34 million people as of 2023 with an average annual population growth rate of 2.19%. The Ghanian population is overall dominated by youths. Population hotspots are found around the urban areas of Accra, Kumasi, Cape Coast and Tamale, although overall, the country has a relatively low population density of $77\ \mathrm{people\,km}^{-2}$. This population density varies widely across the ten administrative regions, with, by approximation, over 68% living in the country's rural areas and 32% living in the urban areas [38].

Ghana's economy is closely tied to the agricultural sector, with approximately 52% of the labor employed in the sector. The essentiality of the agricultural sector is reflected in the fact that it contributes majorly to the country's GDP and accounts for 40% of the export earnings, while at the same time providing over 90% of Ghana's own food needs. The Ghanian agricultural sector is predominantly traditional and smallholder-oriented, and is principally rain-fed. Overall, the main exports are cocoa, gold, timber, diamonds, bauxite, manganese and hydropower [9, 5].

Ghana has a high average temperature with annual temperatures ranging between 24°C to 30°C, although instances have been recorded where temperatures have varied strongly from that norm, both in the North and the South. Generally, rainfall in Ghana decreases from South to North, with the most southwestern part of Ghana being the wettest, which annual rainfall averaging about $2000\ \mathrm{mm}$. In the drier Northern part of the country annual rainfall does generally not exceed $1100\ \mathrm{mm}$. Ghana has two main precipitation regimes, partitioning the Southern and Northern part of the country. In the Northern part of the country a single maximum regime is applicable, with a wet season from May to October and a long dry season from November to May. In the Southern part of the country the double maxima regime is applicable, with the wetter seasons present from April to July and from September to November. Over the years, the temperatures in Ghana's ecological zones have been rising, while rainfall patterns are generally becoming increasingly erratic [9, 5].

2.2. Reservoirs

Large parts of the semi-arid regions of Sub-Saharan Africa rely on water reservoirs – both large and small – to overcome drought and ensure water availability throughout the year. These reservoirs can be found all throughout Sub-Saharan Africa, but are especially vital in the drier areas of West-Africa.

In this region, the small and medium reservoirs have often existed for many decades, or even longer [94]. In Ghana specifically, the country's independence from Great Britain in the 1960s bench-marked the start of sizable investments regarding small and medium reservoirs. In the years that followed, the popularity of that practice fell and as good as disappeared from the national development agenda. After a hiatus of approximately 30 years, development took off again, driven largely by large-donor investments in the North of Ghana [117].

As mentioned in chapter 1, the introduction, (small) reservoirs play a vital role in sub-Saharan Africa, including Ghana. The relevance of these small reservoirs is tied closely together with range a of challenges the facing the region, including population growth and climate change, which shall be briefly discussed.

According to the United Nations (UN), the population of sub-Saharan Africa is projected to rise from one billion people in 2016 to nearly 2.2 billion in 2050 [107]. In combination with the expected rise in temperature and the growing erraticity of precipitation patterns, the potential threat to water security with regards to people's livelihoods, agriculture, hydropower and the environment has become very real [106, 118]. This vulnerability already came to light during the 2018 Cape Town water crisis, where the city faced a potential water supply disaster, due to a combination of long-term drought, population growth and poor planning and management of water resources and infrastructure.

Interwoven among these threats related to water availability is the fact that in large parts of sub-Saharan Africa water resources are poorly monitored, both in terms of hydro-climatic variables and water usage [60]. Especially with ungauged basins or reservoirs the need for better water management is strongly related to the need for clear, usable and automated (radar)-satellite imagery. This can help provide the data required for better water resource management. In this context, and as will be discussed in further detail later on in this thesis, SAR technology could provide fruitfully.

The definition of what qualifies reservoirs as 'small', 'medium' or 'large' is not universally agreed upon, and throughout different papers and research different definitions are applied. In this thesis, the generic terms 'small', 'medium' and 'large' reservoirs will be qualified as follows: the term 'small reservoir' will be used to define reservoirs with a surface area smaller than $100\ \mathrm{ha}$. Reservoirs with a surface area ranging between $100\ \mathrm{ha}$ and $10\,000\ \mathrm{ha}$ will be regarded as 'medium' and reservoirs with a surface area exceeding $10\,000\ \mathrm{ha}$ are regarded as 'large'. The descriptions are summarized in table 2.1.

Table 2.1: Reservoir description by size

description	**size range** ha
small	<100
medium	100 - 4000
large	>10000

Within Ghana, these qualifications only allow for two reservoirs to be regarded as 'large'. Lake Volta, the largest artificial reservoir in the world (based on surface area), contained behind the Akosombo Dam, with a staggering surface area of approximately $850\,000\ \mathrm{ha}$, and the Bui reservoir in the West, with a surface area ranging between $28\,800\ \mathrm{ha}$ and $44\,400\ \mathrm{ha}$. Due to the enormity of both Lake Volta and the Bui reservoir, these reservoirs will not be examined with regards to the SAR capability to detect Bragg scattering in this thesis.

Within Ghana, it is mainly the North that is populated by a large number of (very) small reservoirs. The Upper East Region (UER) especially has been researched to a great extent [94, 3, 81, 44, 75]. According to Owusu [94], the number of small reservoirs in Ghana alone – his definition being reservoirs with a storage capacity up to $1\,000\,000\ \mathrm{m3}$ – reaches almost a 1000, with a quarter of them located in the UER. The spread of these reservoirs is depicted in figure 2.1. Even more of these reservoirs, 1700, can be found in Burkina Faso, where they too provide water for livestock, irrigation and domestic uses. The focus of this thesis will be on the small and medium reservoirs of Ghana. Within Ghana, the spread of medium sized reservoirs is not contained to a single region, as they can be found all over.

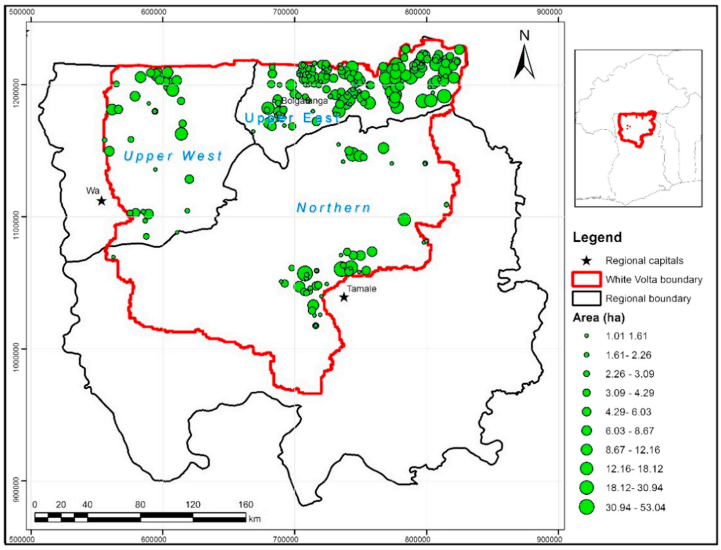

Figure 2.1: Distribution of small reservoirs by surface area [44]

2.3. SAR: Synthetic Aperture Radar

In this study, Synthetic Aperature Radar (SAR) is used to remotely sense and delineate water reservoirs in Sub-Saharan Africa. This section provides a technical background on the workings of SAR and its properties. General working of SAR are discussed in subsections 2.3.2 and 2.3.3. In subsection 2.3.4 the concept of Polarimetric SAR data is considered. In subsection 2.3.5, an overview of previous, current and prospective SAR missions is provided, and finally in subsection 2.3.6, a more detailed disquisition on the Copernicus Sentinel-1 Mission is given.

2.3.1. Introduction to SAR

Discovered in 1954, SAR imaging is a coherent radar system, which records the amplitude and phase of the reflected signal - also known as the 'echo'. As a microwave (MW) remote sensing technique, SAR imaging is used in providing large-scaled 2D images of Earth's surface reflectivity, doing so with relatively high spatial resolution. As an active system, the sensor produces its own energy and subsequently records the energy reflected back, after interaction with the Earth's surface has taken place.

SAR operates in the microwave region of the EM spectrum. Wavelengths used in SAR technology vary per system and mission, but are usually in the range of P-band (65cm) to Ka-band (1.2cm). The Copernicus Sentinel 1A/B system specifically operates in C-band, with a wavelength of 5.54cm.

2.3.2. Configuration and Geometry

In simplified terms, a SAR system consists of a pulsed MW transmitter, an antenna - used for both transmission and receiving - and a receiver unit. SAR is a side-looking system, unlike most optical sensors, which are usually NADIR looking. Hence, the active MW sensors illuminate a swath of land in the ground range direction (x), perpendicular to the flight path (y), which is also known as the azimuth. The antenna beam is directed towards the ground with an angle of incidence θ_0. The direction 'r' depicted in figure 2.2 is hence the radar-line-of-sight (RLOS) [27].

The antenna footprint depicted in figure 2.2 is the area covered by the antenna beam in both the ground range (x) and azimuth directions (y). The size of this antenna footprint is indicated by ΔX and ΔY, and is defined from the antenna apertures (θ_x, θ_y), which in turn are dependent on the wavelength of the transmitted signal and the physical dimensions of the antenna (L_x, L_y). As the spacecraft moves forwards in the azimuth direction, the area is scanned in that same direction, while the radar beam continues to cover the illuminated area in range direction. The area scanned by the antenna beam, as the spacecraft continues to move in azimuth direction, is referred to as the 'radar swath'.

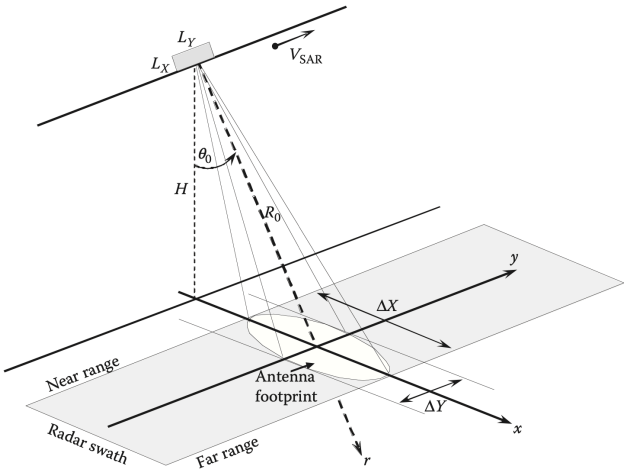

Figure 2.2: SAR imaging geometry in strip-map mode [66]

2.3.3. Spatial Resolution

The spatial resolution is an important quality criteria in any radar system. It describes the system's ability to differentiate between two closely spaced objects and is, as will be discussed further, closely related to the physical dimensions of the antenna. Other factors that determine spatial resolution are the antenna bandwidth and the pulse duration τ. To give an indication on what resolution should be expected: the older ERS-1,2 and ENIVSAT Missions had a ground range resolution of $20\mathrm{m}$. For the Sentinel-1 Mission, using Interferometric Wide Swath (IWS), this improved to $5\mathrm{m}$. The German satellite TerraSAR-X even has a resolution of $1\mathrm{m}$ to $3\mathrm{m}$.

We can discriminate between range resolution and azimuth resolution - intuitively, these terms are the resolution measured in the range and azimuth distance respectively. The (slant) range resolution is given by the following formula, and has the bandwidth as its determining factor.

$$\delta_r = \frac{c}{2B_p} \tag{2.1}$$

δ_r slant range resolution

c speed of light

B_p bandwidth

To translate slant range resolution into ground range resolution, we can scale this equation in the following manner:

$$\delta_r = \frac{c}{2B_p} * \frac{1}{sin(\theta_i - \alpha)} \tag{2.2}$$

θi nominal incidence angle

α local slope

While discussing the azimuth resolution, a fundamentally limiting factor becomes clear. As with any camera or telescope, a radars resolution is limited by the size of the aperture, or in this case, the antenna. For Real Aperture Radar (RAR) systems the relation between aperture size and resolution is given by formula 2.3. The values for r_0 and L_a can be derived from figure 2.3.

$$\delta_a = r_0 * \frac{\lambda_0}{L_0} \tag{2.3}$$

λ_a wavelength of transmitted pulse

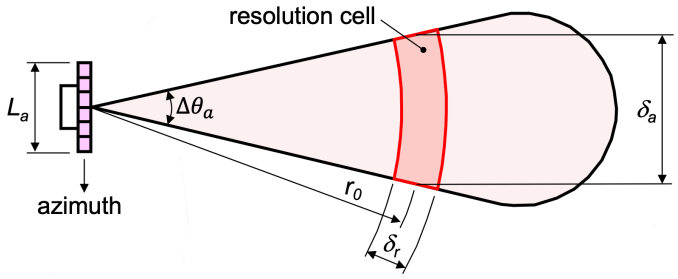

Figure 2.3: Geometry of azimuth resolution

With orbital altitudes of common radar satellites ranging the order of 600km - 800km, usable resolutions in the order of 10m would soon require antennas with lengths of kilometers. This limitation does not apply to optical systems, as they deal with wavelengths much smaller than those found in radar. To overcome this problem, Synthetic Aperture Radar (SAR) was introduced.

Fundamentally, SAR consists of a system that carries many of the standard radar elements, e.g. an antenna, transmitter, receiver and a data collection system with the ability to provide coherent Doppler phase histories. The systems ability to control signal characteristics and record coherent phase information is essential for the construction of high resolution images. Essentially, the low spatial resolutions due to the small aperture is turned to our advantage by the previously described ability to precisely measure phase and Doppler. As the satellite moves in the direction of travel, the beam (directed orthogonal to the travel direction), will illuminate ground objects for an extended period of time. During this time, phase and Doppler information are collected. With the application of the appropriate signal processing, the possibility occurs to synthesize an aperture that is now equivalent to the distance traveled by the actual, physical antenna, while the the location remains in the beam [80]. This distance can be referred to as L_{SA} and is given by formula 2.4

$$L_{SA} = \Delta\theta_a * r_0 = \frac{\lambda_0}{L_a} * r_0 \tag{2.4}$$

L_{SA} Length of the synthetic aperture

Consequentially, the spatial resolution for a given SAR system can now be found through equations 2.5 and 2.6 [27]. As we can see, the azimuth resolution is now independent of range.

$$\Delta\theta_{SA} = \frac{\lambda_0}{2 * L_{SA}} = \frac{L_a}{2 * r_0} \tag{2.5}$$

$$\delta_a = \Delta\theta_{SA} * r_0 = \frac{L_a}{2} \tag{2.6}$$

2.3.4. Polarimetric SAR Data

The term polarimetry refers to the vector nature of the electromagnatic (EM) waves. Radar polarimetry however, refers the polarization state of an EM wave in radar applications. The propagation and interaction with matter of electric (E) and magnetic (M) waves are described by Maxwell's equations [66]. The EM plane wave has both an electric and magnetic component, located in a plane perpendicular to the direction of travel, and can be described as the vector sum of two orthogonal components, typically horizontal and vertical components. These components are characterized by their amplitude and the relative phase between them. When we regard the tip of the vector E of a fully polarized wave and adjust our view to the direction of travel, that tip will trace out a specific pattern. Generally, this trace pattern will show to be an ellipse, as shown in figure 2.4.

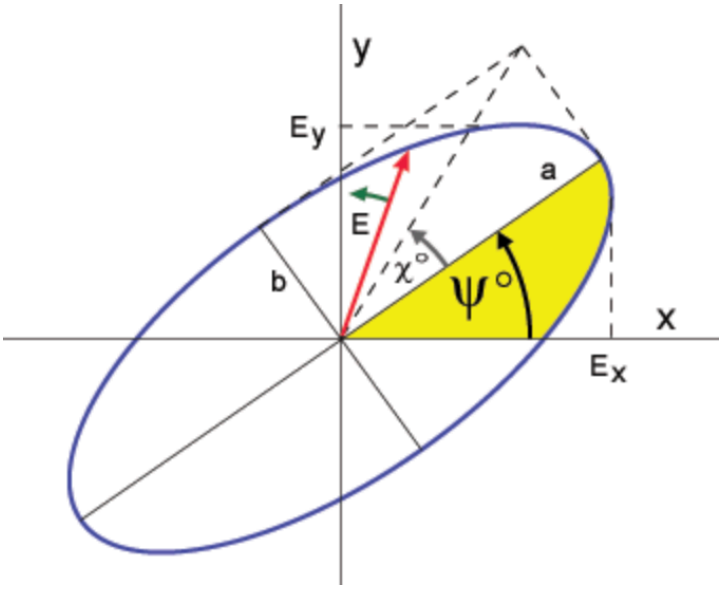

Figure 2.4: Polarization ellipse showing the orientation angle ψ and ellipticity χ [18]

The parameters ψ and χ stand for the orientation angle and the ellipticity of the polarization ellipse respectively. The value of the angle ψ is measured counter-clockwise from the positive horizontal axis (x) to the semi-minor axis (a), as can be seen in figure 2.4, and ranges between $0°$ and $180°$. The parameters χ determines the degree to which the ellipse is actually oval and ranges between $-45°$ to $-45°$. Illustratively, a polarization ellipse with an ellipticity of of $\chi = 45°$ will present as a perfect circle, whereas an ellipse with $\chi = 0°$ will show as a straight line.

Radar systems use antennas designed to both transmit and receive EM waves of specific polarizations. To be able to create waves with a certain polarization, signals with two orthogonal components are required: horizontal (H) and vertical (V). Since interaction with a scatterer can lead to a change in the polarization state of a signal, the antenna is often designed to receive the different polarization components of the EM wave simultaneously. A radar system with the ability to receive and transmit both horizontal and vertical polarization will use the denotation in table 2.2 for each of it's channels.

Table 2.2: Polarization Channels

HH	horizontal transmit and horizontal receive
VV	vertical transmit and vertical receive
HV	horizontal transmit and vertical receive
VH	vertical transmit and horizontal receive

HH and VV shall from now on be referred to as 'like-polarized', while VH and HV shall be referred to as 'cross-polarized'. Using these denotations we can describe a radars systems polarization complexity in the following manner:

- Single Polarized: HH or VV or VH or HV
- Dual Polarized: HH and HV, VV and VH or HH and VV
- Quad Polarized: HH, HV, VH and VH

As mentioned previously, interaction with a scatterer might result in a change of polarization and intensity between the transmitted and received wave. The scattering process that takes place a the scattering target can be described by means of the scattering matrix S, which is provided in equation 2.7.

$$\begin{bmatrix} E_h^s \\ E_v^s \end{bmatrix} = \begin{bmatrix} S_{HH} & S_{HV} \\ S_{VH} & S_{VV} \end{bmatrix} * \begin{bmatrix} E_h^i \\ E_v^i \end{bmatrix} \tag{2.7}$$

The matrices in equation 2.7 describe the transformation of the incident wave to the scattered wave. Note that the elements of the scattering matrix are complex in nature. This allows for a phase change, that may occur during the scattering process, to be well-represented.

2.3.5. Spaceborne SAR Missions

Figure 2.5 provides an overview of historical, current and future spaceborne SAR missions, and sorts them in terms of bandwidth. A larger version of the image is provided in appendix A. The extensive list of SAR missions can also be classified in terms of agency. The European Space Agency (ESA) deserves some special recognition in this regard [99]. ESA's strategic planning can be classified into roughly three pillars: Copernicus, Meteorology and Earth Explorer. The focus of this thesis lies within the Copernicus program. The Copernicus program is an EU program with the aim to monitor and forecast the state of the environment on land, sea and in the atmosphere. The program consists of the respective Sentinel satellites, of which Sentinel-1 and Sentinel-2 are arguably the most famous, and a set of additional contributing missions.

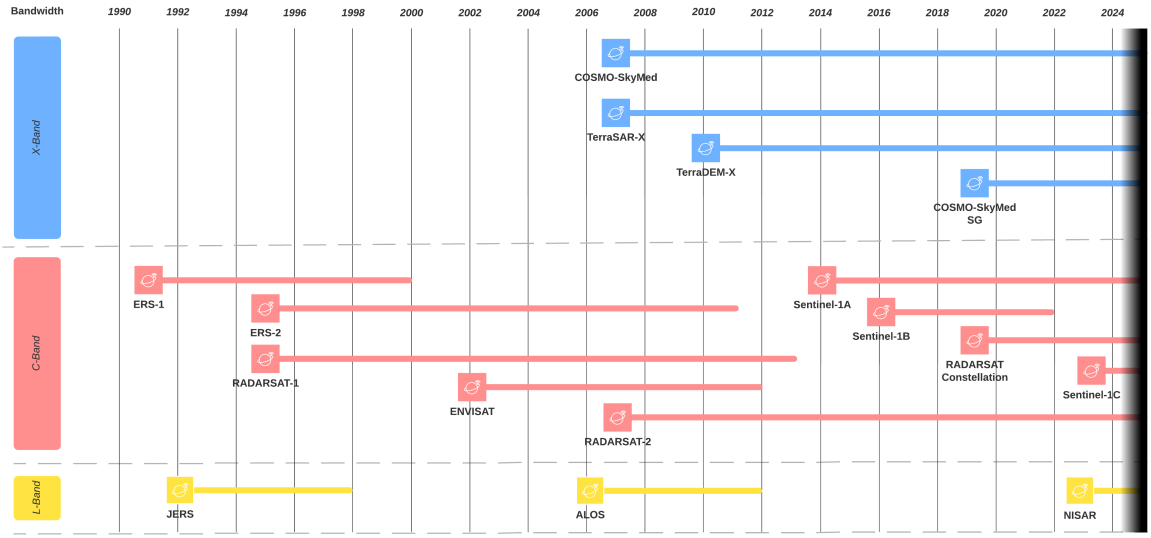

Figure 2.5: Overview of historical, current and future SAR Missions [99]

With regard to SAR, Sentinel-1 is the workhorse of the Copernicus program. Sentinel-1A was launched on the 3rd of April, 2014, and is still in function, surpassing its expected mission duration of seven years. Sentinel-1B was launched approximately two years later, on the 25th of April, 2016, but unfortunately a loss of data transmission occurred at the end of 2021. A power issue was found to be the root cause of the satellites trouble, and on the 3rd of August, 2022, it was announced that the efforts to recover the mission would end [36].

Designed to be a continuous and reliable source of C-band imagery, Sentinel-1 works in a pre-programmed conflict-free operation mode, ensuring reliability of the data production and enabling the growth of a consistent long term data archive [95]. In that spirit, the Sentinel-1 data is freely available via the Open Access Hub, Google Earth Engine (GEE) or by other mirror data facilities. Additionally, ESA has produced an open source toolbox for the different Sentinel products: the Sentinel-Application Platform (SNAP). As of a few years, SNAP has been updated to allow for other sensor products to be processed as well [113].

Regarding Sentinel-1, the C-band SAR is the payload of the mission. The system has an optimal resolution of $5\,\mathrm{m} \times 5\,\mathrm{m}$ with full polarimetric abilities. The polarization modes available in the Sentinel-1 SAR mission are provided in table 2.3. Observation mode, polarization and pass geometry are dependent

Table 2.3: Sentinel-1 Modes

Mode	Swath Width	Resolution (m)	Polarizations
Stripmap	$\succ 80\text{km}$	$5\,\text{m} \times 5\,\text{m}$	HH-HV, VH-VV
IWS	$\succ 250\text{km}$	$5\,\text{m} \times 20\,\text{m}$	HH-HV, VH-VV
EWS	$\succ 400\text{km}$	$20\,\text{m} \times 40\,\text{m}$	HH-HV, VH-VV
Wave Mode	$20\,\text{m} \times 20\,\text{m}$ vignettes with 100km spacing	$5\,\text{m} \times 5\,\text{m}$	HH-VV

on location. Figure 2.6 provides an overview on those. For the country of Ghana specifically, an ascending pass in IW mode, with dual polarizations (VH-VV) can be expected, with a twelve-day repeat cycle.

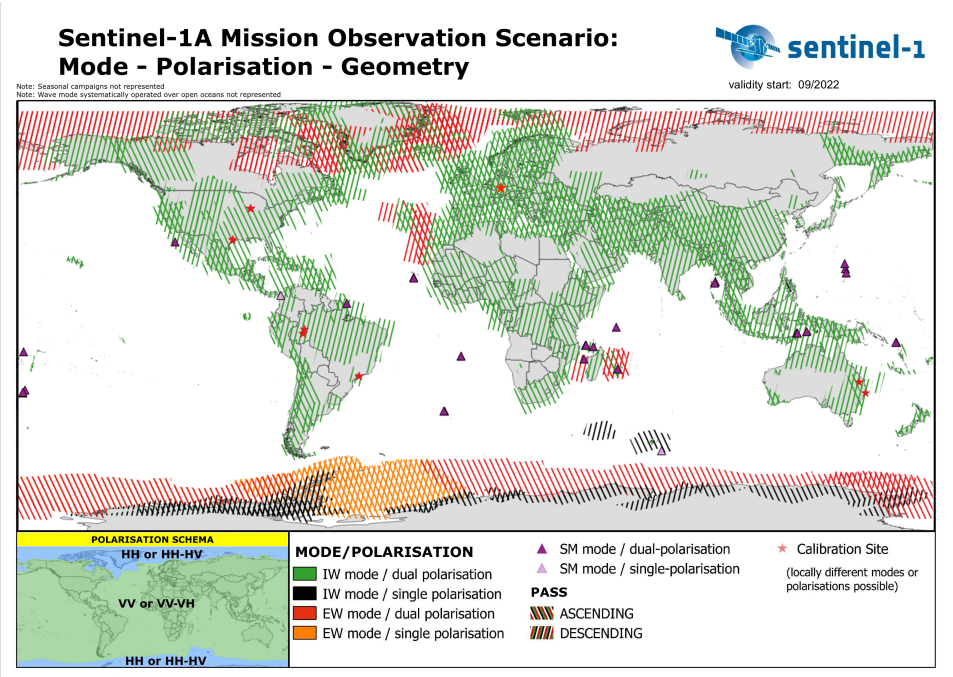

Figure 2.6: Sentinel-1A Coverage, Mode, Polarization and Geometry [37]

ESA is not the only agency to launch and operate spaceborne SAR missions. The German Aerospace Center (DLR) has a variety of satellites currently in operation, with TerraSAR-X and TanDEM-X as their most important projects. Their primary payloads are X-band radar sensors with operational modes stripmap, spotlight and scanSAR [35].

The Agenzia Spaziale Italiane (ASI) has a long legacy concerning SAR products too, due to their extensive COMSO-SkyMed (CSK) program. The COMSO-SkyMed constellation consists of four X-band SAR satellites, launched between 2007 and 2009. As with TerraSAR-X and TanDEM-X spacecrafts, the constellation operates in stripmap, spotlight and scanSAR, with full polarization opportunities [99]. Currently, ASI is focussing on the second generation of COSMO-SkyMed satellites, which were launched in 2019 (CSG-1) and 2022 (CSG-2). With the launching of the second generation of COSMO-SkyMed satellites, the ASI is aiming to enhance the quality and capabilities of imaging of the original COSMO-SkyMed spacecrafts [32].

Outside of Europe, the Japan Aerospace Exploration Agency (JAXA) has also developed spaceborne SAR sensors. Their main focus has been L-band frequencies, with the JERS-1 satellite being launched first in 1992, followed by ALOS and ALOS-2 in 2006 and 2014. The ALOS-4 was launched July 1st 2024 [99]. ALOS-4 replaced the current ALOS-2 mission and has an improved sensor, with much larger swath widths, higher resolution and better coverage [31].

2.3.6. Copernicus Mission

The Copernicus mission is the Earth observation component of the EUs space program. The program is managed by the European Commission and is implemented together with the ESA, alongside a long list of other partners. In this research, the focus will lay with the space component of the Copernicus program, which currently comprises of several Sentinel missions, of which the Sentinel-1 (Sentinel 1A and 1B) and Sentinel-2 (Sentinel 2A, 2B and 2C) missions are the best known. The Sentinel-1 mission initially consisted of the 1A and 1B satellites. Sentinel-1B was retired due to a power supply issue in late 2021. The Sentinel-1C sattelite was launched December 2024. Additionally, the Sentinel-1D satellite is in development [33].

2.4. Google Earth Engine

Over the past decades, large archives of remote sensing data have become available, both through U.S. Governmental agencies such as NASA, the U.S. Geological Survey and the National Oceanic and Atmospheric Administration (N.O.A.A.), and via the ESA. Unfortunately, taking advantage of these resources requires considerable technological expertise and effort, limiting the opportunities of the many researchers who do not have access to high-performance computing resources. Google Earth Engine is a cloud-based platform that allows its users to visualize and analyze satellite imagery and other geospatial, environmental and socio-economic datasets, such as landcover, DEMs or population distributions [48].

In GEE, only the Sentinel-1 Ground Range Detected (GRD) product is available, not the Single Look Complex (SLC) product. Both GRD and SLC are two common SAR data formats. GRD data represents the detected amplitude, while SLC preserves both amplitude and phase. With GRD, the data is stored as real numbers representing the intensity of the signal, whereas SLC data is stored as complex numbers. SLC is typically used for applications requiring phase info, such as interferometry, while GRD data is preferred for mapping and classification, as its easier to process and comes in smaller file sizes.

In this thesis, the Sentinel-1 GRD product will be used for analysis. The GEE catalog already contains pre-processed the Sentinel-1 radar imagery. To derive the backscatter coefficient σ^0 in dB a number of pre-processing steps were applied, based on the algorithms implemented by the Sentinel-1 Toolbox software [47]. This backscatter coefficient, σ^0, represents target backscattering area (radar cross section) per unit ground area. Due to the fact that these values can vary by several orders of magnitude, it is converted to dB [46]. Each of the pre-processing steps applied by GEE, before data is made available, are discussed below.

2.4.1. Application of the Orbit File

During the acquisition of the imagery, the satellite position is recorded by a Global Navigation Satellite System (GNSS). To ensure the fast delivery of the imagery products, the orbit information generated on-board is stored within the Sentinel-1 Level-1 products. These orbit vectors, contained within the metadata, are generally not very accurate. More precise satellite orbit files are generated afterwards and are generally available within twenty days after data acquisition, with a accuracy smaller than five centimeters [41]. To help improve geocoding and overall processing results, the application of the precise orbit files should be preformed with priority over all other pre-processing steps [87].

2.4.2. GRD Border Noise Removal

Because the Earth's surface is irregular, distortions can appear on the Level-1 images while they are being generated. The border noise removal algorithm was designed to remove the low intensity noise present on the edges of the images [87, 105, 41].

2.4.3. Thermal Noise Removal

Thermal noise is caused by the microscopic motions of electrons, due to temperature and presents itself as the random fluctuations of voltage within the electrical components in the internal circuitry of the satellite. The Sentinel-1 image intensity is distributed by the additive thermal noise, especially in the cross-polarization channel [41]. The thermal noise removal algorithm available in SNAP corrects the inter-swath backscatter discontinuities caused by thermal noise, resulting in more smooth Sentinel-1 imagery.

2.4.4. Application of Radiometric Calibration Values

With the calibration step, the objective is to remedy the signal intensity according to the sensor characteristics and the local incidence angle. The data required to preform this calibration procedure is stored in the metadata of the Sentinel-1 product [87].

2.4.5. Terrain Correction

Generally, the SAR data is sensed using varying viewing angles. As a consequence, images have some degrees of distortions, such as foreshortening and shadows. With terrain corrections, DEM's (the SRTM $30\mathrm{m}$ DEM for latitudes between $60°$N and $60°$S and the ASTER DEM for latitudes larger than $60°$N and $60°$S) are used to correct for these distortions [41].

2.4.6. Conversion to dB

In the last step of the GEE pre-processing workflow, the unitless backscatter coefficient σ^0 is converted to dB, using the logarithmic transformation mentioned earlier and provided again in formula 2.8.

$$dB = 10 * \log_{10}(\sigma^0) \tag{2.8}$$

3

Theory

3.1. Scattering Mechanisms

The echoes received by a radar derive from one or more individual reflections. These echoes represent the resulting signal of many individual scattered waves over the target area. The received signal is presented as a complex value, representing and manipulating two variables - phase and amplitude - as a single quantity. The phase of the radar signal is the number of oscillations that the wave executes between the radar and the surface and back again. The amplitude is a measure of the target reflectance or intensity of the received signal, and is often converted to the backscatter coefficient, sigma nought (σ_0). Sigma nought is sometimes also referred to as the scattering coefficient, and its value depends on both the physical and electrical properties of the reflected material, as well as environmental factors. When it comes to measuring reflectivity, sigma nought was often a favoured descriptor, but current datasets will also use the unit of dB. A low reflectivity will be present as darker tones in the image, while high reflectivity is represented with bright tones [63, 55].

There are multiple types of scattering that can be distinguished, all of which will be discussed below. The first type is **specular reflectance**. This type of scattering generally occurs when reflection occurs according to Snell's law, such that the signal is reflected away from the sensor. This will appear on the radar image as a dark area. Additionally, we have **rough surface reflectance**. Roughness is a relative term in this case, as will be discussed later. Generally, rough surface scattering will occur if the variations in surface height begin to approach the wavelength. As a result of the rough surface, the signal will scatter in all directions, including the direction of the radar sensor, leading a rough surface to generally show up on the radar image in brighter tones. When two smooth surfaces form a right angle, the occurrence of **double bounces** can come into play. Due to the geometric configuration of the two smooth surfaces, the signal bounces twice off the surfaces and the greatest part of the energy is reflected back to the sensor. This type of scattering is usually found in urban areas, where there is an abundance of smooth surfaces at right angles with each other. Interestingly, this type of scattering is also found in flooded areas, where there is standing water present, and upright tree trunks form the geometric angles that lead to double bounces. On radar images, the double bounces will show up as brighter pixels or tones. Lastly, there is **volume scattering**. This is a type of scattering that takes place within a volume or a medium, such as tree canopy or a snow pack. Usually, it consists of multiple bounces and reflections from different components within the volume. This type of scattering is most readily apparent when vegetated areas are imaged at longer wavelengths [57].

Specular reflectance, rough surface scattering and double bounces can be regarded as types of surface scattering, such that the previously mentioned scattering mechanisms can be sorted roughly into two groups: surface scattering and volume scattering. In the former category, the roughness of the surface plays an important role. In general, radar backscatter increases with a rougher surface. The definition of 'roughness' depends on the circumstances under which the image was acquired. Using the Rayleigh criterion, the definition of roughness is dependent on both the wavelength of the transmitted signal and the incidence angle during acquisition. The Rayleigh criterion is provided in equation 3.1 [101].

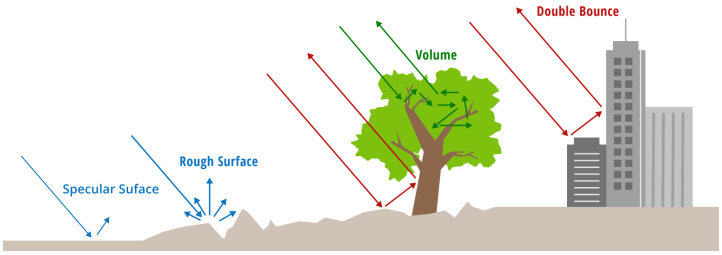

Figure 3.1: Different types of reflection [85]

$$\partial h < \frac{\lambda}{8 * cos(\theta_i)} \tag{3.1}$$

∂h average height of the surface irregularities

λ radar wavelength (cm)

θ_i depression angle

This equation implies that a surface is considered smooth if the vertical relief is lower than ∂h. This line of demarcation appears to be well defined, but in reality a strict, binary demarcation between rough and smooth is not an accurate representation. A varying distinction was proposed by Peake and Oliver [11]:

$$\begin{aligned} \text{smooth when: } & \partial h < \tfrac{\lambda}{25 * cos(\varphi)} \\ \text{rough when: } & \partial h > \tfrac{\lambda}{4 * cos(\varphi)} \\ \text{intermediate when: } & \tfrac{\lambda}{25 * cos(\varphi)} \leq \partial h \leq \tfrac{\lambda}{4 * cos(\varphi)} \end{aligned} \tag{3.2}$$

Another scattering phenomenon that may occur is Bragg scattering. Bragg scattering is a type of coherent scattering that leads to signal enhancement. Bragg scattering can occur if the positions of the scatterers are aligned parallel with the line of flight and are arranged such that their spacing is regular. In that case, and at particular incident angles and system wavelengths, the radar backscatter can be coherently reinforced. This reinforced scattering is what will further on be referred to as Bragg scattering.

The phenomenon was first investigated in 1912 by William Lawrence Bragg and William Henry Bragg, during their work on X-rays [12]. In crystallography, Smith and Thompson defined the condition for Bragg scattering to occur as:

$$2 * (L * sin(\theta) = N * \lambda \tag{3.3}$$

L spacing between the scatterers

N integer

θ incident angle

λ wavelength

This Bragg scattering leads to a total reflected power that is proportional to the square of the number of constituents, which is always greater than that from randomly phased scatterers, for which the total power is proportional only to their number. If Bragg scattering occurs within a resolution cell of a remote sensing radar, then the reflectivity from that cell appears as a small number of Bragg sets, rather than

as a large number of individual scatterers. In other words, under certain conditions, weak individual reflections can add up to a significant echo signal with constructive interference.

Interference is inherent to coherent radar imagery. As a consequence of interference, speckle is observed. Speckle appears as a grainy 'salt-and-peppery' texture in a radar image, caused by random constructive and destructive interference from the multiple scattering returns that will occurs within resolution cells [49]. Constructive interference happens when two waves overlap in such a way that they combine to create a larger wave. Destructive interference happens when two waves overlap in a such a way that they cancel each other out [78]. By conventional standards, speckle is deemed to be an unwanted and dominating noise that degrades the quality of SAR products. In regards to modeling practices, speckle is often simulated as a multiplicative random noise process which is statistically independent of the scene.

3.2. Surface Water Detection

In the field of radar-driven water resource management, water bodies are usually detected due to their characteristic low backscatter. The ability of a radar imaging system to detect surface water depends on both system and surface parameters, and includes (but is not limited to) the roughness characteristic of land and water, changes in the dielectric constant, incident angle and wavelength. Open water is not the only land cover type that is characterized by a low radar return. Sand dunes, bare ground or radar shadows will often show a similar low backscatter intensity as surface water, giving rise to the possibility of confusion. With reservoirs, lakes and ponds, their often characteristic shape can help them make more distinguishable. According to Henderson, however, shape is not the most important parameter in surface water detection, but rather the size and contextual information [55, 56].

Along the shoreline of a water body, there is usually a sharp increase in backscatter intensity. A high contrast ratio can be observed as we look at the line between water and shore, due to the lower backscatter return of the (smooth) water surface and the higher backscatter return of the rougher land. The ability of a radar imaging system to detect surface water depends on both system and environmental parameters. Factors that influence detectability of the surface water include the roughness of both land and water, changes in the dielectric constant, incident angle and the wavelength operated on. In terms of environmental characteristics, the relative relief, slope and conditions of the surface water will all impact detectability too. As a result of that, surface water detectability decreases when the water body is adjacent to bare ground, grassland or shrub-like vegetation. When the water body is juxtaposed with forests land, however, detectability proves much better.

With regards to look angle, a low look angle ($\leq 20°$) will generally result in higher radar returns over water surface, thereby reducing the land/water tonal difference required for detection. Additionally, low look angles increase probability of radar layover. Higher look angles ($\geq 45°$) are generally preferred for the delineation of water bodies, although it does have the downside of increased radar shadowing [55].

3.3. Reservoirs in Radar Imagery

At a first glance, the detection and delineation of water bodies from radar imagery seems like a simple task. There are a range of variables that can hinder the detection of open water, such as the surface roughness of water or a decrease in the land/water contrast [15, 74, 122, 128, 96]. To this date, surface water mapping studies have often been limited to either smaller, specific areas, or require user-intensive methods [15, 123]. In the previous chapter, a rather in-depth discussion on the theory of scattering and polarization was provided. Following ESA's recommendation, a VV polarization mode would be preferred for the detection of open water. Prior research, however, has shown that both HH and HV channels show considerable better results over the usage of a VV channel [17, 74, 16]. Due to specular scatterings predominance over volume scattering, which is low over open water, depolarization is low and we are thus dealing with mainly like-polarized reflections [74]. When delineating water bodies in cross-polarization, backscatter intensities are thus expected to be lower. With regards to the like-polarized channels the VV channel backscatter intensities are expected to be highest.

Wind-induced Bragg scattering effects are normally largest in the VV channel, as it highlights the surface roughness effect through the interaction of the capillary waves [16]. The cross–polarized channels

HV/VH are noticeably less affected by surface roughness. Alsdorf *et al.* found that using L-band radar could limit the effect of Bragg scattering in radar imagery, since the longer L-band wavelengths would lead the signal to be reflected specularly [6]. The presence of Bragg scattering is dependent on both wind direction and velocity, as mentioned previously. Within literature, different wind speed thresholds for Bragg scattering are provided. Liebe *et al.* found that, with C-band ENVISAT ASAR, a wind speed of $2.60\ \mathrm{m\,s{-}1}$ at a height of $2\ \mathrm{m}$ above the surface (or $3.30\ \mathrm{m\,s{-}1}$ at a height of $10\ \mathrm{m}$) was a threshold wind speed for Bragg scattering to occur [74]. Wu *et al.* found that wind speeds of over $3\ \mathrm{m\,s{-}1}$ over the water surface would lead to noticeable surface roughness [122], and Brisco *et al.* came to the conclusion that an approximate value of about $2.78\ \mathrm{m\,s{-}1}$ would serve as a proper threshold [15]. What we can conclude from this is that there is no sharp demarcation threshold, but that the manner in which wind impacts surface roughness is a complex function that takes into account several other facts, such as both the direction of the wind and the radars line of flight and the incident angle at which is measured.

In the detection of water surfaces, smooth surfaces with a similar scattering response - e.g. bare ground, sandy dunes or smooth tarmac - can lead to confusion. The presence of mountains, hills or start slopes in general can also be problematic [74, 19]. [74] found that, in the tail part of the reservoir especially, problems are most prevalent. Especially in the rainy season, when the tail part is expected to be at full capacity, the distinction between open water and the surrounding wetland becomes unclear [74]. This tail part is also were most vegetation is present, which can drastically change the backscatter signature [8]. Sometimes the presence of vegetation can help delineation, e.g. when the shores of the water body are covered with tall reeds, in which case the double bounce scattering on that part will drastically increase the ease of demarcation between water and land.

3.4. Bragg Scattering in SAR Imagery

Bragg scattering and Bragg surfaces are most commonly referred to when discussing sea surfaces on radar images. When we have small, wind-induced capillary waves or short gravity waves, which have wavelengths in the range of millimeters to centimeters, the water surface can act as a Bragg surface. Unlike a random rough surface, the facets of the Bragg surface have a regular pattern. Each facet, at a particular angle, will occur regularly and with the same distance between them. In our case, these facets are the wind-induced waves on the water surface. In other words, the wind blowing over the water surface induces small, regular waves that scatter the transmitted signal much like a rough surface would [121].

On the studied reservoirs, Bragg scattering most frequently presents itself near the boundaries of the reservoirs, often as large patches that cover at least part of the reservoir. Sometimes though, the Bragg scattering patches can cover nearly the entire reservoir. Almost never, the Bragg scattering patches show up at just the center of the reservoir.

Radar wavelength matters here. Bragg scattering on SAR imagery is influenced by the wavelength of the radar system because it occurs when the radar wavelength matches twice the wavelength of the surface waves. So this resonance condition determines which waves contribute most strongly to the backscatter signal. Because of this, radar systems with shorter wavelengths (X-band or C-band) resonate with shorter waves, and longer radar wavelengths (L-band of P-band) resonate with longer surface waves, which we would typically find on the ocean [121].

Figure 3.2 shows the scattering pattern that occurs over a Bragg surface, which is visibly different than the scattering pattern that would occur over a specular surface.

3.5. Image Segmentation and Classification

Identifying water bodies from radar images is not a trivial task, as the images can be complex and noisy, with many other features present. This is where image segmentation and classification techniques come into play. Image segmentation refers to the process of partitioning an image into multiple image segments, regions or objects. The goal of segmentation is to allow for easier and more meaningful image analysis. Image classification, on the other hand, involves assigning a label or category to the segments, object or pixels present in radar images. The goal here is to identify what is presented in the object or pixel(s), and to assign it to a predefined category.

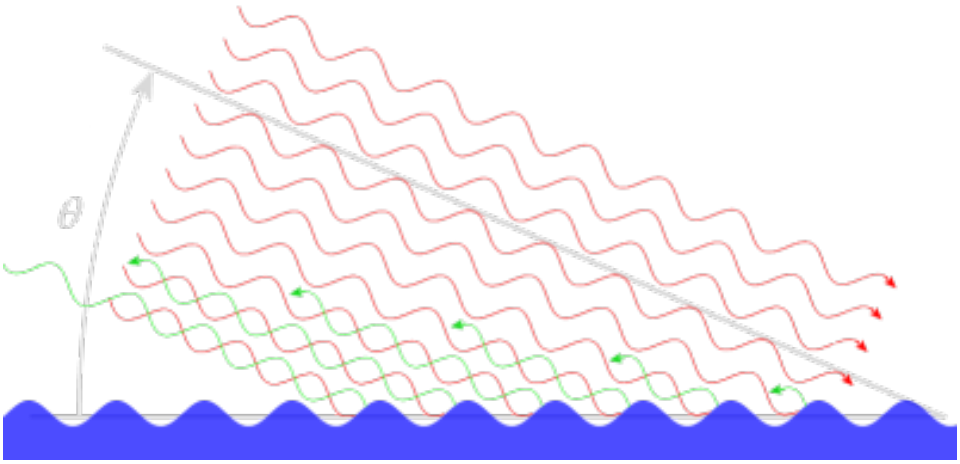

Figure 3.2: Bragg scattering

There are several radar image classification algorithms that can be used to detect water bodies on radar images. The three main types of image classification techniques in remote sensing are:

- Unsupervised image classification
- Supervised image classification
- Object-based image analysis (OBIA)

3.5.1. Threshold Classification

Of these types of classification, unsupervised and supervised image classification are two of the most common approaches. The most commonly used algorithm in water body detection is thresholding. Thresholding is a basic technique to separate objects or regions of interest. The principle behind thresholding is to select a threshold value and compare each pixel value in the image with that threshold value. The selection of an appropriate threshold value is critical to the success of thresholding. A value that is too low will result in too many false positive detections, and in the same manner a threshold value that is set too high will result in too many false negative detections. An appropriate threshold value can be determined using various methods, such as manual selection, statistical analysis or adaptive thresholding. A variety of studies have applied this thresholding technique to the effect of water body detection [19, 16, 109, 128]. Though these studies resulted in generally acceptable results over calmer waters surrounded by rougher vegetation, they did not preform as well under challenging circumstances, such as when wind had increased surface water roughness. This is due to the wind-induced surface roughness of the water, making the backscatter intensity of the water surface to become similar to the backscatter intensity of the surrounding land. This makes it rather difficult to distinguish between land and water, based on SAR imagery alone.

This is in part because the rougher surface caused by wind can produce a texture similar of that land or other surfaces, making it difficult to distinguish between water and non-water areas, based on texture alone.

Generally, thresholding is considered an unsupervised classification technique, as it does not require prior knowledge or training data to segment an image. Rather, thresholding relies on a predetermined threshold value or computed value based on image statistics, and segments the image into two regions based on this value. In this manner, the segmentation is based solely on the pixel values of the image, without any external information or supervision. Additionally, forms or supervised threshold classification was preformed, among others by Henry *et al.* in 2006 and van de Giesen in 2001, in the context of flood mapping and the mapping of flood plains. With this method, a compromise is found between accuracy and the speed at which classification can be delivered. These methods do require a scene- or region-specific approach [15], which makes the methods rather difficult to employ over larger areas, with a certain degree of automation.

3.5.2. Active Contour Modeling

Active contour modeling, also known as 'snakes', is a computer vision technique used to detect and delineate the boundaries of objects or segments in an image. The technique works by defining a contour or curve that can deform and move within the image to find the object boundaries. This technique can be used to identify the outlines and edges of bodies of water. To use active contour modeling for water body detection, a user first selects an initial contour or curve that surrounds the area of interest. The algorithm then iteratively adjusts the contour to minimize an energy function that is defined based on the image data and the desired properties of the contour. The energy function typically includes terms for image gradient, curvature and other factors that influence the shape and position of the contour. Effectively, this corresponds to minimizing the energy integrated over the contour, which often favors smooth contours.

Successful applications of active contour modeling in water delineation have been applied by Horrit *et al.* in 2001, Ahtonen *et al.* in 2004 and Hahmann and Wessel in 2010. It can be a powerful technique in water body detection and delineation, but there are practical considerations, as it can be a computationally intensive and the method is quite sensitive to the choice of parameters. Additionally, a rough map of the water bodies is required to perform initialization of the snake [59, 50].

3.5.3. Support Vector Machine

Support Vector Machines (SVMs) are not so much used ML algorithms in the practice of surface water detection using radar imagery. It is a supervised learning method that separates the classes with a decision surface that maximizes the margin of class boundaries [21, 4]. The objective of the SVM algorithm is to find a hyperplane in a N-dimensional feature space, in which N equals the number of features, that separates the samples of different classes. This hyperplane then functions as a decision boundary, and thus determines to which class a sample belongs to, or which label should be assigned. The training points adjoined to the optimal hyperplane are called support vectors [103]. The SVM classification method is known to be robust for processing noisy remote sensing data and to be highly effective in solving generalization problems not linearly separable [53, 23]. A SVM was previously employed by Pôssa and Maillard to separate water surfaces from land, but only tested the effectiveness of their algorithm under wind-free conditions, [98].

3.5.4. Random Forests

As with SVMs, a Random Forest (RF) is a ML algorithm that can be used for, among others, classification. It is an ensemble method that combines multiple decision trees to produce a more accurate and robust model than a single decision tree could. In this section, we will focus on how RFs function in classification tasks. The RF algorithm works by creating multiple decision trees and combining their productions. A given, arbitrary RF will consist of N individual decision trees. Each decision tree is trained on a random subset of the data and a random subset of the features. This randomness helps to reduce the possibility of over-fitting and improves the accuracy of the model. During training, each decision tree tries to find the best split at each node, based on a previously selected criterion. Examples of that criterion include measures such as information gain or the Gini impurity. The best split is the one that maximizes separation between classes [110].

Once the decision trees are trained, the RF algorithm combines their predictions using a majority vote. This majority vote principle is effective in reducing the impact of individual errors and the production of an overall more accurate prediction. Advantages of the RF algorithm are its ease in usage and interpretation. The training of the RF algorithm can be done using intensity, texture, or other features. The algorithm can handle the noise and variability in the radar data, and its ability to handle unbalanced classes can be useful for detecting small water bodies or areas of partial water coverage. However, the effectiveness of Random Forest for water detection will depend on the quality of the features used and the complexity of the classification [110].

3.5.5. Neural Networks

Artificial Neural Networks (ANNs) are a type of ML algorithm inspired by the structure and function of biological neurons in the brain. It is a complex, non-linear system formed by extensive interconnection of a large number of neurons, with the ability of self-learning, self-organization, self-adaptation and strong non-linear mapping. ANNs consist of multiple layers of interconnected nodes, called artificial

neurons or perceptrons, which process and transform input data to produce output predictions. These attributes make them suitable for solving the problems of uncertain reasoning, judgment, recognition and classification of complex causal relationships [122]. There are three crucial layers in a neural network:

- Input Layer
- Hidden Layer(s)
- Output Layer

Here the input layer consists of the features, or explanatory variables. The hidden layers consists of a finite number of hidden nodes. The basic overview of an ANNs architecture is provided in figure 3.3. In a Shallow Neural Network (SNN), there is only one single hidden layer present. When we refer to a Deep Neural Network (DNN), we are dealing with two hidden layers or more. The data is processed through the input and hidden layers to the output layer, which consists of the target variable, or dependent variable. In the NN, the nodes are connected by weights. In an ANN, these weights can be adjusted for each feature in the evaluation and prediction, to improve recognition methods [122]. If all nodes are connected to each other, we speak of a Fully Connected Network (FCN).

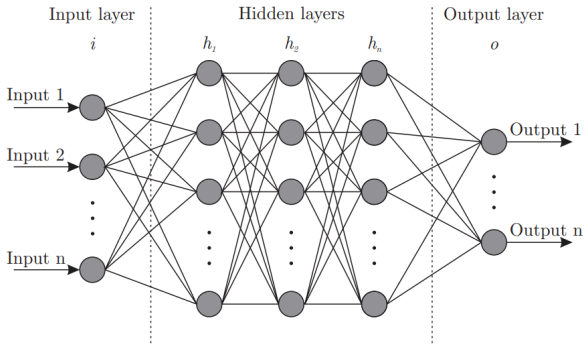

Figure 3.3: Basic Structure of an ANN [13]

In the hidden nodes, the sum of inputs is computed by means of the trainable weights, and a transfer (or activation) function is applied. Such a transfer function can take many different forms, from logistic functions, binary step functions and softsign functions, to Rectified Linear Unit (ReLU) functions, which are commonly used in Convolutional Neural Networks (CNNs). In a SNN, this choice of transfer function does not heavily impact the output result, but this changes as we move onto DNNs. Naturally, the choice for a certain transfer function will impact computational time and costs, which should be taken into account.

The output layer function is in part dependent on the general goal of the algorithm. When used for simple regression, a linear output layer function will suffice. With classification, we can differentiate between binary class classification, in which case a logistic output layer function (Binary Logit) can be applied, and a multiclass classification, in which case a softmax function (Multinomial Logit) will come into play [54, 127, 64].

In the context of optimization, the function used to evaluate a potential model configuration - in the case of ANNs this comes down to a set of weights - is referred to as the objective function or loss function. Typically, with ANNs, we aim to minimize this objective function. The loss function reduces the various good and bad aspects of a complex function to a single value, allowing possible model candidates to be ranked and compared. The loss function can take many different forms. For regression problems, the MSE or RMSE is oftentimes used. In classification, however, the cross-entropy or Hinge-loss can be used. Minimization of the objective function is achieved through training the model, doing so by finding the optimal combinations of weights. Mathematically, this is an ill-posed problem, since ANNs are not uniquely identifiable, and there are numerous sets of weights that give exactly the same output probability distribution for given data.

During training, backwards propagation is often used to tweak the weights. The idea behind this method

is to compute how the total error is generated from each node in each layer, and how the total error would change by changing the weights. Having the derivatives, we can improve the weights layer by layer to move towards the minimum. The optimization algorithms used in training an ANN are chosen by the analyst. Sometimes, Gradient Descent (GD) is used. The analyst can futher refine the ANN setup by tuning of the hyperparameters, such as the batch size and learning rate. Varying the batch size comes down to choosing between stability and robustness, and that in turn comes down to determining the size of a single epoch [54, 127, 64].

Usage of ANNs in the detection of water and objects using radar-based data has been previously applied by Wu *et al.*, Shen *et al.* and Balajee and Durai [122, 109, 10]. In the latter two cases, a specific type of ANN was used: Convolutional Neural Networks (CNNs). CNNs are a type of NN that, contrary to their typical ANN counterparts, use the complete image information and are commonly used in Computer Vision. The need for CNNs comes from the extreme computational expenses required during the processing of full images using ANNs. With ANNs, the amount of weights quickly grow to be massive, even with SNNs and small images, and they do not scale well to actual, full images. This problem is solved by using CNNs, specifically by connecting the neurons in a layer to only a small region of the layer before it, rather than in a fully-connected manner.

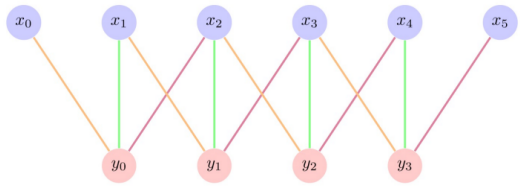

Figure 3.4: Convolutional Layer [71]

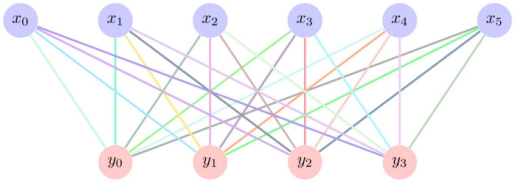

Figure 3.5: Fully-Connected Layer [71]

In essence, they are similar to other NNs, but with the added layer of complexity of using a series of convolutional layers. The workings of such a convolutional layer is discussed further on in this section. CNNs are often used for image recognition and classification tasks. Typical CNN architecture comprises of:

- Input Layers
- Convolutional Layers
- Pooling Layers
- Fully-Connected Layers

In which the Input layer will, as before, hold the raw pixel values of the image. The convolutional layers will compute the output of neurons that are connected to local regions in the input. The convolutional layers are made up of a set of filters (also referred to as 'kernels') that are applied to the input image. The extensive stacking of convolutional layers can be used to create complex models, able to learn more intricate features from images. The Pooling layers are a type of convolutional layer, used to preform a downsampling operation along the spatial dimensions of the input. As such, the application of pooling layers helps the reduction of the number of parameters and as such makes the training faster. Finally, the Fully-Connected layer is used to take the features learned by the previous layer and translates them to predictions on class types. These FC-layers are one of the most basic types of layer in the CNN. As with the common ANN, each neuron in this layer will be connected to all the neurons in the previous volume. With this type of NN, we can achieve the task of single image classification. This is, however, insufficient for the detection of water bodies in radar images, as it only allows for the entire image to be classified as a single class. This single-object classification can be taken one step further to achieve localisation too, meaning that a bounding box can be defined to locate the single object in the image. With multiple objects present in an image, object detection can be achieved. Finally, with image segmentation, the algorithm is able to classify each pixel in the image. This is the level of complexity that needs to be reached if consistent detection of water bodies is required on radar satellite images [71]. The differences between these techniques are illustrated below.

With image segmentation, the architecture starts to be fundamentally different from the regular CNN-

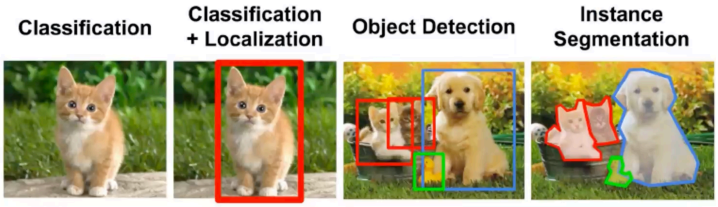

Figure 3.6: Classification Techniques [71]

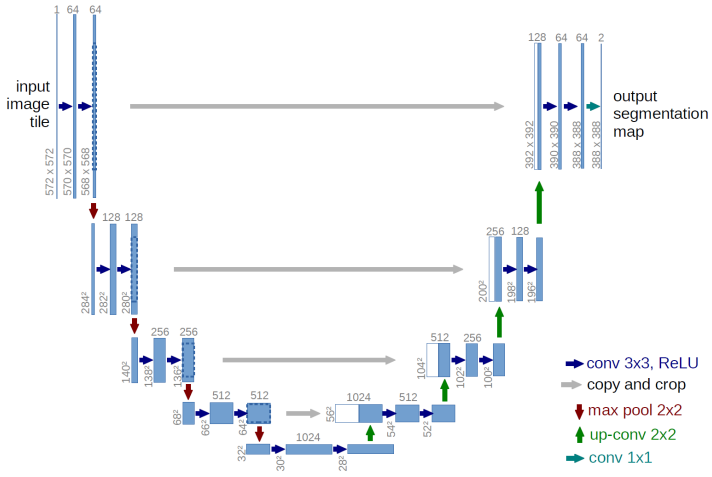

Figure 3.7: U-Net Architecture [102]

ConvNet architecture discussed before. An example of such a CNN is U-Net, originally developed to detect cell boundaries in biomedical images [102]. The architecture contains two substructures: a classic downsampling (encoding) path and a consequent upsampling (decoding) path. The encoder structure follows a traditional stack of consequent convolutional and pooling layers. The decoder structure uses convolutional and unpooling layers, and simultaneously applies concatenations between both branches to directly copy from the downsampling to the upsampling path. The concatenations are preformed to add location information to the upsampled image and aids in localising details in the image. An overview of the U-Net architecture is provided in image 3.7. As can be seen, there are no dense (fully-connected) layers present, meaning that images of different sizes can be used as input without increasing or decreasing the amount of trainable parameters. The only parameters to learn on the convolutional layers are the kernels. The result is thus a per-pixel classification, but due to the addition of the convolutions, the network has been trained to take into consideration edges, patterns and, generally, context [71].

4

Data and Methods

4.1. Introduction

The main algorithm applied in this thesis is a of supervised classification algorithm with the aim to take Sentinel-1 SAR imagery and, based on those images, differentiate between surface water affected by Bragg Scattering and unaffected water surfaces on selected water bodies. Supervised classification is a process that consists of the following stages:

- Class Definition
- Pre-Processing
- Algorithm Training
- Image Classification
- Accuracy Assessment

Firstly, the specific aspects of the study area will be discussed in further detail. Next, the process of class definition and the construction of a training dataset will be elaborated on in the section 4.3. The various sets of polygon data and satellite products, as their required pre-processing steps are defined under the sections on satellite data, reference data and pre-processing. The methodology applied during the process steps is broadly depicted in figure 4.1 and can be viewed in larger dimensions in appendix B, where the entire diagram is shown, as well as the three separate parts separate from each other, so that it is easier to read.

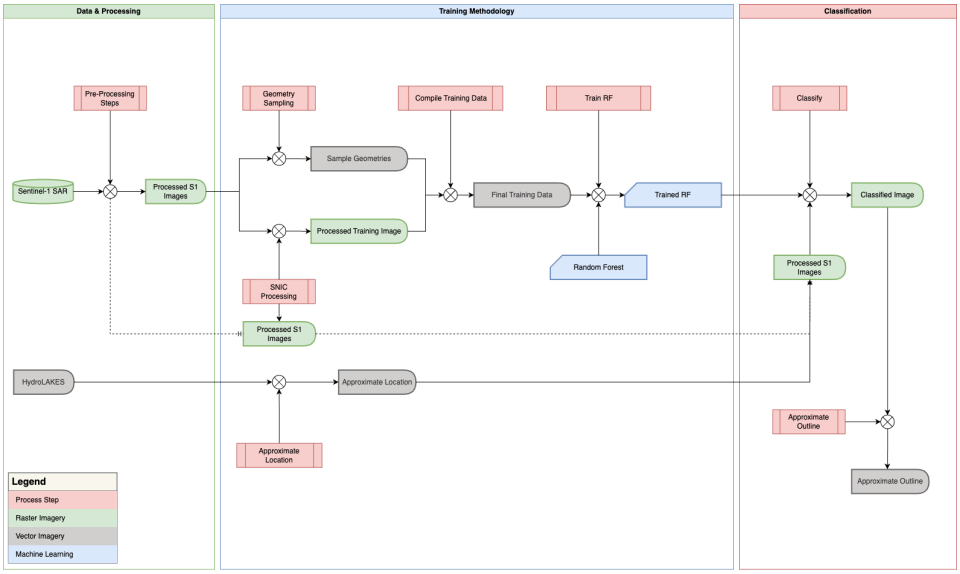

Figure 4.1: Conceptual Methodology

4.2. Study Area

General information on the study area has been presented in section 2.1. More in-depth information, with more relevance to the context of the study, will be provided here. This pertains specifically to data on precipitation patterns and dominant wind regimes throughout the country. As previously used by Owusu and Waylen [92, 93], Ghana can be partitioned into four main agro-ecological zones, as shown below in image 4.2.

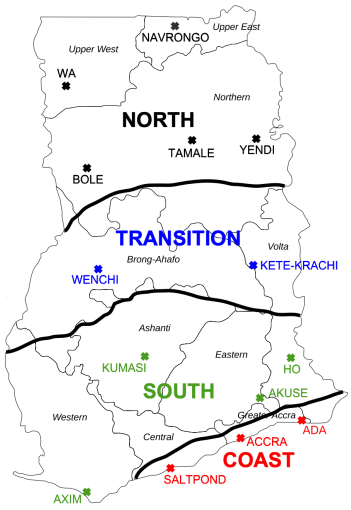

Figure 4.2: Main Agro-Ecological Zones [92, 93]

4.2.1. Precipitation

Ghana presents with different precipitation regimes throughout, generally along the North-South axis. The North-South orientation of these regimes is in most part defined by the movement of the Inter-Tropical Convergence Zone (ITCZ), which brings the African Monsoon. This gives rise to a uni-modal precipitation distribution in the North and a bi-modal precipitation distribution in the South. The uni-modal precipitation distribution in the Northern part of the country shows a single rainy season, followed by a long dry period. Prior to the rainy season, precipitation shows to build up gradually to a maximum, which generally occurs in August/September, as the rain-bearing tropical maritime air mass reaches

the area. Following this peak, as the drier North-Eastern trade winds start to dominate, the dry season enters, lasting from November until early March [79].

In the Transitional zone a longer rainy season is observed, reaching its relatively low maximum in June till September. In the north and coastal zone, the bi-modal precipitation pattern is observed. In both zones the start of the first monsoon occurs around April, with the maximum peak reached around June. Additionally, a much smaller peak is observed around October [79].

4.2.2. Wind

Traditionally, wind data in Ghana is measured by the country's Meteorological Services Department (MSD), who conducts measurements at their 22 stations across the country. On a more local level, the TAHMO organisation has a large number of local weather stations spread across the country, many of which also measure wind speeds [45]. Additionally, the Global Wind Atlas provides a GIS web-interface which helps identify high wind areas and can offer additional insight in wind orientation and speed throughout the day, month or year [26].

Following the same partitioning as previous, general differences pertaining to wind characteristics between the North, Transitional, South and Coastal zone can be described. Generally, in each zone a similar wind speed profile throughout the day can be observed, with peaks in the night till early morning (midnight till 6 AM) and lows from midday till early night. Only in the coastal zone a different pattern is observed, with peaks between midday till midnight and lows from early morning till just before midday. Average indexed wind speeds for each month and region are plotted in figures 4.3, showing a much more varying pattern between the zones.

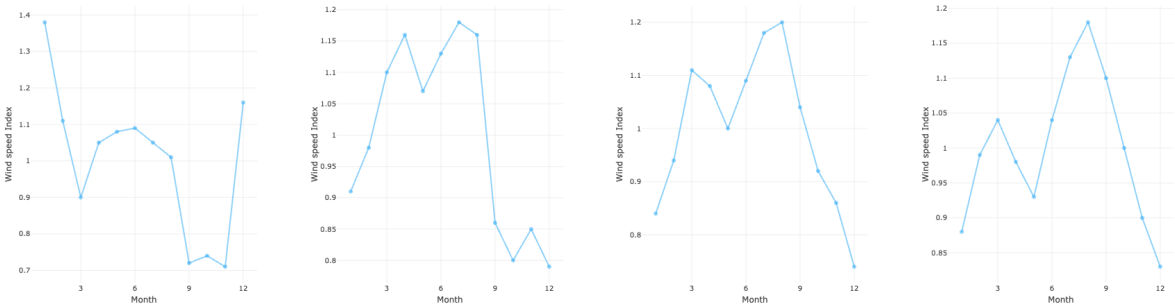

(a) Northern Zone **(b)** Transitional Zone **(c)** Southern Zone **(d)** Coastal Zone

Figure 4.3: Average Wind Speed per Zone

4.3. Reference Data

4.3.1. HydroLAKES

To gather information on the location, size and type of reservoirs in Ghana, the HydroLAKES database was used. The HydroLAKES database is part of the larger HydroSHEDS project and aims to provide the shoreline polygons of all global lakes with a surface area of at least ten hectares. The database has been constructed using a wide range of auxiliary data sources of lake polygons and gridded lake surface areas [61, 84]. Additionally, a number of hydro-environmental characteristics are provided. The datasets used in the creation of the HydroLAKES database are listed in table 4.1.

Table 4.1: Datasets used in the creation of HydroLAKES

Original dataset	Region	Format	Original Resolution	Reference	Number of lakes
Canadian Hydrographic Dataset (CanVec)	Canada	Vector	1:50 000	[88]	863 550
Shuttle Radar Topographic Mission (SRTM) Water Body Data (SWBD	50°S - 60°N	Raster	30m (vectorized and smoothed)	[111]	282 571
MODerate resolution Imaging Spectro-radiometer (MODIS) MOD44W Water Mask	Russia (>60°N)	Raster	250m (vectorized and smoothed)	[20]	167 435
US National Hydrography Dataset (NHD)	Alaska	Vector	1:24 000	[114]	58 496
European Catchments and Rivers Network System (ECRINS)	Europe (>60°N)	Vector	varying resolutions	[34]	50 699
Global Lakes and Wetlands Database (GLWD)	World	Vector	1 :1 000 000	[69]	3023
Global Reservoir and Dam Database (GRanD)	World	Vector	1 :1 000 000 or better (varying)	[70]	1133
Other/Own mapping	World	Vector	1:1 000 000 or better (varying)	n/a	781
Total					

For the region of interest, the Shuttle Radar Topographic Mission (SRTM) and the SRTM Water Body Data (SWBD) were the primary source of information. The HydroLAKES shoreline data was used primarily in two process:

- restricting the areas where in training data was created
- input in outline finding process

These processes with will be discussed in further detail in section 4.4 on methodology.

4.3.2. Sentinel-1

The technical details on inSAR radar technology have been discussed previously in chapter 2. As mentioned, this research primarily uses Sentinel-1 radar data. The Sentinel-1 data provided through the GEE platform is available from 2014 onward till present and is provided in GRD scenes. The pre-processing steps discussed previously are applied by Google Earth Engine itself, previous to making the data available to the user.

To train the algorithm, Sentinel imagery with various patches of Bragg scattering was acquired. As to accomplish this, scenes from 2018 up to and including 2022 over the water bodies Bosomtwe, Kpong, Buntanga, Vea, Tono and Barekese were acquired. Before the equipment failure of the Sentinel-1B satellite in December 2021, this amounted to approximately 59-61 scenes per calendar year. Since the Sentinel-1B failure, this number has been reduced to an approximate number of 29 scenes per calendar year per location. The locations of these selected water bodies are depicted below:

Figure 4.4: Locations of Water Reservoirs used for database

Especially over Kpong, Bosomtwe and Bui a larger amount of Bragg patches were collected. The table below shows the number of Bragg scenes per location. In total, a number of 1793 images were processed as to acquire a total of 41 Bragg-flagged images. Table 4.2 provides an overview of recorded instances where Bragg scattering was present.

Table 4.2: Recorded Bragg Instances

Date	Location	Date	Location
2018-03-22	Bosomtwe	2019-07-09	Barekese
2018-07-20	Bosomtwe	2020-05-28	Barekese
2018-09-06	Bosomtwe	2020-10-13	Barekese
2018-09-30	Bosomtwe	2021-01-29	Barekese
2019-03-29	Bosomtwe	2021-02-16	Barekese
2019-04-16	Bosomtwe	2021-03-24	Barekese
2019-06-15	Bosomtwe	2021-04-17	Barekese
2019-06-27	Bosomtwe	2020-09-30	Bui
2020-05-10	Bosomtwe	2021-09-13	Bui
2020-05-28	Bosomtwe	2022-03-24	Bui
2020-10-19	Bosomtwe	2018-05-27	Kpong
2020-12-12	Bosomtwe	2018-09-18	Kpong
2021-01-29	Bosomtwe	2018-10-12	Kpong
2021-02-16	Bosomtwe	2019-02-27	Kpong
2021-03-06	Bosomtwe	2019-10-25	Kpong
2021-07-22	Bosomtwe	2020-03-05	Kpong
2021-10-02	Bosomtwe	2021-08-27	Kpong
2022-03-19	Bosomtwe	2020-05-04	Tono
2022-03-31	Bosomtwe	2020-05-10	Tono
2020-05-10	Vea	2020-05-10	Voggo
		2021-08-21	Voggo

4.3.3. TAHMO Climate Data

As mentioned in section 3.3, there is no clear demarcation threshold at which wind speed is indicative of Bragg scattering. In varying studies, varying thresholds were mentioned, all ranging around $3.0\ \mathrm{m/s}$. The TAHMO climate data was put next to the imagery showing Bragg scattering, to see if their readings could be an indicator of the presence of Bragg scattering. To this extent, for the water bodies selected and previously mentioned in table 4.2, the average wind speeds and maximum windgust speeds were collected for the closest day and time at the nearest measuring location.

4.4. Conceptual Model

In the conceptual model below the workflow, made concrete by the GEE scripts provided, is depicted. Roughly, the workflow can be divided into five sub-processes:

1. Creation of training polygons
2. Creating of training datasets
3. Classification
4. Outline Finding
5. Accuracy Assessment

4.4.1. Creation of training polygons

Essential for the performance of the classification algorithm is the creation of a qualitative training set. Bragg scattering is a phenomenon that - in the context of water delineation - has been mentioned mostly due to its interference in such a process. A comprehensive database of Bragg scattering imagery, such as exists for e.g. hand writing recognition, object detection or breast cancer detection [65, 76, 120], is not available. As the goal of classification is to distinguish surface water affected by Bragg scattering from water surfaces unaffected by Bragg scattering, a first step of the supervised classification process is to identify the different classes to be identified. In order for the algorithm - later to be discussed - to accurately quantify the linkages between patterns, a large and high-quality dataset is required.

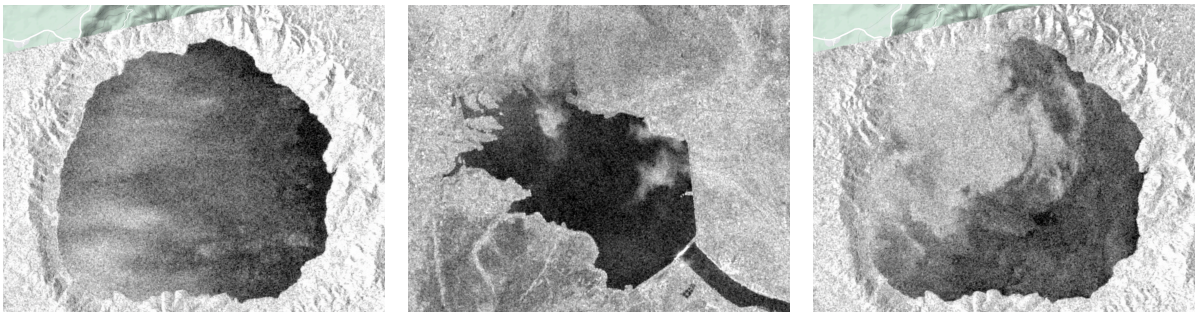

(a) Bosomtwe 2020-05-28 **(b)** Kpong 2021-08-27 **(c)** Bosomtwe 2022-03-19

Figure 4.5: Example imagery (VV) to be Flagged for Bragg Scattering

As a first step in the process of creating a training database, visual inspection of a wide range of Sentinel-1 images was preformed. During this process, images that show obvious signs of Bragg scattering are flagged and saved, as to be used later. Three examples of flagged images are depicted in figure 4.5.

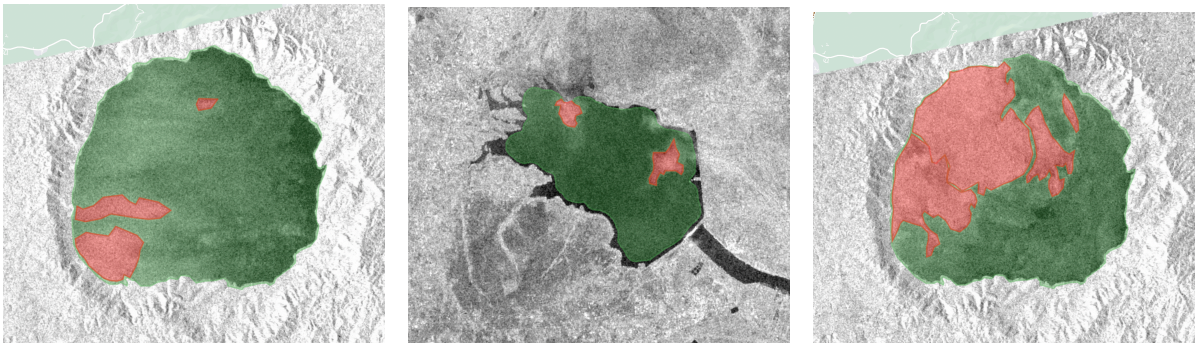

(a) Bosomtwe 2020-05-28 **(b)** Kpong 2021-08-27 **(c)** Bosomtwe 2022-03-19

Figure 4.6: Bragg and Non-Bragg Scattering Sample Regions

The training data is constructed by going through the images, both flagged and not flagged, and creating a polygon of the parts of the water surface that show or do not show Bragg scattering, as well as polygons representing the surrounding area (shore). In this manner, for each image used samples are taken at points that do not show Bragg, points that do show Bragg - given that Bragg scattering is present in the image - and points representing shore. An example of the polygons indicating the locations of Bragg scattering patches and normal water per image are illustrated in figures 4.6a, 4.6b and 4.6c.

Within these Bragg/Water/Shore geometries, points were sampled, for which the location, date and class have been recorded. This information will be combined with the results of the process described in subsection 4.4.2 - Creating of training datasets - later on.

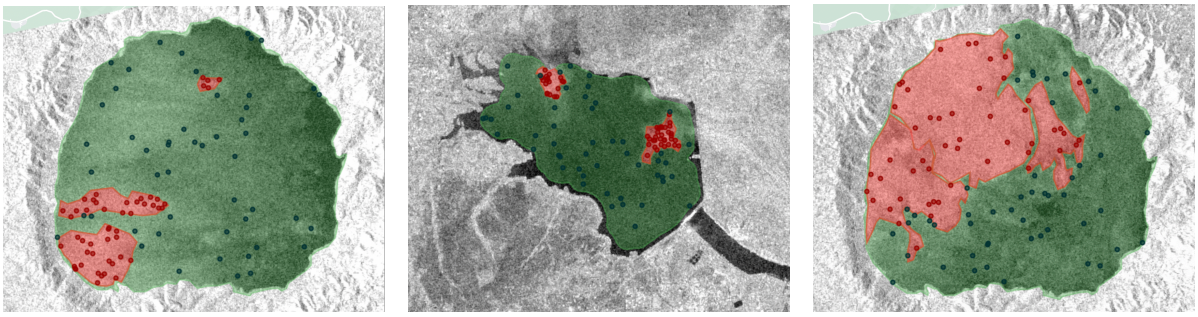

(a) Bosomtwe 2020-05-28 **(b)** Kpong 2021-08-27 **(c)** Bosomtwe 2022-03-19

Figure 4.7: Bragg and Non-Bragg Scattering Samples

4.4.2. Creation of training datasets

Classification is a well-studied and often applied technique. In the previously mentoined studies, satellite and radar imagery were processed using both pixel-based approaches and object-based approaches. With a pixel-based approach, only pixel values are considered. With the object-based approach, segmentation of the imagery is applied, such that the image is segmented into objects on multiple scales. In large-scale studies especially, applying an object-based classification approach has the added effect of a decreased computation time [119, 115].

SNIC Superpixels

Testing shows that simply using a Sentinel-1 VV and VH dataset is not adequate as to effectively train an algorithm in detecting Bragg scattering over a water surface. To this extent, a combination of superpixel clustering based on SNIC (Simple Non-Iterative Clustering) and calculated values such as the statistical mean, median and standard deviation of pixel groups. The SNIC algorithm, developed by Achanta and Süsstrunk, serves as an improved version of the Simple Linear Iterative Clustering (SLIC) superpixel segmentation method [1, 2].

The task of image segmentation, e.g. simplifying an image into small clusters of connected pixels - superpixels - serves as an important (pre-) processing step in object localization, (multi-) class segmentation or object-tracking. The advantages of using superpixels for these processes is that, by applying superpixels, we simplify the image and reduce the number of pixels from millions of pixels to a much, much lower amount of clusters consisting of similar pixels. The advantages of using the SNIC method for superpixel clustering can be summarized by: [1]:

- an algorithm that runs in a single iteration
- it requires less memory than previous clustering methods
- high computational efficiency
- high segmentation quality

SNIC clusters pixels without the use of k-means iterations. The centroids are initialized on a regular grid. The likeness of a pixel to a centroid is measured using a distance in respect to both color and spatial coordinates. To this extent, an algorithm is used that employs both normalized spatial and color distances. As found by Achanta and Süsstrunk, and with a spatial position $\mathbf{x} = [\,x \quad y\,]^T$ and CIELAB color $\mathbf{c} = [\,l \quad a \quad b\,]^T$, the distance of the k[th] superpixel centroid $C\,[\,k\,]$ to the j[th] candidate, is given by [1]:

$$\sqrt{\frac{\left\| \mathbf{x}_j - \mathbf{x}_k \right\|_2^2}{s} + \frac{\left\| \mathbf{c}_j - \mathbf{c}_k \right\|_2^2}{m}} \tag{4.1}$$

where the values of s and m are normalizing factors for spatial and color distances, respectively. Logically, if we regard an image consisting of N pixels and K superpixels, each of the K superpixels is expected to contain NK^{-1} pixels. Assuming a square shape of the superpixels, the value of s can be defined as follows:

$$s = \sqrt{\frac{N}{K}} \tag{4.2}$$

The value of the normalizing factor for color distances, m, is user-provided, and within GEE defined as the *compactness factor*. If the user chooses to apply a higher value of m this will result in more compact superpixels, at the cost of poorer boundary adherence, and vice versa [112, 108]. The effect of a changing value of m for imagery over Bosomtwe 2022-03-19 is illustrated in images 4.8a, 4.8b and 4.8c.

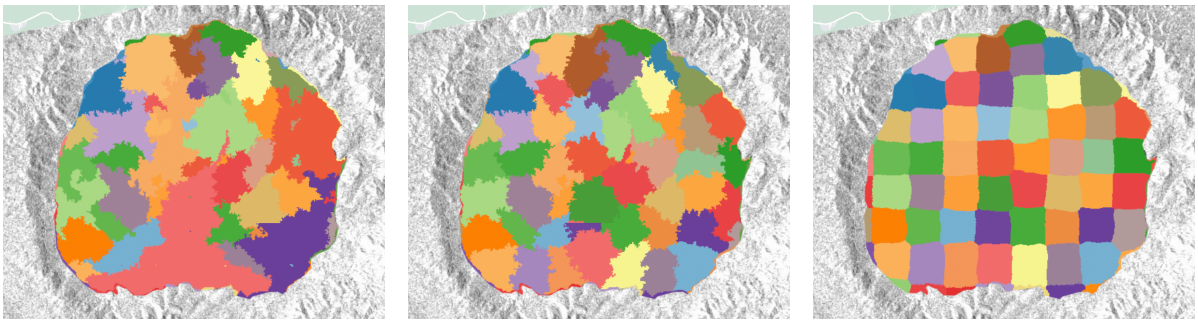

(a) $m = 0$ **(b)** $m = 100$ **(c)** $m = 10000$

Figure 4.8: Effect of Compactness Factor on SuperPixels

Starting from the initial centroids, the SNIC algorithm enforced a priority queue to choose which pixel is to be added to the cluster next. This queue is occupied with candidate pixels that are either 4 or 8-connected to the currently growing superpixel cluster. Whether a 4 or 8-connected priority queue

is utilized is an user-defined choice that can be set within the GEE environment by adjusting the *connectivity* parameter. Generally, the higher the value for this parameter, the smoother the objects will appear [1, 112, 108]. This can be seen in figures 4.9

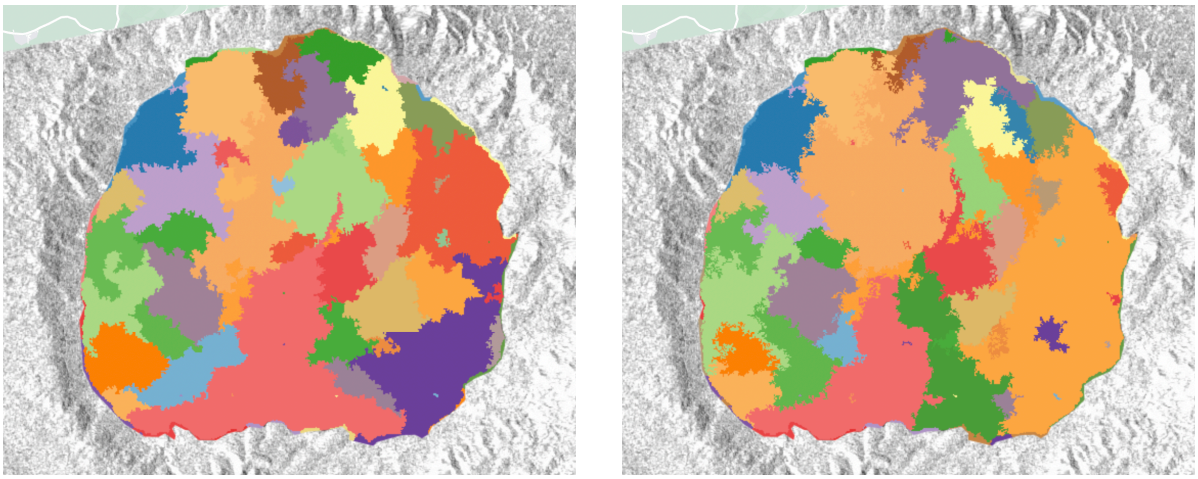

(a) $connectivity = 4$ **(b)** $connectivity = 8$

Figure 4.9: Effect of Connectivity Value on SuperPixel

Additionally, the superpixel *size* and *neighborhoodSize* are parameters within the SNIC algorithm that can be user-defined. The effect of setting the superpixel *size* speaks for itself, and is illustrated below in image 4.10. The *neighborhoodSize* defaults to $2 \times size$. This parameter sets a limit for the clusters and, if set to $size = 1$, will show large squares around some of the larger clusters. Essentially, the *size* parameter influences the overall size and number of the superpixels generated. The *neighborhoodSize* controls the size of the sliding window used for clustering, so a larger *neighborhoodSize* allows for more extensive spatial context in the clustering process.

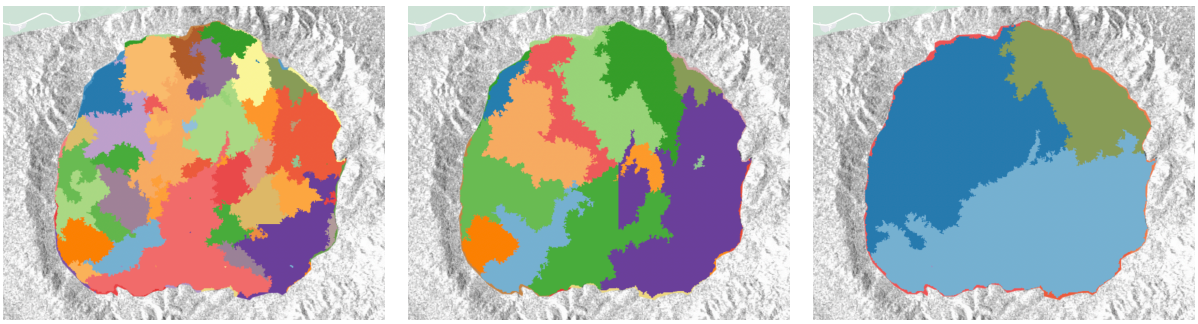

(a) $size = 50$ **(b)** $size = 100$ **(c)** $size = 250$

Figure 4.10: Effect of Size Value on SuperPixels

SNIC polygons were computed for each of the Sentinel-1 images used during the training process. The SNIC images have been vectorized and consequently reduced back to imagery with an added band containing a cluster-id. The original Sentinel-1 SAR images are overlayed with the SNIC cluster images, concatenating bands to create a final overlay. Usually, the SNIC superpixels are computed using the mean pixel values within the cluster. In this research, mean values were computed, as well as median values and the standard deviation.

SNIC was used for a number of reasons. First of all, all SAR images are affected by noise and speckle. By using the SNIC superpixels, this noise is effectively smoothened, while still keeping the important image structures. Because the the superpixels correspond to meaningful regions in the image, this makes visual interpretation and labeling easier.

Gray Level Co-Occurace Matrix

In addition to VV and VH values, texture and entropy factors increase the ability to differentiate between classes. The factor 'texture' was used in the form of the Gray-Level Co-Occurance Matrix (GLCM). In short, the GLCM is a tabulation of how often different combinations of pixel brightness values (or *gray levels*) occur in an image. The GLCM is based on gray-scale images, and evaluates the co-occurance of similar values occuring in the different possible directions: horizontally, vertically or diagonally [86]. In essence, the GLCM is a statistical method which allows us to capture the spatial relationships between pixels. By using these texture characteristics, we are provided insight in features such as the homogeneity, contrast and directionality. The GLCM features can be categorized into three main groups: a contrast group (contrast, dissimilarity, homogeneity), an orderliness group (angular second moment, maximum probability, entropy) and a statistics group (GLCM mean, variance and correlation). The mathematical expressions defining the GLCM features were provided by Haralick and Connors [52, 22] and are provided in equations 4.3 till 4.23.

$$ASM = \sum_i \sum_j \{p(i,j)\}^2 \tag{4.3}$$

$$Contrast = \sum_{n=0}^{N_{g-1}} n^2 \left\{ \sum_{i=1}^{N_g} \sum_{j=1}^{N_g} p(i,j) \right\} \tag{4.4}$$

$$Correlation = \frac{\sum_i \sum_j (ij) p(i,j) - \mu_x \mu_y}{\sigma_x \sigma_y} \tag{4.5}$$

$$Variance = \sum_i \sum_j (i-\mu)^2 p(i,j) \tag{4.6}$$

$$IDM = \sum_i \sum_j \frac{1}{1+(i-j)^2} p(i,j) \tag{4.7}$$

$$SAVG = \sum_{i=2}^{2N_g} i p_{x+y}(i) \tag{4.8}$$

$$SVAR = \sum_{i=2}^{2N_g} (1 - SENT)^2 p_{x+y}(i) \tag{4.9}$$

$$SENT = -\sum_{i=2}^{2N_g} p_{x+y}(i) log \{p_{x+y}(i)\} \tag{4.10}$$

$$DVAR = \text{variance of } p_{x-y} \tag{4.11}$$

$$DENT = -\sum_{i=0}^{N_{g-1}} p_{x-y}(i) log \{p_{x-y}(i)\} \tag{4.12}$$

$$IMCORR1 = \frac{HXY - HXY1}{\text{max of } \{HX, HY\}} \tag{4.13}$$

$$IMCORR2 = (1 - exp[-2.0\,(HXY2 - HXY)])^{1/2} \tag{4.14}$$

$$\text{where } HXY = -\sum_i \sum_j p(i,j) log(p(i,j)) \tag{4.15}$$

$$\text{where HX and HY are entropies of } p_x \text{ and } p_y \tag{4.16}$$

$$\text{where } HXY1 = -\sum_i \sum_j p(i,j) - log \{p_x(i) p_y(j)\} \tag{4.17}$$

$$\text{where } HXY2 = -\sum_i \sum_j p_x(i) p_y(j) log \{p_x(i) p_y(j)\} \tag{4.18}$$

$$MAXCORR = (\text{second largest eigenvalue of Q})^{1/2} \tag{4.19}$$

$$\text{where } Q(i,j) = \sum_k \frac{p(i,k)p(j,k)}{p_x(i)p_y(k)} \tag{4.20}$$

$$DISS = \sum_{i=0}^{N-1}\sum_{j=0}^{N-1} P_{i,j}(i-j) \tag{4.21}$$

$$Inertia = I(\delta,T) = \sum_{i=0}^{L-1}\sum_{j=0}^{L-1}(i-j)^2 s(i,j,\delta,T) \tag{4.22}$$

$$Shade = A(\delta,T) = \sum_{i=0}^{L-1}\sum_{j=0}^{L-1}(i+j-\mu_i-\mu_j)^3 s(i,j,\delta,T) \tag{4.23}$$

More formally, the GLCM is constructed by forming and M by M matrix with M possible Digital Numbers (DN), and then computing entry *i, j* as the frequency at which DN equals *i* is adjacent to DN equals *j*. Here, a DN is a characteristic of a remote sensing image that describes its sharpness and the clarity of objects in the image [104, 52, 22]. In different words, the matrix represents the relationship between two adjacent pixels. Once the GLCM has been constructed, a variety of texture metrics can be computed based on that matrix. Applying GLCM in GEE, using the `ee.Image.glcmTexture()` function, creates an image where each bands is a different metric. It yields a total of eighteen bands. Fourteen of these bands consist of Second Order Statistical Texture features proposed originally by Haralick. Additionally, four metrics from Connors (1982) are calcualted [52, 22].

The entropy factor computed through the GEE GLCM package should not be confused with the standard entropy computed through GEE. Naturally, both GLCM and 'normal' entropy are computed using the same basic function, namely [22]:

$$entropy = -\sum p \times \log_2(p) \tag{4.24}$$

Using the GLCM, the function evolves to the following:

$$entropy = -\sum_i \sum_j p(i,j) \times \log\left[p(i,j)\right] \tag{4.25}$$

In which $p(i,j)$ is the *(i, j)th* entry in a normalized gray-tone spatial-dependence matrix, $\frac{P(i,j)}{R}$, in which *R* is a normalizing constant. In a broader sense, entropy is a measure or concept of randomness or disorder. Within a Remote Sensing context, entropy is an index of the numerical diversity in the neighborhood. Within GEE, the entropy is computed using the entropy function given in function 4.24 and the structuring element of a kernel. Given that this operation only supports 32-bit or smaller integer types, images have to be recast prior to such operations.

For the normal backscatter intensities, the computed entropy and the GLCM values, both in the VV and VH polarizations, the pixel values are calculated. This yields an image with a total of 40 bands. Using the SNIC clusters, found previously, as a backdrop, the mean, median and standard deviation of each of the features is computed within each of the SNIC superpixels.

4.4.3. Classification

Following the pre-processing steps and the creation of the training data, a classifier can be trained to detect Bragg scattering. Since this research works with open-source GEE data and a web-based interface, no specific downloadable or costly software is required for the creation of the final product.

In section 3.5, a variety of classification algorithms were discussed, including thresholding, SVMs, CART classifiers and Random Forests. Each Machine Learning method functions in its own specific manner, separating the training data and preforming the final classification differently. As the results of this type of classification can be visually interpreted, a qualitative analysis can be preformed with

Table 4.3: Gray-Level Co-Occurance Matrix Features [22, 52]

Feature	Description	Additional Information
ASM	Angular Second Moment	measures the number of repeated pairs
CONTRAST	Contrast	measures the local contrast of an image
CORR	Correlation	measures the correlation between pairs of pixels
VAR	Variance	measures how spread out the distribution of gray-levels is
IDM	Inverse Difference Moment	measures the homogeneity
SAVG	Sum Average	
SVAR	Sum Variance	
SENT	Sum Entropy	
ENT	Entropy	measures the randomness of a gray-level distribution
DVAR	Difference Variance	
DENT	Difference Entropy	
IMCORR1	Information Measure of Corr. 1	
IMCORR2	Information Measure of Corr. 2	
MAXCORR	Maximum Corr. Coefficient	
DISS	Dissimilarity	
INERTIA	Inertia	
SHADE	Cluster Shade	
PROM	Cluster Prominence	

the final classification image produced. To evaluate the performance of the model in a quantitative manner, accuracy assessment is applied. These statistics give insight in both the overall performance of the model and the underlying mechanisms. In this research, a comparison is made between CART classifiers, RFs and SVMs.

4.4.4. Outline Finding

With the classification result (Water/Bragg scattering/Shore) computed, an approximation of the reservoir outline and surface area is computed by grouping the different classes and reducing the raster imagery to vectors. Consequent growing and shrinking operations to eliminate small patches of wrongly-classified superpixels.

Outline Approximation Through Geometric Mean

Initially, the reservoir outline was found by employing a different algorithm, that used the HydroLAKES database and a geometric mean based on the Sentinel-1 imagery from both before and after the date of interest. This method was not employed in the final classification, because it relied to heavily on the external HydroLAKES information and, since it required imagery from past the date of interest, it could not be employed to classify in real-time. Because the algorithm did yield accurate results of the approximate reservoir outline, and the results acquired through this method are later compared to the outline found through the classification results, the methodology of the outline-finding algorithm is still discussed here.

The process has the aim of providing an accurate geometry of the reservoir shoreline. This process is especially relevant for when relatively small reservoirs are subjected to classification, as the effect of temperature and seasonality on the reservoir surface is relativity much larger for these reservoirs, compared to larger reservoirs [28]. The process is illustrated using imagery taken from Lake Bosomtwe at 11-06-2022 in figure 4.11. This process starts with taking the HydroLAKES shoreline polygon and finding the point at the center of the geometry, taking into account a maximum error tolerated when preforming any necessary re-projection. The script overlays this centroid – an `ee.Geometry()` – with the relevant SAR imagery over this location.

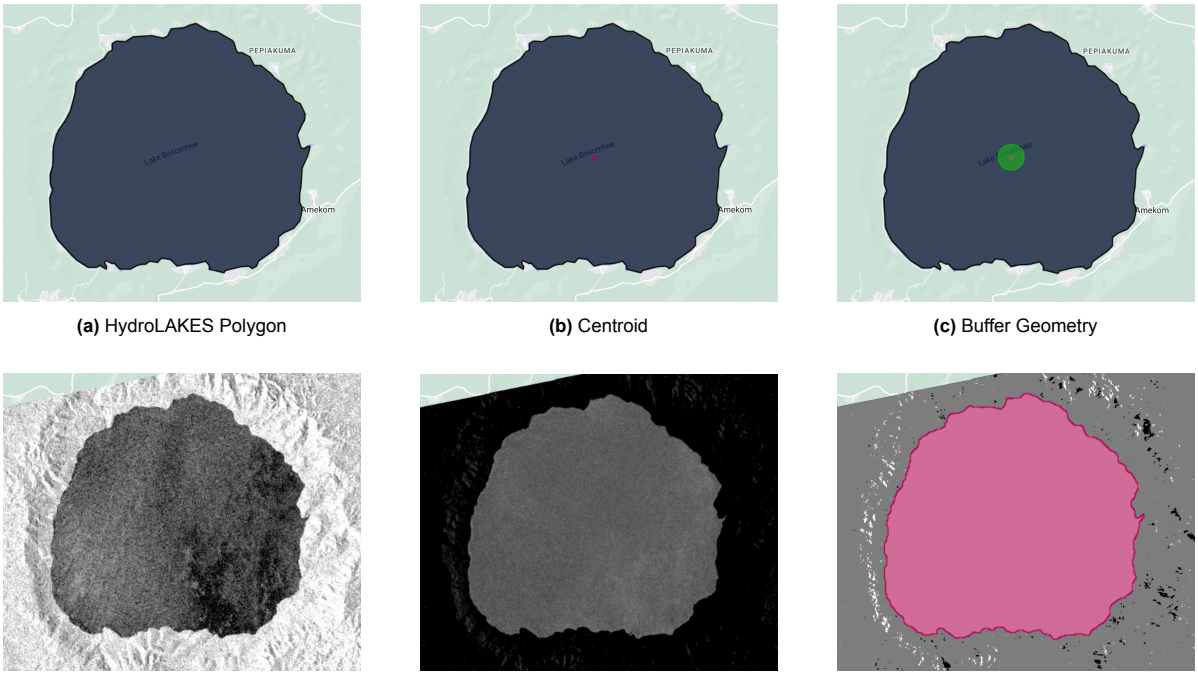

(a) HydroLAKES Polygon **(b)** Centroid **(c)** Buffer Geometry

(d) VV Imagery **(e)** σ_{vhvv} **(f)** Shoreline Polygon

Figure 4.11: Process steps of finding shoreline geometry through geometric mean for lake Bosomtwe, Ghana

In this instance, the relevant SAR imagery means the median of all available SAR imagery within a date range of one month: both before the date at which the classification is to be made as a month previous. The image is clipped using a bounding box with a distance of three km of the centroid. Given the rarity of Bragg scattering occurring, computing the median of the SAR imagery over a range of two months will yield an image that would almost always be free of Bragg scattering.

Depending on the size of the reservoir, a sample buffer around the centroid is created. The geometric mean is computed, based on the median composite calculated previously. This geometric mean σ_{vhvv} is given by the function 4.26 [62].

$$\sigma_{vhvv} = \sqrt{\sigma_{vh,median} \times \sigma_{vv,median}} \tag{4.26}$$

The geometric mean σ_{vhvv} is applied based on the assumption that, by taking the geometric mean, low σ values will be raised. These low σ values could be falsely interpreted as water. Based on the statistical mean and the standard variation applicable, a range is determined within which water pixels can be found, based on the work of Kavats *et al.* [62]. Again, a maximum error is defined such that the amount false positives and false negatives is minimized, without hindering computational time. By computing the reservoir outline for a range of reservoirs on dates where clear Sentinel-2 imagery was available, comparing the computed reservoir outline with the optical imagery and computing the error margin between the computed outline and the actual reservoir outline, various ranges for the water mask were tested. The smallest error margin between the computed reservoir outlines and actual reservoir outline were found by employing a water mask of:

$$\mu_{\frac{1}{2}} - 3\sigma < water < \mu_{\frac{1}{2}} + 3\sigma \tag{4.27}$$

For the case depicted in figures 4.11a to 4.11f, this range is visualized in figure 4.12. Naturally, this algorithm will classify some water pixels as shore and visa versa. However, since these wrongly identified instances are of small scale and are relatively well scattered over the zone of interest, a simple consecutive growing and shrinking operation on the resulting polygon is sufficient to remove these wrongly identified patches.

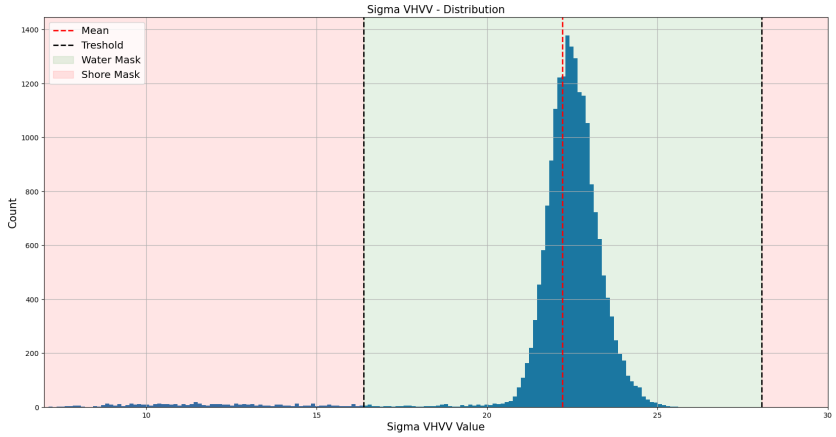

Figure 4.12: Statistical Range Water Mask

Confusion Matrix

Classification metrics can be divided into three main groups: binary, multi-class and multi-label classification. In a binary classification, there are two classes and the map produced by such a classification has the option for each of the image's pixel to either have a particular trait associated with it (+) or not (-). Examples include change vs. no-change, forest vs. no-forest. In multiclass classification, machine learning is focused on categorizing data into more than two classes. Examples include email categorization (spam, non-spam, important) or handwritten digit classification. Multi-label classification is a machine learning paradigm where instances can be associated with multiple labels simultaneously. An example of this is document tagging. From this characterization, it can easily be seen that in this study we are dealing with multiclass classification.

One of the most commonly applied methods of accuracy assessment is the confusion matrix, which, in essence, shows how (often) the model is confused during classification. An example of an confusion matrix is provided in figure 4.13. For a binary classification the confusion matrix takes the form of a 2×2 table. The binary confusion matrix has four elements that summarize every possible scenario of class labeling [42]. From these labels, a range of other metrics, such as the Overall Accuracy (OA), the Producers Accuracy (PA) and Users Accuracy (UA) can be calculated. For multi-class classification, the confusion matrix increases in size.

		Acutal Class			
		Class 1	**Class 2**	**Class 3**	
Predicted Class	**Class 1**	Cell 1 (TP)	Cell 2 (FP)	Cell 3 (FP)	Total 4
	Class 2	Cell 4 (FN)	Cell 5 (TN)	Cell 6 (TN)	Total 5
	Class 3	Cell 7 (FN)	Cell 8 (TN)	Cell 9 (TN)	Total 6
		Total 1	Total 2	Total 3	Total

		Acutal Class			
		Class 1	**Class 2**	**Class 3**	
Predicted Class	**Class 1**	7550	43	89	7682
	Class 2	58	349	4	411
	Class 3	59	0	7162	7221
		7667	392	7255	15314

Figure 4.13: Confusion Matrix

Essentially, the OA tells us, out of all the reference data, what proportion is classified correctly, usually expressed as a percentage. It is an easy metric to calculate and interpret, but ultimately only provides both user and producer with very basic accuracy information.

$$OverallAccuracy = \frac{TP + TN}{TP + TN + FP + FN} \tag{4.28}$$

The PA tells the map accuracy from the perspective of the map producer, and thus shows the probability that a certain cover class - water or Bragg scattering - of a water body area is classified as such. The

metric is the complement of the Omission Error (OE), which is $OE = 1 - PA$. In the same manner, the UE, or reliability, is the accuracy from the point of view of the map user, and essentially tells us how often the class on the map will actually be present on the ground. It is complement of the Commission Error (CE): $UA = 1 - CE$.

Early papers already highlighted the limitation of these conventional approaches to accuracy assessment, especially regarding the omnibus index of overall accuracy [42]. With this statistic, the magnitude can be highly sensitive to variations in class abundance. As with many classification problems, i.e. land cover change or with the present problem of Bragg scattering detection, one class is often very rare. With these cases, high accuracy can very easily be achieved by merely allocating all cases to the most bountiful classes. With those circumstances, a classification could yield a high accuracy while in actuality providing a very poor representation of reality, especially in regard to the rare class [40, 58].

Kappa Coefficient

The Kappa coefficient (κ) is a value that represents the performance of the classification relative to a random classification, i.e. indicating if the classification does better than a random classification. It can be calculated from the confusion matrix and is widely used in classification accuracy assessment. Using notation from Foody and Giles[42], κ can be calculated from:

$$\kappa = \frac{p_0 - p_e}{1 - p_e} \tag{4.29}$$

$$p_0 = \frac{C1 + C5 + C9}{Total} \tag{4.30}$$

$$p_e = \frac{T1 * T5}{Total^2} + \frac{T2 * T5}{Total^2} + \frac{T3 * T7}{Total^2} \tag{4.31}$$

In which p_0 is the proportion of cases classified correctly (OA) and p_e is the expected proportion of cases correctly classified by chance. The value of κ lies between -1 and 1, but interest is typically only focused on the positive part of the range, as a negative value would indicate a classification with less agreement to reality than chance alone, and would thus be difficult to interpret. The maximum value of 1 occurs when there is perfect agreement and a value of 0 indicates that the observed agreement between classification and reality equals that of due to chance.

Training and Validation Sets

Following the construction of the training data, the data is partitioned into two datasets: a training set and a validation set. Both sets fulfill a distinct purpose, contributing to the building of a robust and reliable model. The training set is at the cornerstone of the model development. It is used to train the Machine Learning algorithm and is enables the model to learn the underlying patterns and relationships present in the data. It is used to compute a training confusion matrix and thus indicate the training accuracy.

The validation set serves as a vital supplement to the training dataset. During model training it is easy for the model to fall for over-fitting, as the model tries to fold itself to the training data characteristics at the expense of generalizing the actual underlying patterns within the data. In this regard, the validation set serves as an impartial judge, as it evaluates the models performance on data its never seen before. A large difference between accuracy in the training and validation set could therefore indicate over-fitting. To this purpose, a data split of 70/30 was used.

5

Results

5.1. Introduction

This chapter displays the main results relevant to the scope of this research. The performance of different available classifiers is compared and a final classifier is chosen and optimized. The potential of Sentinel-1 data to classify Bragg scattering is discussed and the relevance of a range of computed Sentinel-1 features is discussed.

5.2. Performance Classifiers

There is a wide variety of classifiers available, both in general and through GEE. A variety of those classifiers were compared as to determine which would be best suited for the classification of Bragg scattering in Sentinel-1 imagery. As described previously in chapter 4, the following classifiers were compared:

- CART
- Random Forest
- Support Vector Machine

Each classifier was trained on the collected training samples, which's construction has been described previously in chapter 4. Their outputs were compared in terms of Overall Accuracy, Kappa Coefficient and visual output. These first two qualitative estimates were summerized below in table 5.1.

Table 5.1: Accuracy Scores Classifiers

	CART	**RF**	**SVM**
Overall Accuracy	0.9801	0.9835	0.8509
Kappa Coefficient	0.9638	0.9696	0.7250

As can be seen, Overall Accuracy scores are relatively comparable across classifiers. As mentioned before, we are dealing with an unbalanced dataset, which indicates that Overall Accuracy could not be a faultless measure of the classifiers' validity. As such, the Kappa Coefficient provides a better insight in the functionality of the different classifiers. In this regard, the SVM under-performs compared to the CART and RF classifiers, who both show to be similar in terms of Overall Accuracy and Kappa Coefficient. Visual results too were compared across reservoirs. To illustrate these findings, a selection of output results for the Bosomtwe reservoir are provided in figures 5.1 to 5.6.

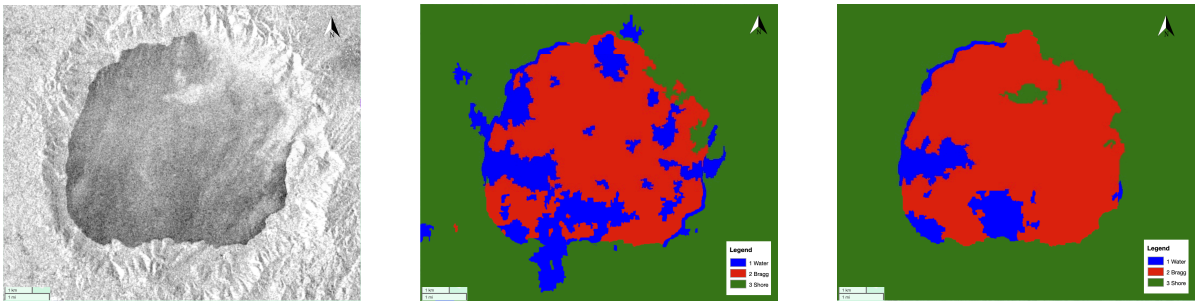

(a) Sentinel-1 Imagery (VV) **(b)** CART Classification **(c)** RF Classification

Figure 5.1: Bosomtwe 2021-01-29

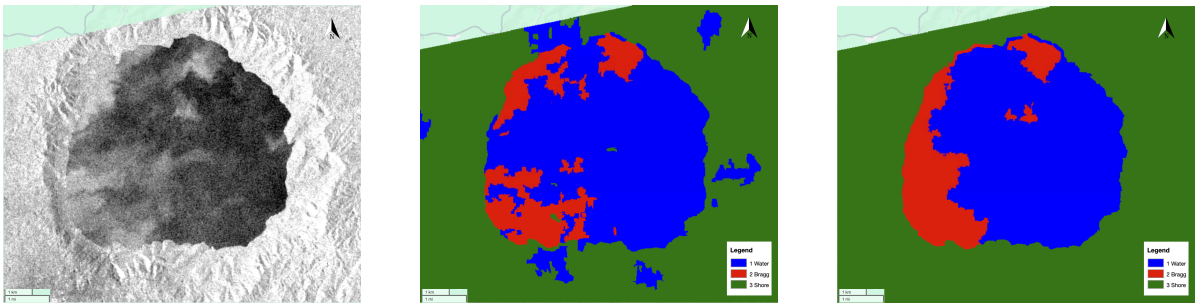

(a) Sentinel-1 Imagery (VV) **(b)** CART Classification **(c)** RF Classification

Figure 5.2: Bosomtwe 2021-02-16

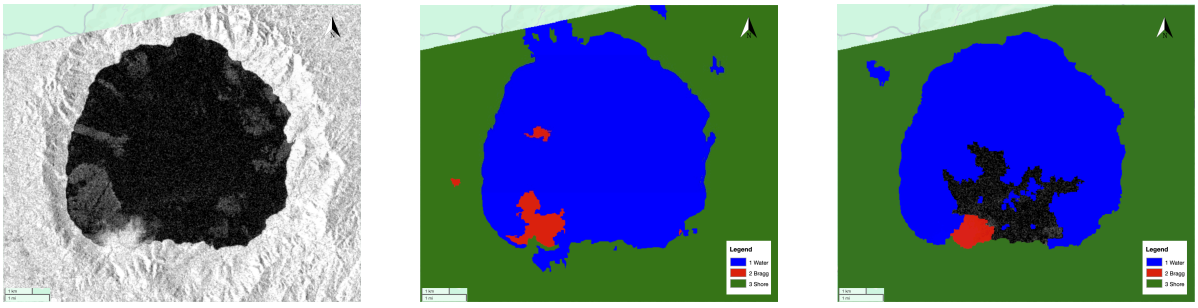

(a) Sentinel-1 Imagery (VV) **(b)** CART Classification **(c)** RF Classification

Figure 5.3: Bosomtwe 2021-07-22

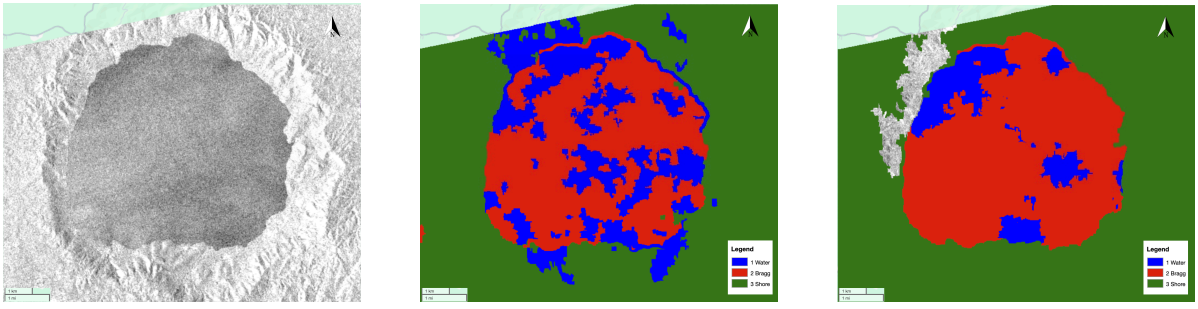

(a) Sentinel-1 Imagery (VV) **(b)** CART Classification **(c)** RF Classification

Figure 5.4: Bosomtwe 2022-03-07

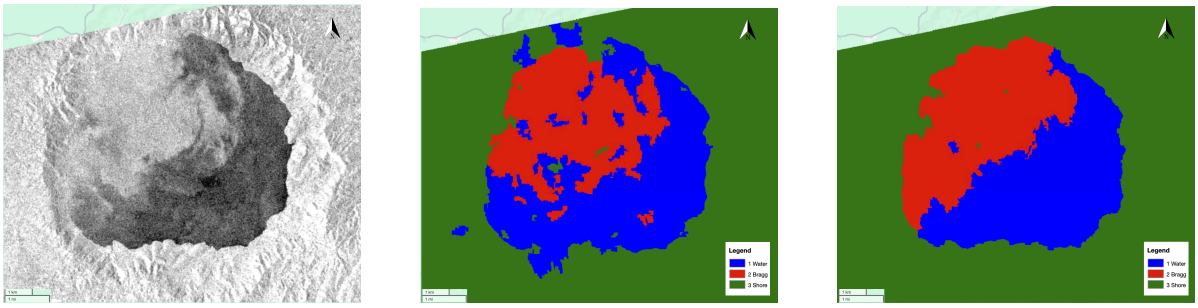

(a) Sentinel-1 Imagery (VV) **(b)** CART Classification **(c)** RF Classification

Figure 5.5: Bosomtwe 2022-03-19

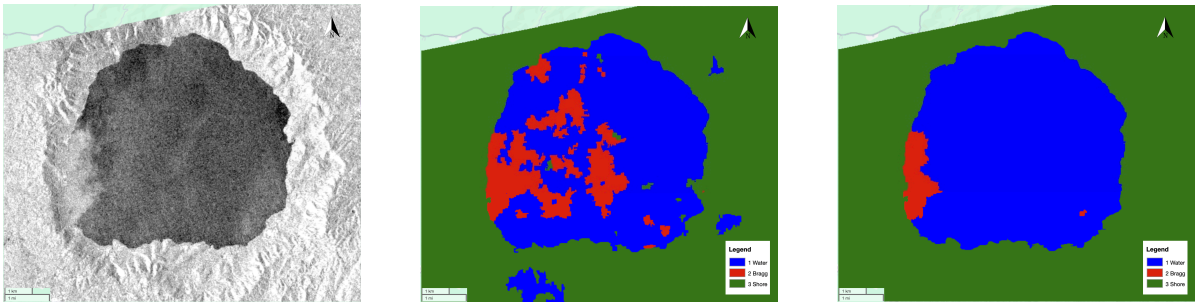

(a) Sentinel-1 Imagery (VV) **(b)** CART Classification **(c)** RF Classification

Figure 5.6: Bosomtwe 2022-03-31

For the 2021 imagery, CART and RF show comparative outputs. In the 2022 imagery specifically, the CART results show to be a little more patchy than the RF output. The RF output shows higher coherency compared to the CART output, with less loose patches, and generally seems to follow the Bragg scattering outlines better. Given that a RF is overall more robust to both outliers and noise than a CART classifier, the higher performance scores and the fact that a RF has a lower tendency to overfit, the choice was made to work with a RF.

5.3. Hyperparameter Tuning

With the choice of classifier set on a RF and the training data compiled, it is time to improve on model performance via hyperparameter tuning. Gathering more data and feature engineering usually has the greatest payoff in terms of time invested versus improved classifier performance, but if those routes have been exhausted, it can be worthwhile to move onto hyperparameter tuning. Hyperparameters are not to be confused with model parameters, which are learned during model training, whereas hyperparameters are set before training. GEE implements a set of sensible default hyperparameters for its classifier models, but these are not to be guaranteed to be an optimal choice for each specific classification problem. In this study, the following hyperparameters are considered for optimization:

- Number of Trees
- Minimum Leaf Population
- Bag Fraction
- Max Nodes

The first parameter speaks for itself: the number of decision trees to be trained and compiled, and as such synonym to the size of the forest. There is extensive literature to be reviewed on the question whether the number of trees in the RF is significantly tied to model performance. Experimental research show that increasing the number of trees in the RF does not guarantee better model performance, and that sometimes using a larger number of trees only increases it's computational cost, without showing any significant performance gain [91].

Consequently, the RF is composed of an N amount of decision trees, which in turn are composed of multilevel and multi-leaf nodes. Therefore the decision tree can be 'pruned' by controlling the parameters or thresholds of the new branch. In this context, the *maxNodes* hyperparameter refers to the maximum number of 'leaves' per tree, and the *minLeafPopulation* parameter is the miminum number of nodes that are created for the training set. If not specified explicitly in GEE, the *maxNodes* value would be unlimited [130].

To determine what the optimal values for these hyperparameters should be, a RF was trained on a range of values for each of the hyperparameters, and the resulting Kappa Coefficient and Overall Accuracy was computed and plotted. The result of these computations are provided below.

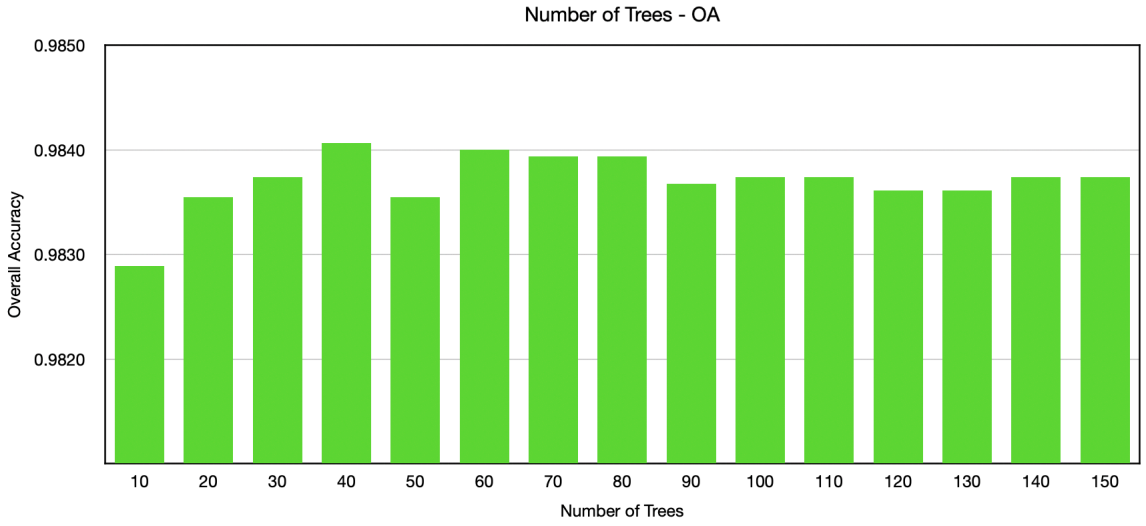

(a) Overall Accuracy

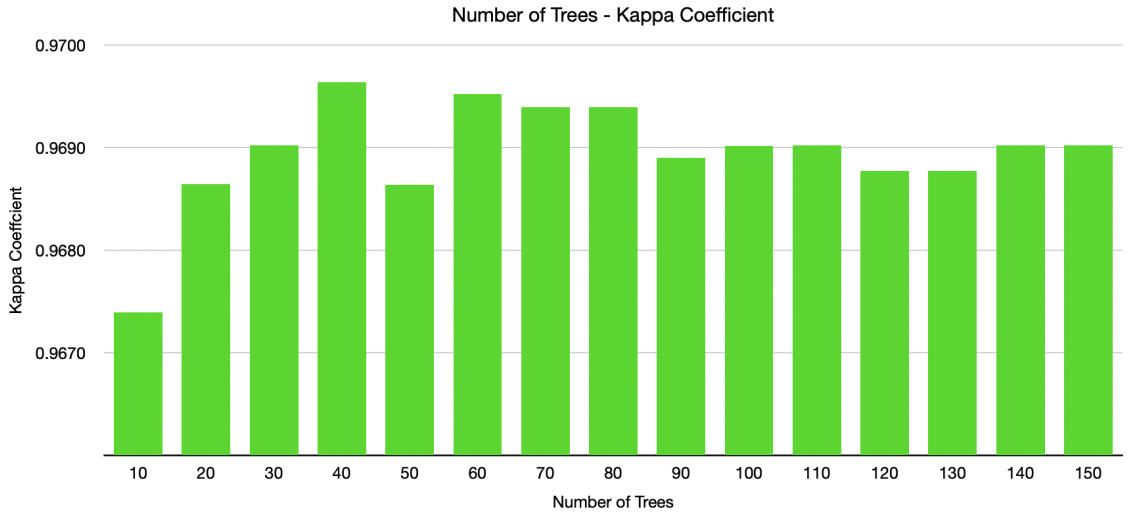

(b) Kappa Coefficient

Figure 5.7: Effect Number of Trees on Quality Classification

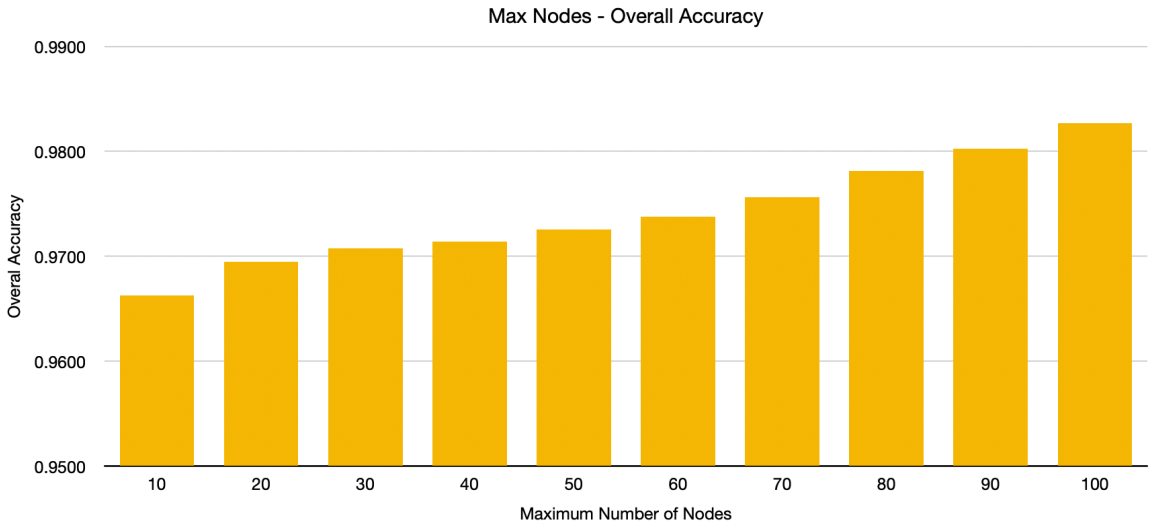

(a) Overall Accuracy

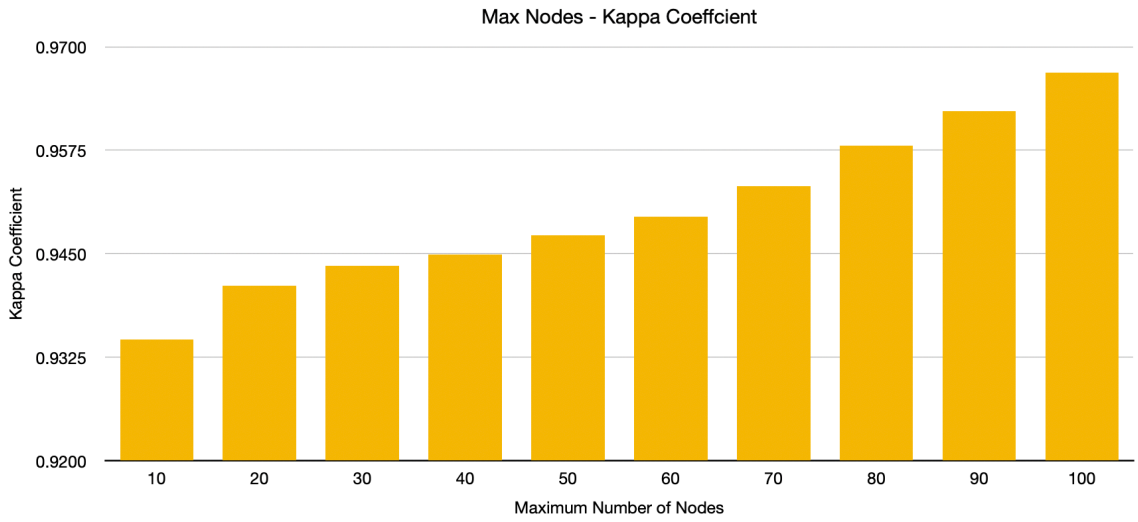

(b) Kappa Coefficient

Figure 5.8: Effect Maximum Nodes on Quality Classification

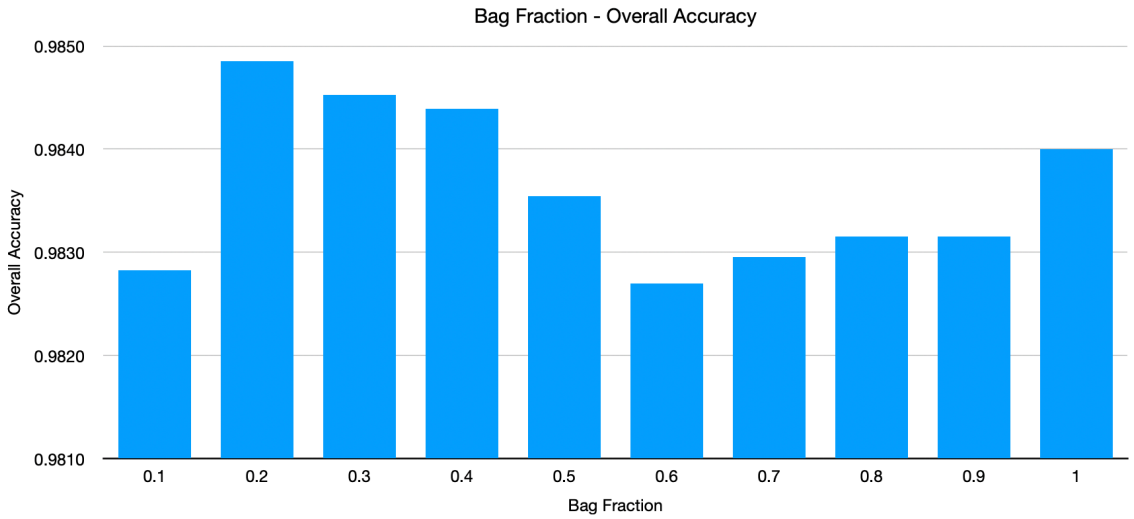

(a) Overall Accuracy

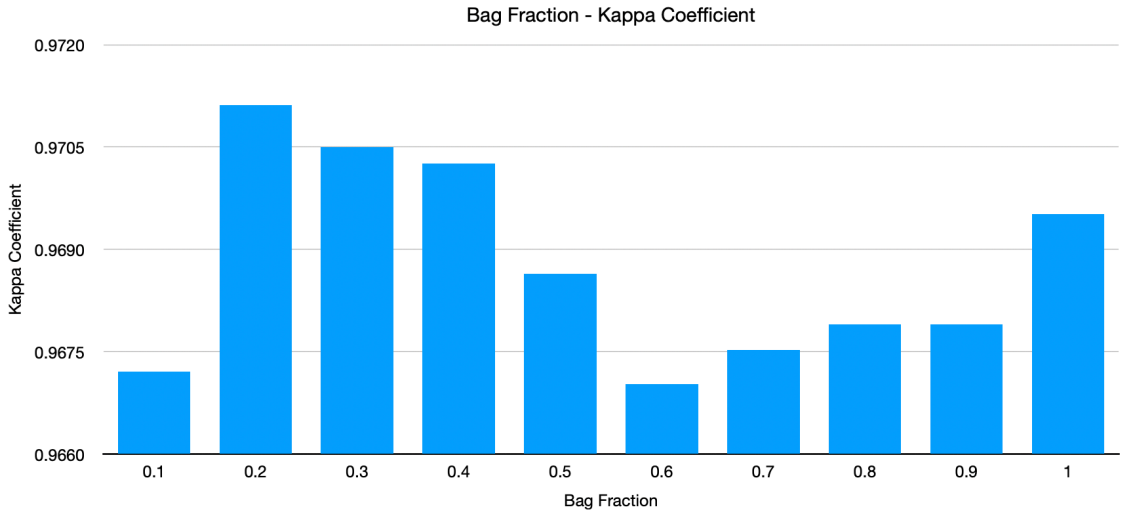

(b) Kappa Coefficient

Figure 5.9: Effect Bag Fraction on Quality Classification

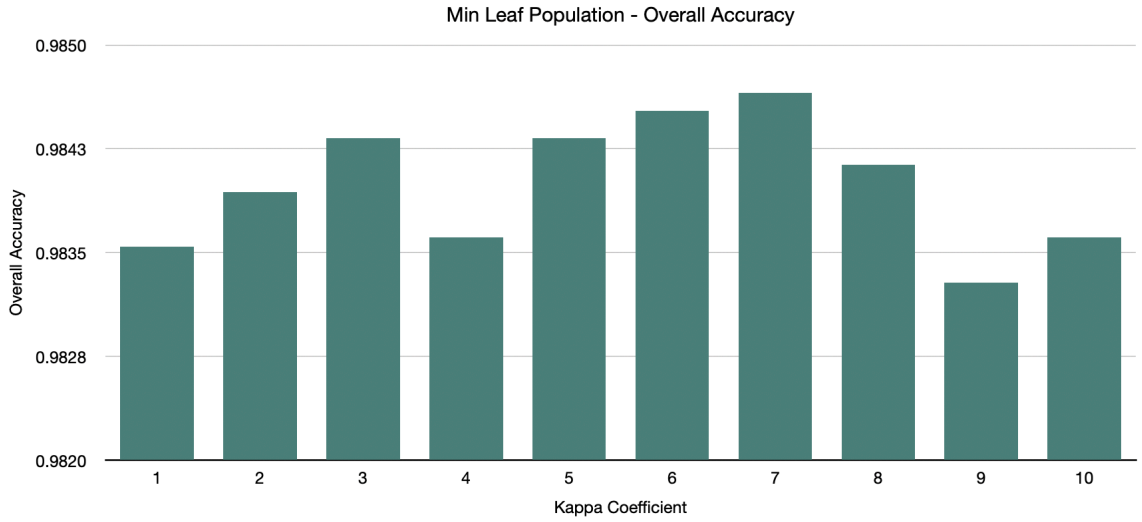

(a) Overall Accuracy

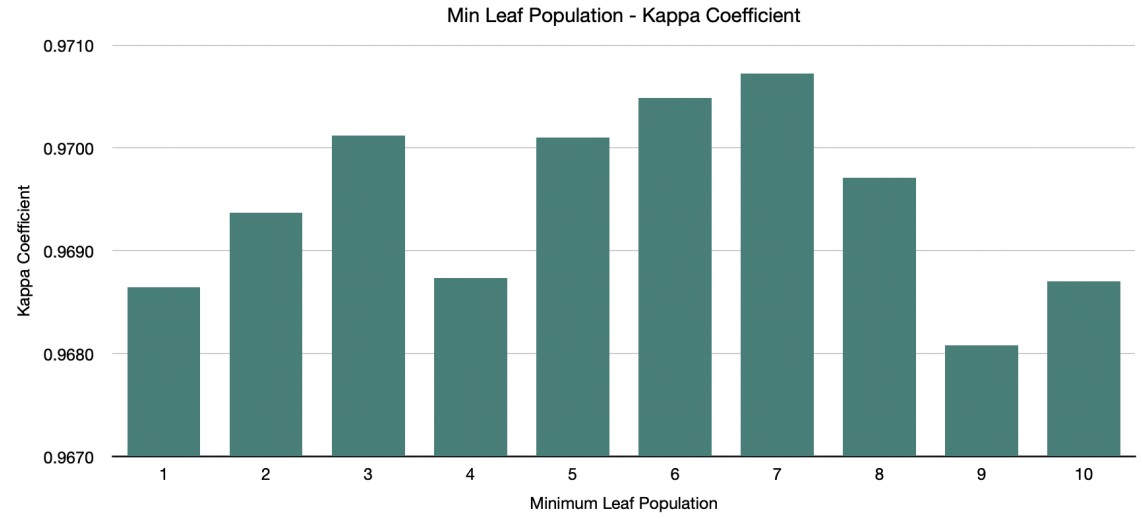

(b) Kappa Coefficient

Figure 5.10: Effect Minimum Leaf Population on Quality Classification

As we can see, for the OA specifically, the range of scores is very small. A larger difference can be seen with the KC. For the number of trees, the highest scores are obtained when using a medium number of trees, approximately 40, rather than using a larger forest. The maximum amount of nodes seems to show an opposite trend: the higher the number of nodes, the better the performance, both in terms of OA and KC. As the maximum number of nodes defaults to null - e.g. no limit - it was decided to leave this parameter on default setting. For the bag fraction, scores show a slight improvement when lowered to 0.2: a 2.39% increase in KC compared to the average KC score of the other tested bag fractions. With a default setting 0.5, the found value of 0.2 was found to be the better choice. With the minimum leaf population, mixed results are shown. For the KC, scores tend to be highest at approximately 7.0, and shows a decrease if either higher of lower value are picked. In conclusion, by observing the figures 5.7a, 5.7b, 5.8a, 5.8b, 5.9a, 5.9b, 5.10a and 5.10b, the tuned parameters are found to be the following, summerized in table 5.2.

To inspect the effect of these tuning activities on the visual output of the classifier, imagery of the classification is provided for some specified dates over lake Bosomtwe and the Kpong reservoir. Both the classification output using default hyperparameters and the classification output using the tuned

Table 5.2: Random Forest default and tuned parameters

	Number of Trees	Min. Leaf Population	Bag Fraction	Max. Nodes
Default Parameter	Always specified	1.0	0.5	null
Tuned Parameter	40.0	7.0	0.2	100

hyperparameters are provided, as described in table 5.2. The results are shown in figures 5.11, 5.12, 5.13, 5.14, 5.17 and 5.16.

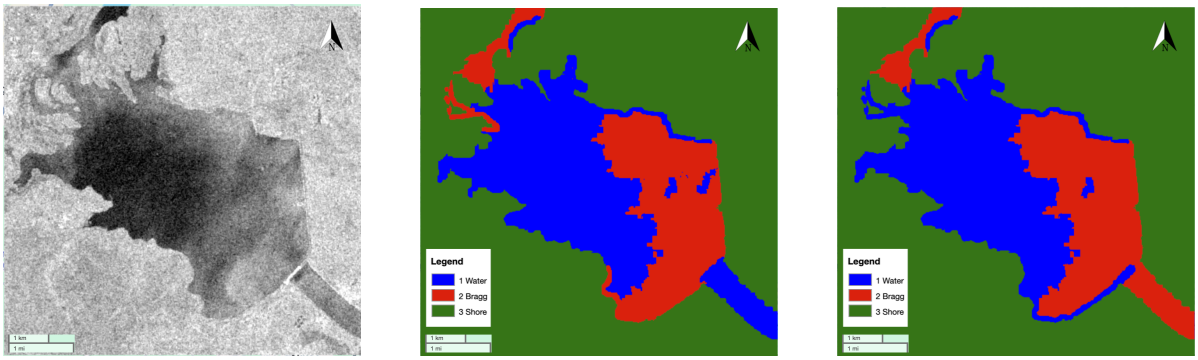

(a) Sentinel-1 Imagery (VV) **(b)** Default Hyperparameters **(c)** Tuned Hyperparameters

Figure 5.11: Kpong 2018-09-18

(a) Sentinel-1 Imagery (VV) **(b)** Default Hyperparameters **(c)** Tuned Hyperparameters

Figure 5.12: Kpong 2019-02-27

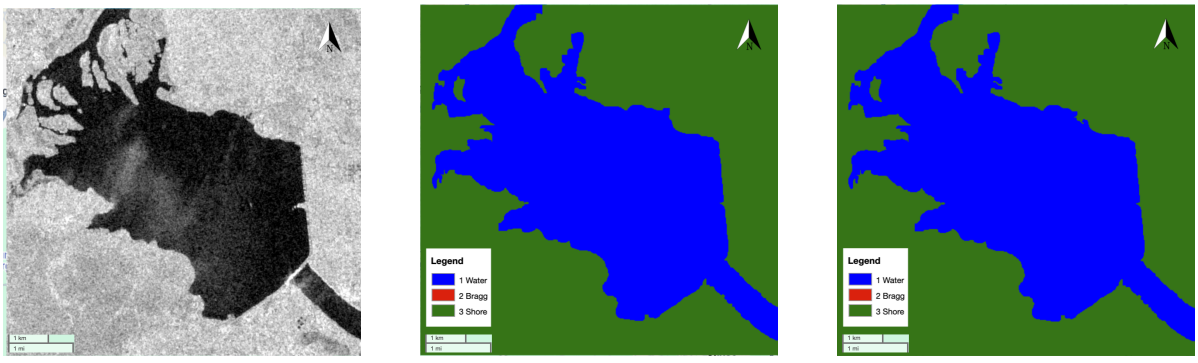

(a) Sentinel-1 Imagery (VV) **(b)** Default Hyperparameters **(c)** Tuned Hyperparameters

Figure 5.13: Kpong 2019-10-25

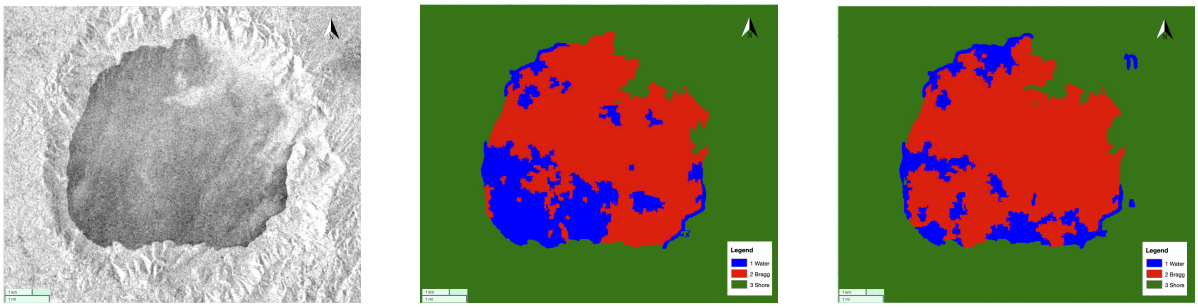

(a) Sentinel-1 Imagery (VV) **(b)** Default Hyperparameters **(c)** Tuned Hyperparameters

Figure 5.14: Bosomtwe 2021-01-29

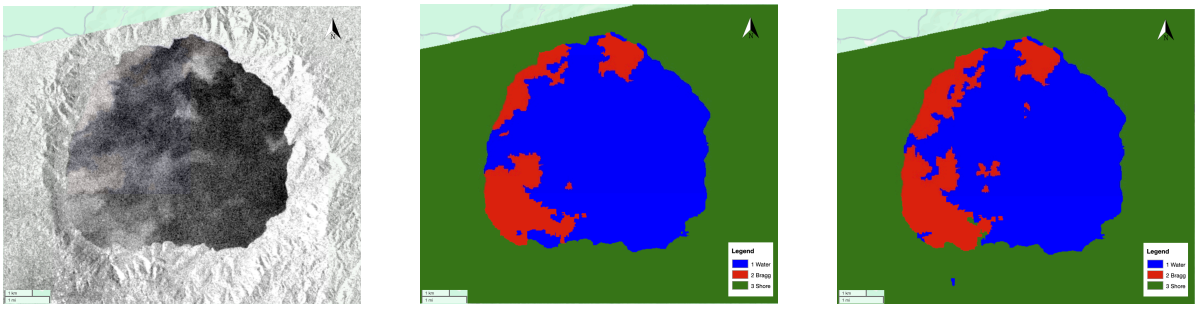

(a) Sentinel-1 Imagery (VV) **(b)** Default Hyperparameters **(c)** Tuned Hyperparameters

Figure 5.15: Bosomtwe 2021-02-16

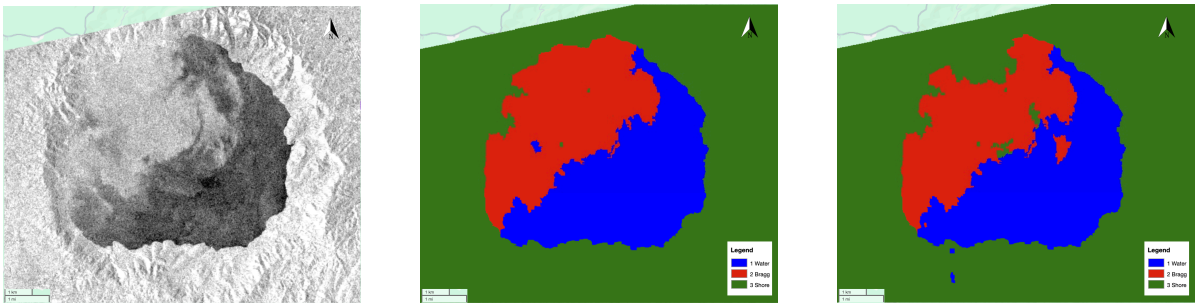

(a) Sentinel-1 Imagery (VV) **(b)** Default Hyperparameters **(c)** Tuned Hyperparameters

Figure 5.16: Bosomtwe 2021-03-19

As we can see in these images, the default/untuned classifier is somewhat less sensitive than the classifier with tuned hyperparameters. This lower sensitivity works for the better in some cases, where it correctly classifies smaller patches of water (non-Bragg) within or connected to larger Bragg scattering patches.

Strangely, images 5.11 to 5.16 show that the default/untuned classifier outperforms the tuned classifier. Although tuning the classifier least to a higher OA and KC score, it noticeably yields visual outputs that are less consistent with reality. The tuned classifier is too sensitive to Bragg scattering, and therefore classifies patches of water as Bragg scattering. Especially when dealing with larger patches of Bragg scattering, the tuned classifier is not able to distinguish between intense Bragg scattering from lighter Bragg scattering patches.

5.4. Relative Band Importance

With the use of both VV and VH polarizations, as with the computed bands for entropy, GLCM and the computation of the mean, median and standard deviation for each of the superpixels calculated using SNIC, a total of 102 bands are in play during classification. Naturally, not all variables carry the same weight in the classification result. To lower the number of variables used - and consequently the computational costs of the classification - the relative importance of the variables are computed and plotted. The RF variable importance is computed after the training and tuning process, to examine the the contribution of each predictor during training. Within GEE, it is a relatively straightforward process to extract variable importance once a RF has been trained. During this process, GEE bases the variable importance on the sum of decrease in Gini Impurity over all trees in the RF. To elaborate, as we move down in the decision tree, every time a split of a node is made, the impurity criterion, the Gini impurity in this case, for the two descendant nodes is less than that of the parent node. By adding up these decreases for each individual variables, over all the trees in the RF, the variable importance is calculated [72, 126].

In calculating the variable importance, a division was made between the mean, median and standard deviation. This was done to make inspection and comparison of the relative importance easier. The relative variable importance for the previously trained and tuned RF is provided below in images 5.17a, 5.17b and 5.17c. A cut-off value of 1.0 was chosen as to select variables for the final model.

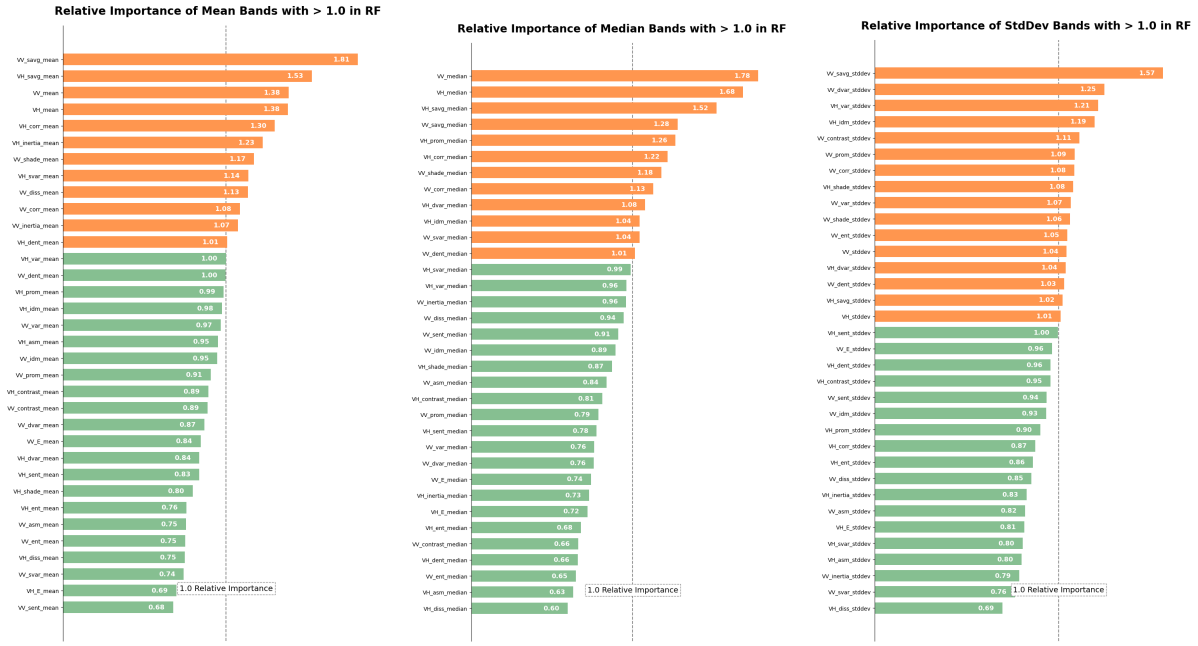

(a) Mean Bands **(b)** Median Bands **(c)** Standard Deviation Bands

Figure 5.17: Relative Importance of Mean, Median and Standard Deviation Bands used in Classification

The dotted line in figures 5.17a, 5.17b and 5.17c shows the 1.0 Relative Importance cut-off. All bands above this cut-off value are shown in orange and have thus been selected. Bands shown in green score a Relative Importance below the cut-off value, and are not taken into account during classification. In total, a selection of 44 bands was made: eighteen from the mean bands, fourteen from the median bands and twelve from the standard deviation bands. Those selected bands were used in the further development of the RF classification.

Relevant GLCM Features

By analyzing the relative band importance in the three statistics (mean, median and standard deviation), there are three GLCM features that are found to contribute positively in each statistics: the sum average (savg), the correlation (corr) and cluster shade (shade). Plotting these GLCM features shows, interestingly enough, that these features are relatively insensitive to Bragg scattering on SAR imagery,

especially in the VH polarization. These features are plotted for an arbitrary date in figure 5.18.

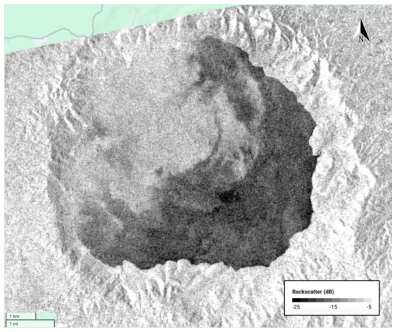

(a) Sentinel-1 Image (VV)

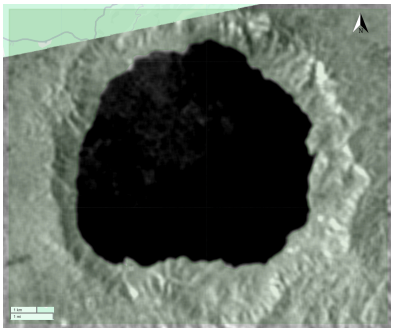

(b) GLCM Sum Average (Savg)

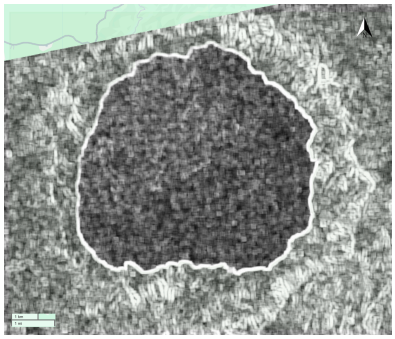

(c) GLCM Correlation (Corr)

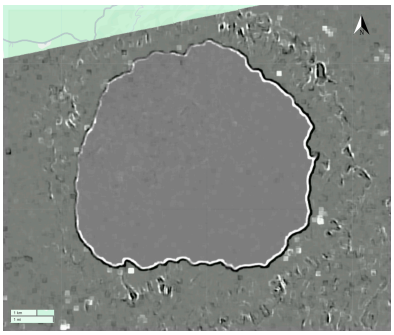

(d) GLCM Cluster Shade (Shade)

Figure 5.18: Bosomtwe 2022-03-19 - Effect GLCM

5.5. Performance Random Forest Classification

Taking into account all previously stated conclusions and decisions regarding the RF (the band importance and hyperparameter tuning), the trained RF is applied and tested on a variety of water reservoirs under a variety of circumstances. The classification of the reservoirs Bosomtwe, Kpong, Tono, Vea and Voggo were evaluated on different dates and examples of classifications are provided. This section will hence start with an overview of classifications, that will be discussed afterwards. In figures 5.19 to 5.33 the Sentinel-1 imagery and the classification results are provided. Based on the computed classification result, a tentative outline of the reservoir is computed, by which reservoir surface area can be estimated. The outline computed, based on the classification result, is also provided in the imagery below.

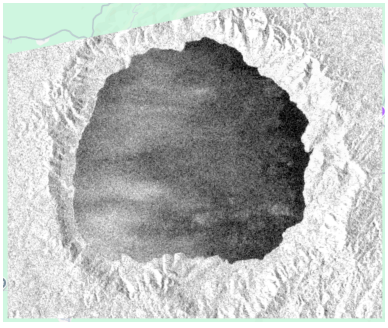

(a) Sentinel-1 Image (VV)

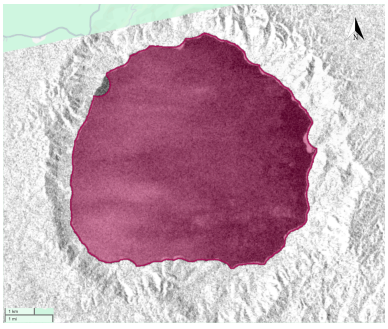

(b) Computed Outline

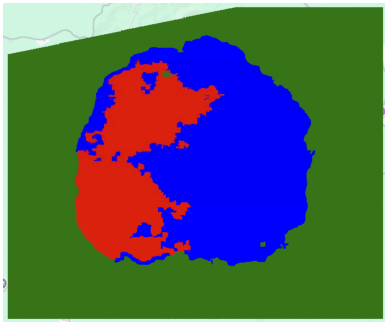

(c) Classification Result

Figure 5.19: Bosomtwe 2020-05-28

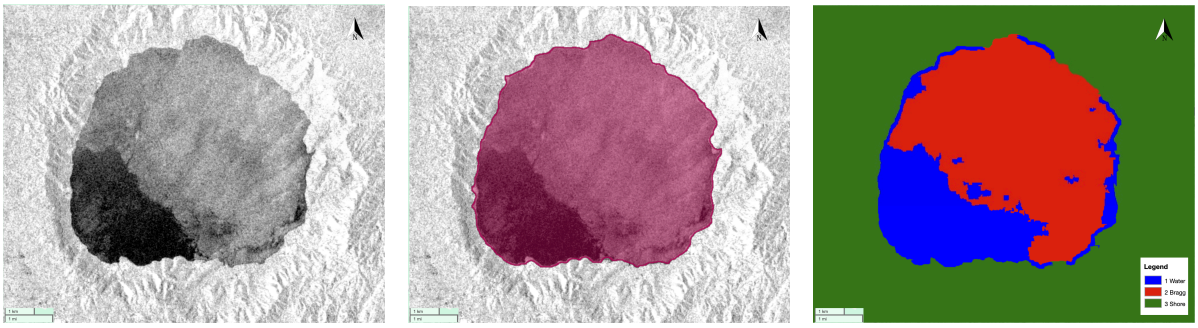

(a) Sentinel-1 Image (VV) **(b)** Computed Outline **(c)** Classification Result

Figure 5.20: Bosomtwe 2021-03-06

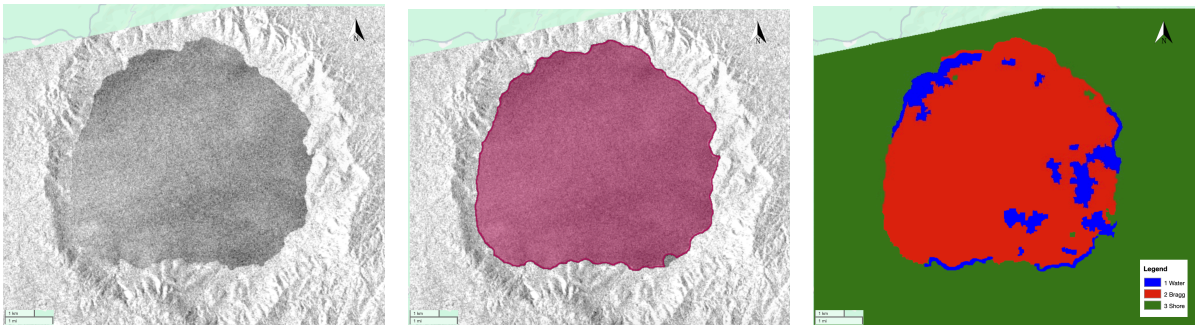

(a) Sentinel-1 Image (VV) **(b)** Computed Outline **(c)** Classification Result

Figure 5.21: Bosomtwe 2022-03-07

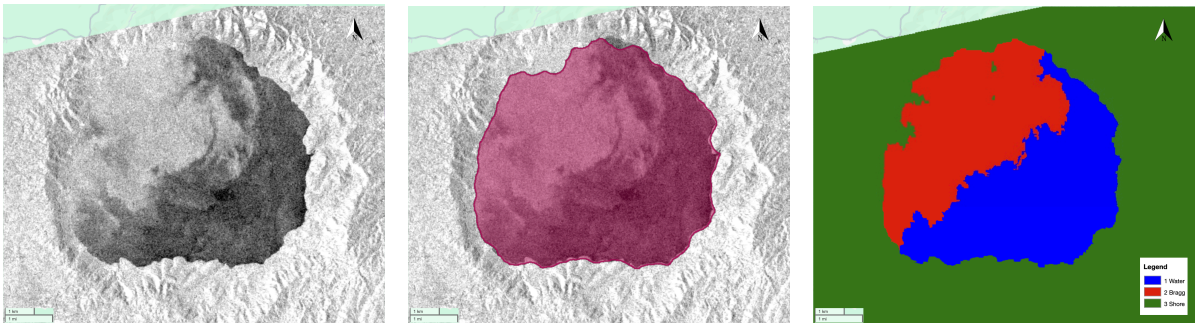

(a) Sentinel-1 Image (VV) **(b)** Computed Outline **(c)** Classification Result

Figure 5.22: Bosomtwe 2022-03-19

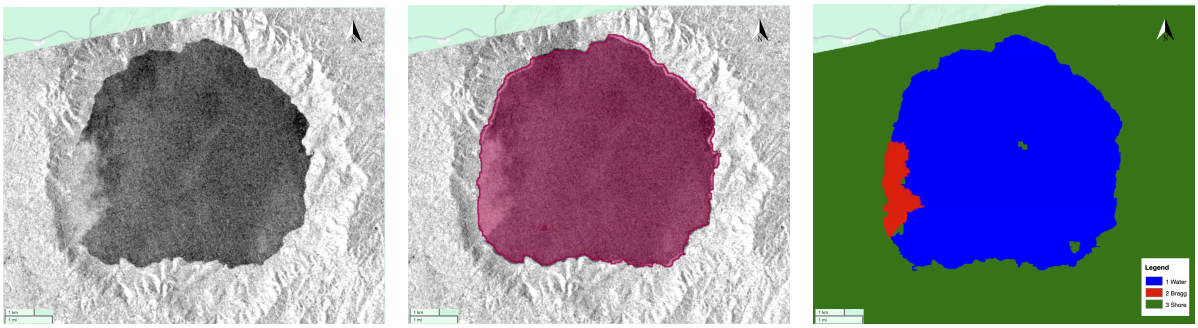

(a) Sentinel-1 Image (VV) **(b)** Computed Outline **(c)** Classification Result

Figure 5.23: Bosomtwe 2022-03-31

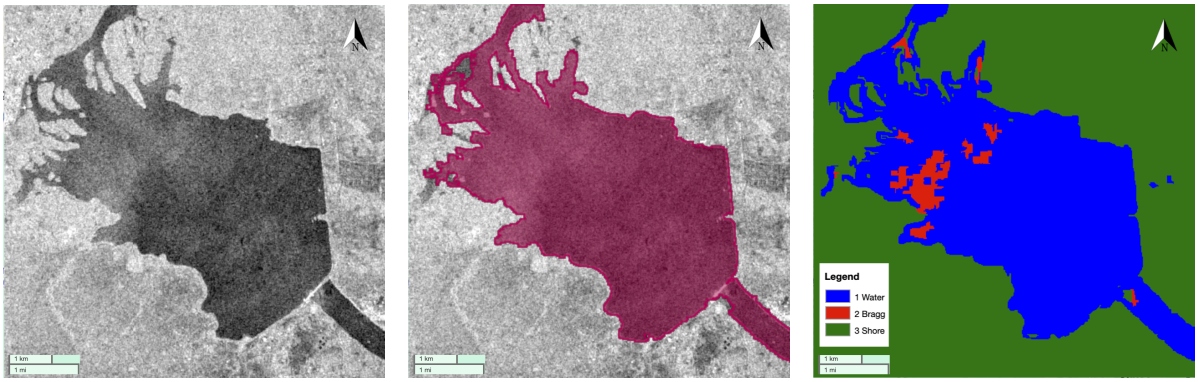

(a) Sentinel-1 Image (VV) **(b)** Computed Outline **(c)** Classification Result

Figure 5.24: Kpong 2019-02-27

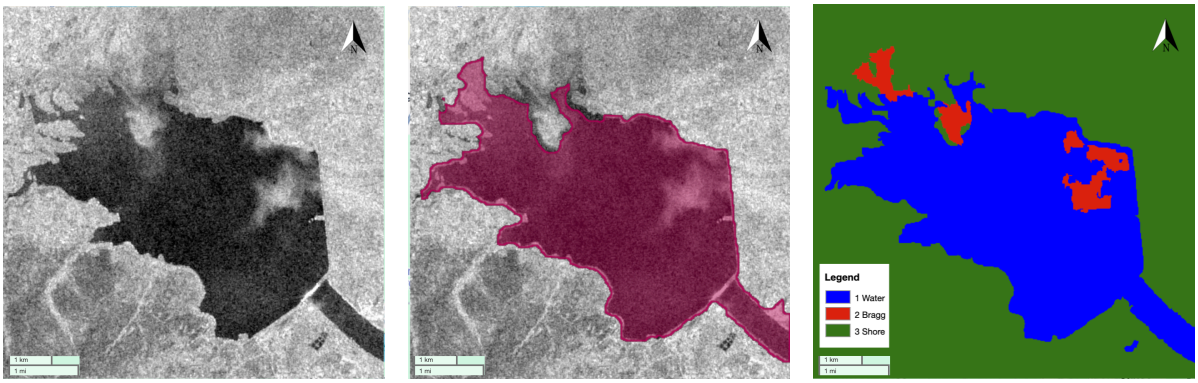

(a) Sentinel-1 Image (VV) **(b)** Computed Outline **(c)** Classification Result

Figure 5.25: Kpong 2021-08-27

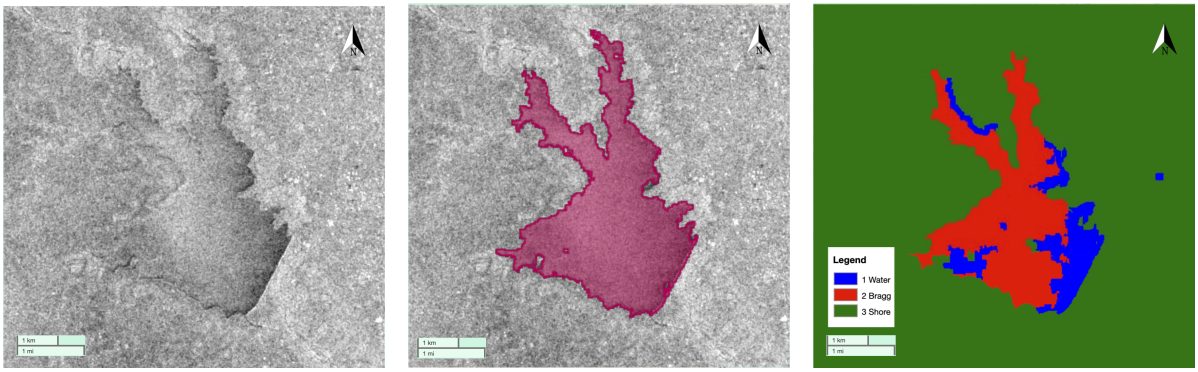

(a) Sentinel-1 Image (VV) **(b)** Computed Outline **(c)** Classification Result

Figure 5.26: Tono 2020-05-04

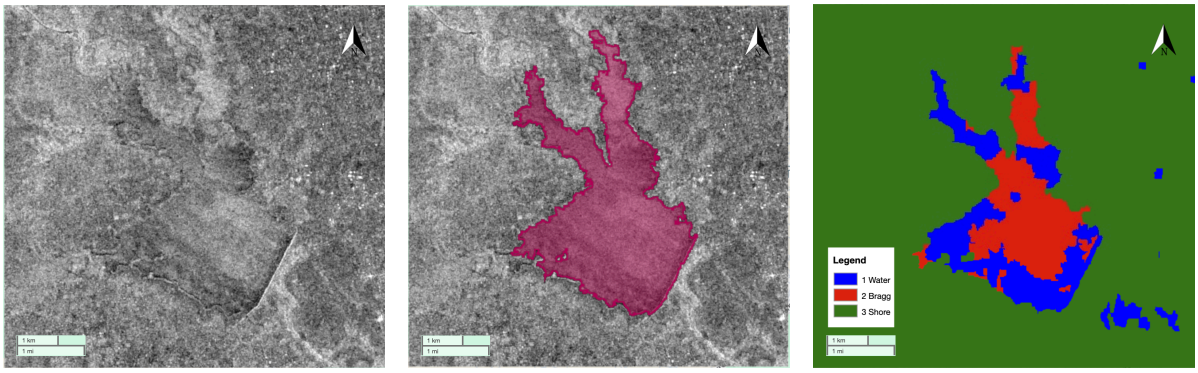

(a) Sentinel-1 Image (VV) **(b)** Computed Outline **(c)** Classification Result

Figure 5.27: Tono 2020-05-10

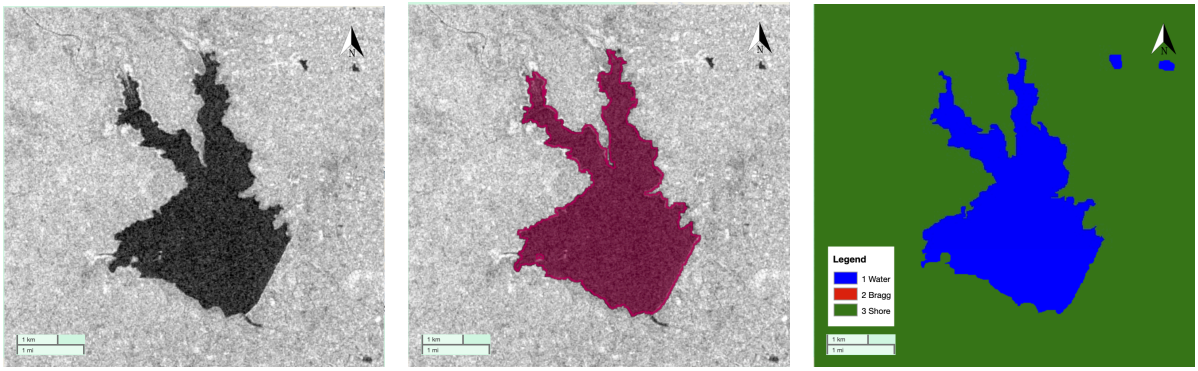

(a) Sentinel-1 Image (VV) **(b)** Computed Outline **(c)** Classification Result

Figure 5.28: Tono 2021-08-27

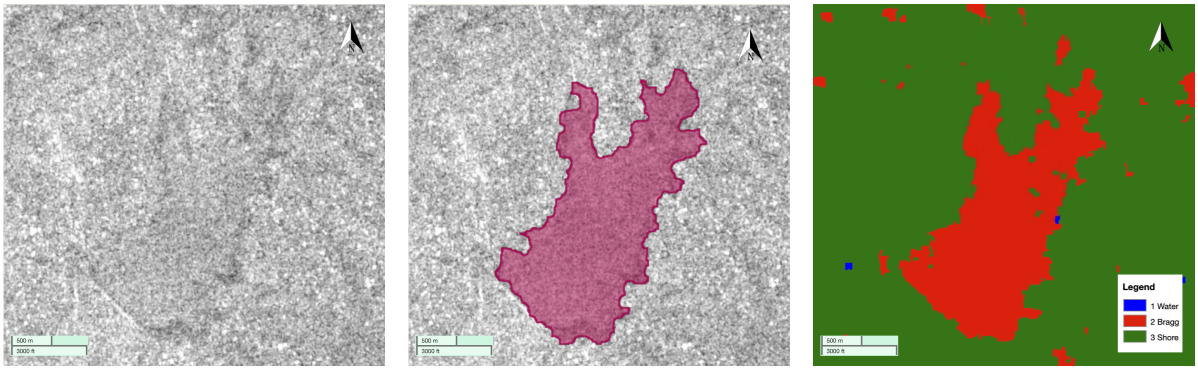

(a) Sentinel-1 Image (VV) **(b)** Computed Outline **(c)** Classification Result

Figure 5.29: Vea 2020-05-10

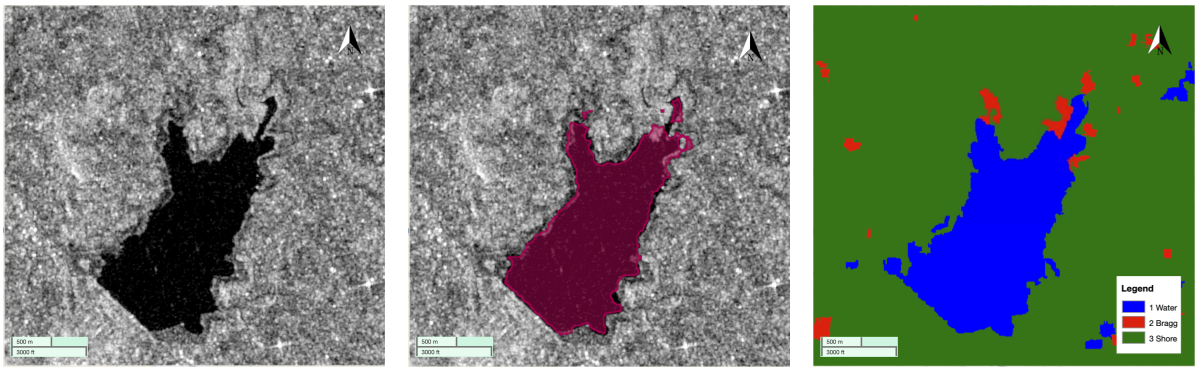

(a) Sentinel-1 Image (VV) **(b)** Computed Outline **(c)** Classification Result

Figure 5.30: Vea 2021-02-28

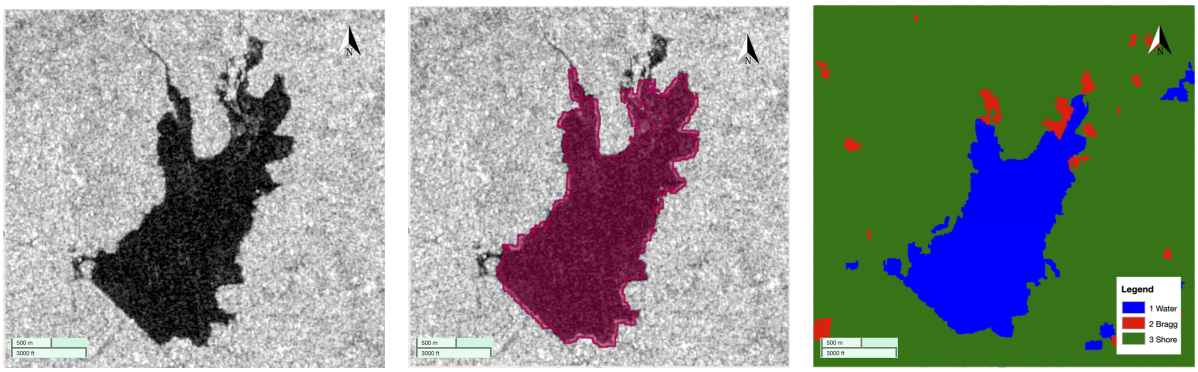

(a) Sentinel-1 Image (VV) **(b)** Computed Outline **(c)** Classification Result

Figure 5.31: Vea 2021-08-27

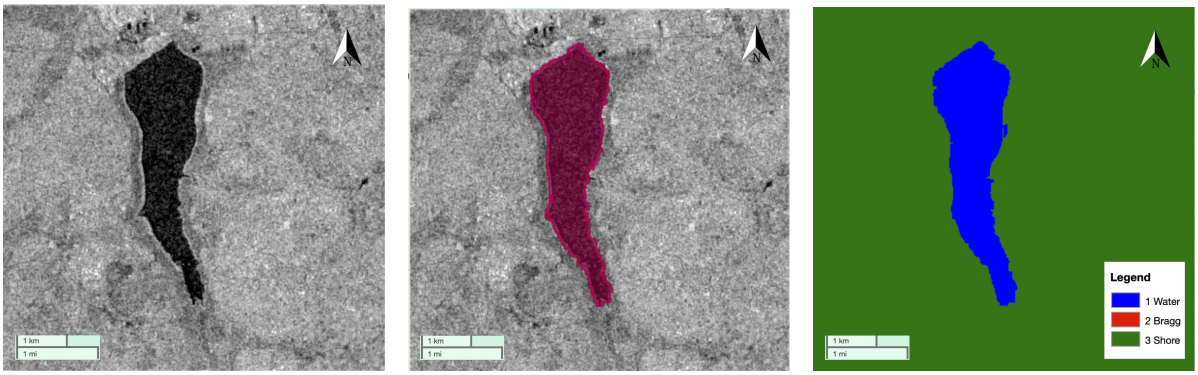

(a) Sentinel-1 Image (VV) **(b)** Computed Outline **(c)** Classification Result

Figure 5.32: Voggo 2020-05-04

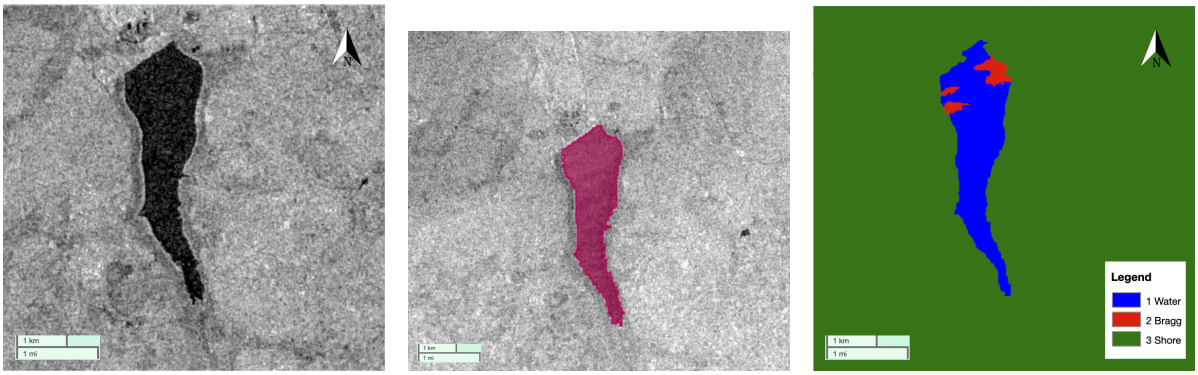

(a) Sentinel-1 Image (VV) **(b)** Computed Outline **(c)** Classification Result

Figure 5.33: Voggo 2020-05-10

Evaluating the results of the classifications based on accuracy assessment parameters alone have been discussed previously in section 5.2, as have the drawbacks of such an approach. That is why the results provided in figures 5.19 till 5.33 are discussed based on the visual output rather than accuracy assessment.

As we can see in the images, classification has yielded mixed results. Especially in images with fading, feather-like Bragg scattering patches, e.g. figures 5.19, 5.20, 5.21 and 5.27, we see that not the entirety of the Bragg patch is classified correctly, but rather the most intense, whitest patches, whereas the slightly darker patches are classified as normal water cover. This could, in part, be explained by the fact that, for such images, the entire reservoir is more or less hazy. Hence, the differences in backscatter intensity for the mean and median superpixels are much less pronounced, and although the mean and median superpixel values could indicate Bragg scattering or the absence thereof, the standard deviation superpixels, which are also trained on images in which the Bragg scattering is much more pronounced, do not. This assumption is supported by the classification result provided in figure 5.21, where the reservoir is almost entirely covered by Bragg scattering of approximate equal brightness and intensity.

It seems that smaller reservoirs, such as Tono, Voggo and Vea, are classified relatively well. The tentative assumption had been that these reservoirs especially would under-perform compared to larger reservoirs, such as Bosomtwe and Kpong. Naturally, since these smaller reservoirs have a smaller surface area, this means that any boundary errors, small artifacts or misclassified superpixels have a relatively larger impact on the total miss-classification error. However, judging from figures 5.26 till 5.33, the classification of Bragg patches and the delineation of the reservoir outline is performed to relative satisfaction. The final accuracy scores for the applied machine learning model are summerized in the table below (table 5.3).

Table 5.3: Accuracy Model

Overall Accuracy	Kappa Coefficient
0.9834	0.9685

Effect Size Superpixel

Note should be taken to the relevance of the 'SuperPixelSize' parameter in the success of the classification. The 'SuperPixelSize' parameter has been discussed previously in section 4.4. Classification of Bragg scattering patches on larger reservoirs (Bosomtwe, Kpong) generally show a higher degree of success if a larger 'SuperPixelSize' is applied, and vice versa.

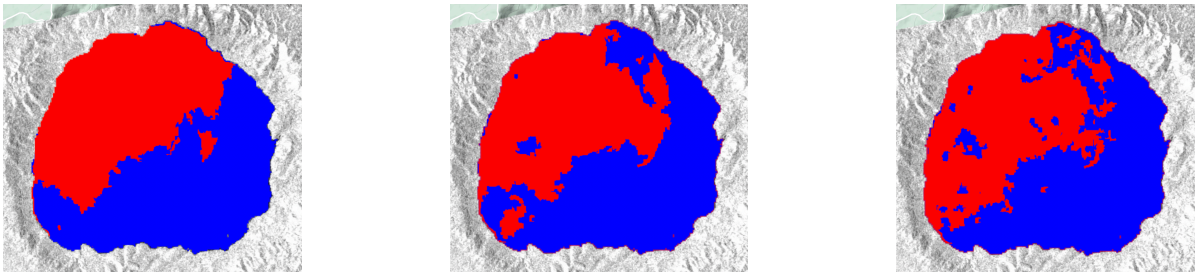

(a) SuperPixelSize at 50 **(b)** SuperPixelSize at 30 **(c)** SuperPixelSize at 15

Figure 5.34: Effect SuperPixelSize on Bosomtwe 2022-03-19 Classification Result

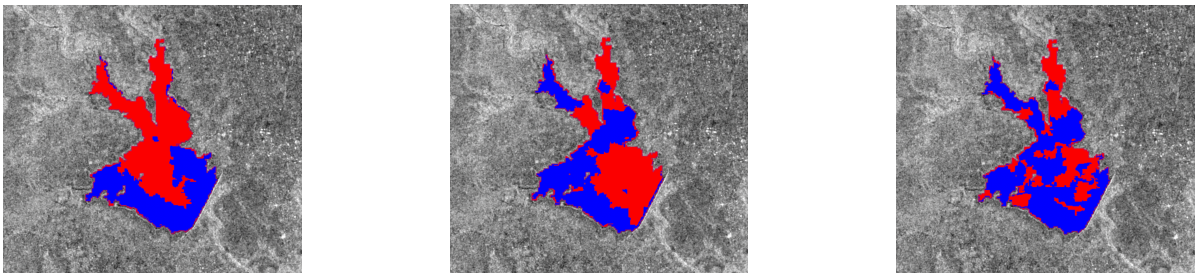

(a) SuperPixelSize at 50 **(b)** SuperPixelSize at 30 **(c)** SuperPixelSize at 15

Figure 5.35: Effect SuperPixelSize on Tono 2020-05-10 Classification Result

The parameters relevant to SNIC superpixel segmentation have been previously discussed in chapter 4 Methods. Throughout the training and classification process, all the parameters relevant to the SNIC superpixel segmentation - apart from the SuperPixelSize - have been kept identical. The effect of changing the SuperPixelSize parameter on the classification process has been illustrated in images 5.34 and 5.35. This SuperPixelSize parameter translates to the superpixel seed location spacing, measured in pixels. As we are dealing with imagery with a resolution of $10\mathrm{m}$, the demonstrated SuperPixelSizes of $15\,\mathrm{px}$, $30\,\mathrm{px}$ and $50\,\mathrm{px}$, provided in images 5.34 and 5.35, translate to a seed spacing of respectively $150\,\mathrm{m}$, $300\,\mathrm{m}$ and $500\,\mathrm{m}$.

As we can see in the six images provided above, applying a higher SuperPixelSize will result in larger, more logical Bragg scattering patches that agglometerate together, and vice versa applying a smaller SuperPixelSize will result in a smaller, more patchy Bragg scattering classification.

There is no single right answer as to which SuperPixelSize is the right fit, but by applying different SuperPixelSizes for all reservoirs, on different radar images, a general consensus was reached as to which SuperPixelSize best fits each reservoir. Because the classification program was built with the intention for it to be used on a broader spectrum than just the reservoirs used during classification, comparison of chosen SuperPixelSize and reservoir surface area yielded the rule-of-thumb provided in table 5.4.

Table 5.4: Superpixel sizes by reservoir size

description	size range ha	superpixel size px
small	<2000	15
medium	2000 - 4000	30
large	>4000	50

5.6. Quality of Outline and Surface Area

In finding the best way to approximate reservoir outlines and surface area, more than one way was tried. Initially, an outline-algorithm was employed to approximate surface area and reservoir outline, based on past and future Sentinel-1 imagery and known approximate outline. This method was eventually not employed, given that it relied to heavily on the availability of Sentinel-1 imagery both before and after the date of interest, as well as initial information on the approximate reservoir outline and location, making the method to dependent on external factors and not allowing classification to happen in real-time.

The reason the result of this outline-finding algorithm are still discussed is because they yielded more accurate results than the outline-finding method employed now, which used the classification result. Hence, the quality of the results are still discussed.

As elaborated on before in section 4.4.4, the effects of seasonality on reservoir surface areas is most prominently reflected in reservoirs with smaller surface areas. To this extent, the quality of the outline-finding algorithm was tested with specific attention to smaller reservoirs. To make inspection easier, the computed outline will be compared with both the relevant SAR imagery and, if available, a Sentinel-2 True Color composite (RGB).

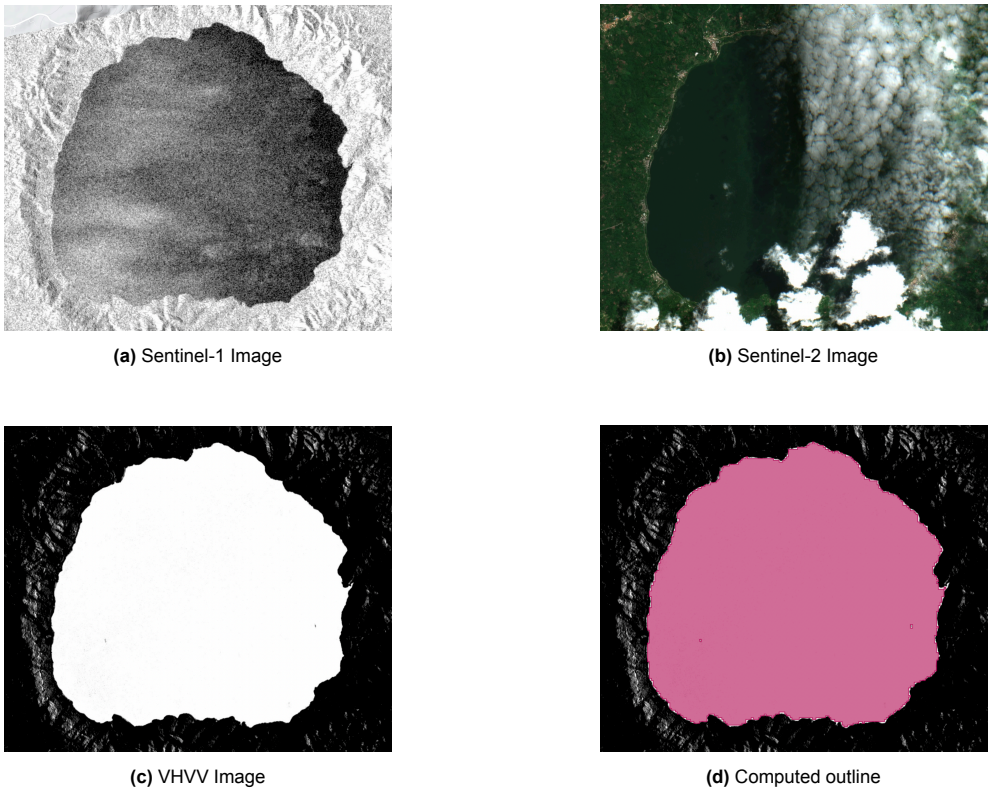

(a) Sentinel-1 Image

(b) Sentinel-2 Image

(c) VHVV Image

(d) Computed outline

Figure 5.36: Bosomtwe 2020-05-28

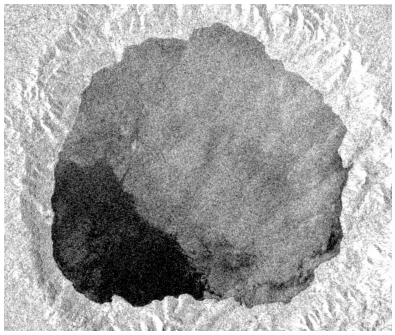

(a) Sentinel-1 Image

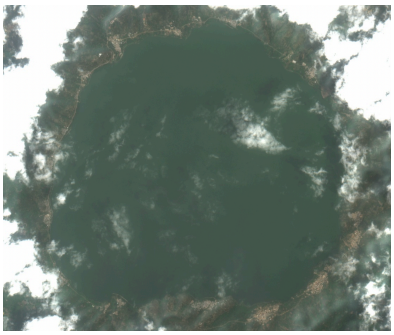

(b) Sentinel-2 Image

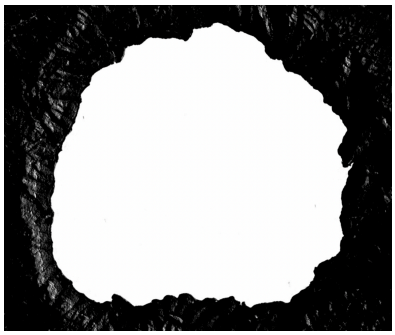

(c) VHVV Image

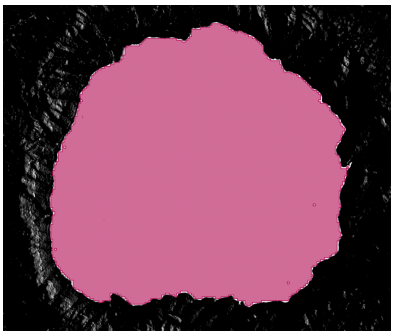

(d) Computed outline

Figure 5.37: Bosomtwe 2021-03-06

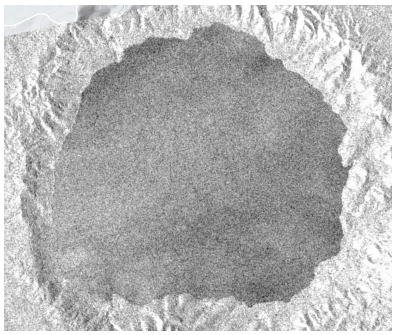

(a) Sentinel-1 Image

(b) Sentinel-2 Image

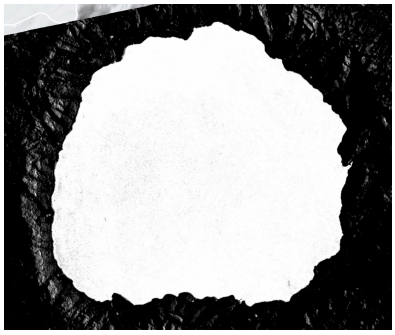

(c) VHVV Image

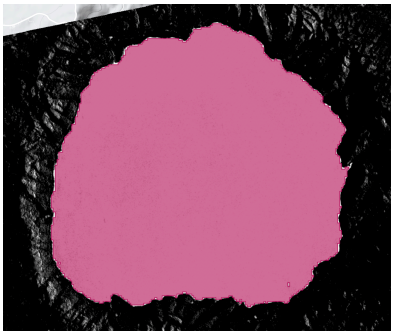

(d) Computed outline

Figure 5.38: Bosomtwe 2022-03-07

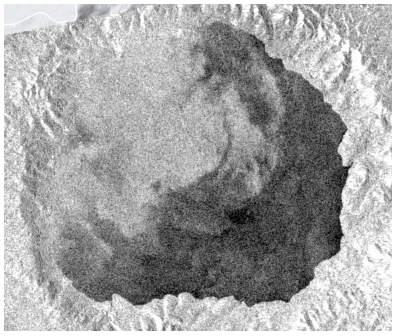

(a) Sentinel-1 Image

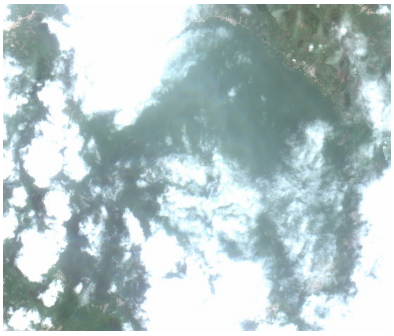

(b) Sentinel-2 Image

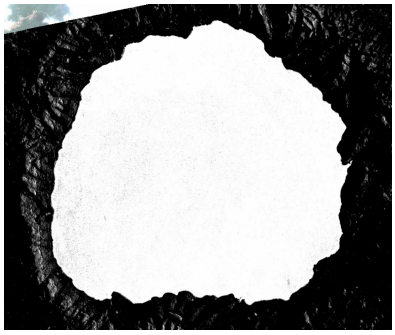

(c) VHVV Image

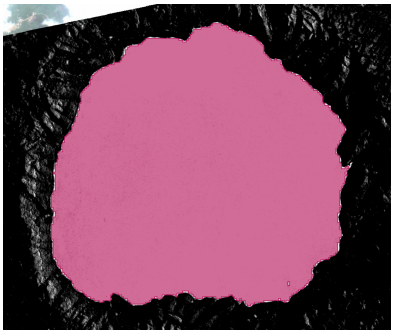

(d) Computed outline

Figure 5.39: Bosomtwe 2022-03-19

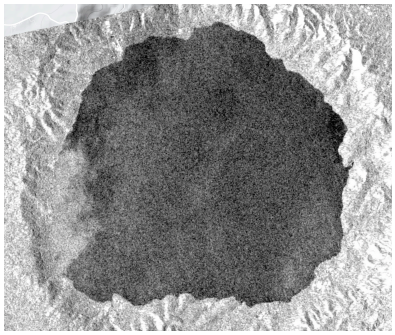

(a) Sentinel-1 Image

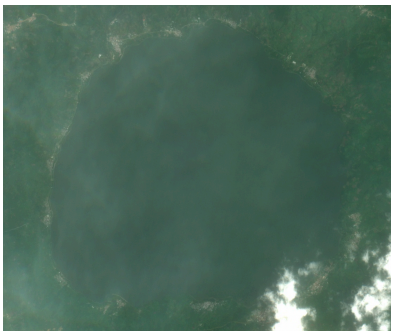

(b) Sentinel-2 Image

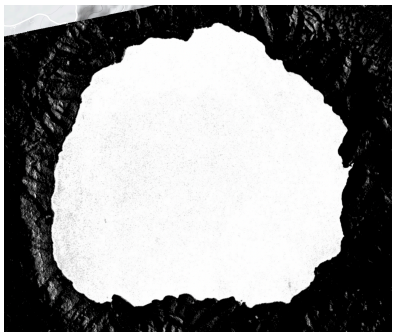

(c) VHVV Image

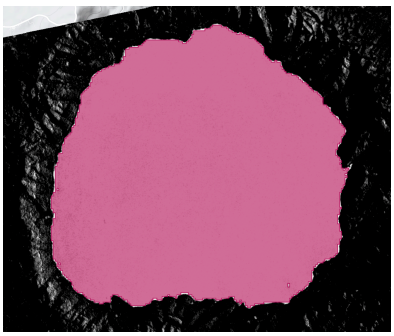

(d) Computed outline

Figure 5.40: Bosomtwe 2022-03-31

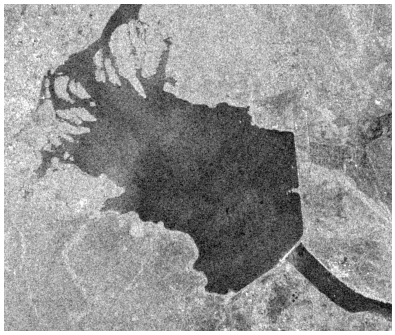

(a) Sentinel-1 Image

(b) Sentinel-2 Image

(c) VHVV Image

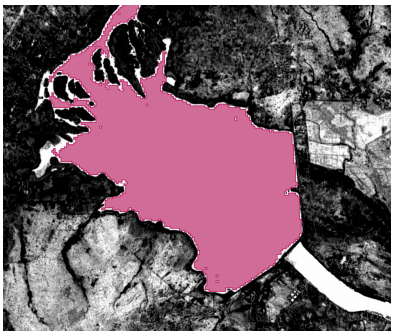

(d) Computed outline

Figure 5.41: Kpong 2019-02-27

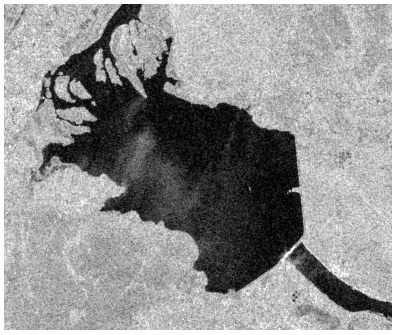

(a) Sentinel-1 Image

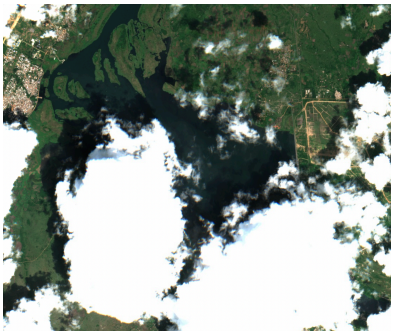

(b) Sentinel-2 Image

(c) VHVV Image

(d) Computed outline

Figure 5.42: Kpong 2019-10-25

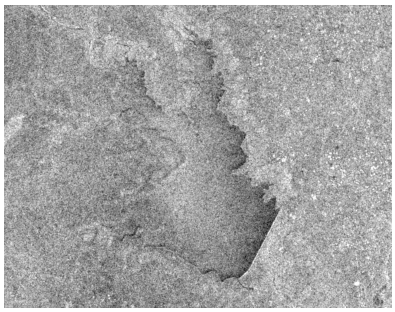

(a) Sentinel-1 Image

(b) Sentinel-2 Image

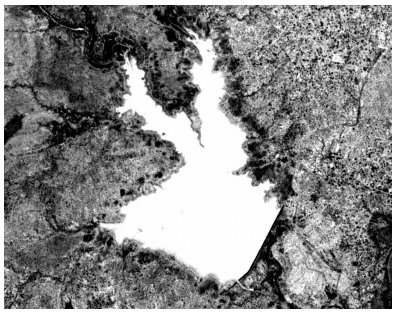

(c) VHVV Image

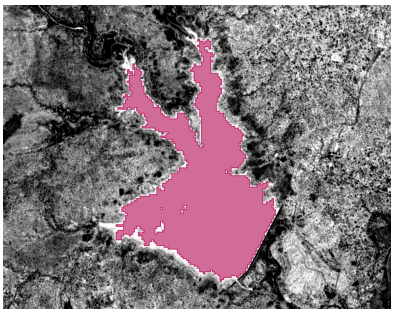

(d) Computed outline

Figure 5.43: Tono 2020-05-04

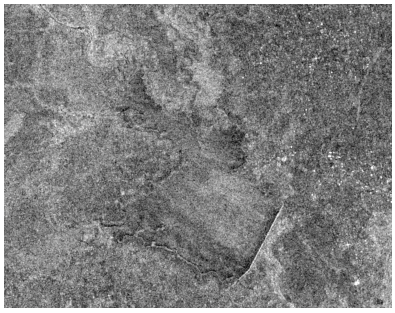

(a) Sentinel-1 Image

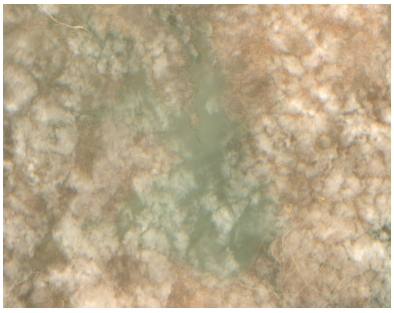

(b) Sentinel-2 Image

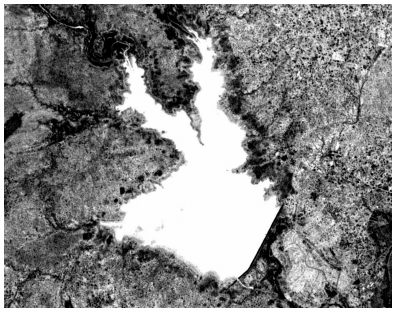

(c) VHVV Image

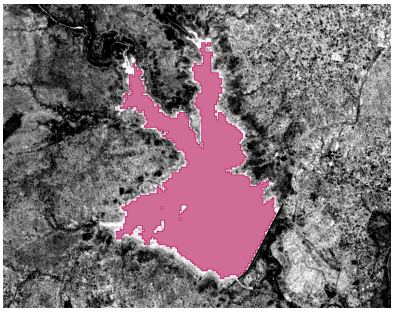

(d) Computed outline

Figure 5.44: Tono 2020-05-10

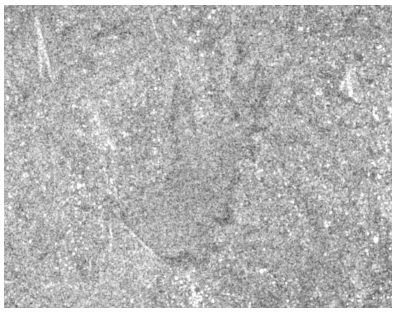

(a) Sentinel-1 Image

(b) Sentinel-2 Image

(c) VHVV Image

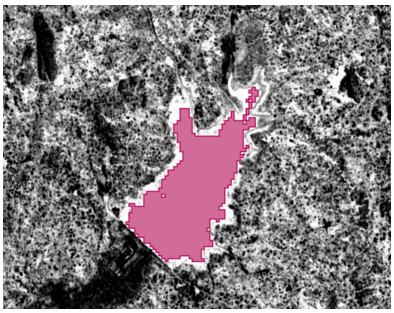

(d) Computed outline

Figure 5.45: Vea 2020-05-10

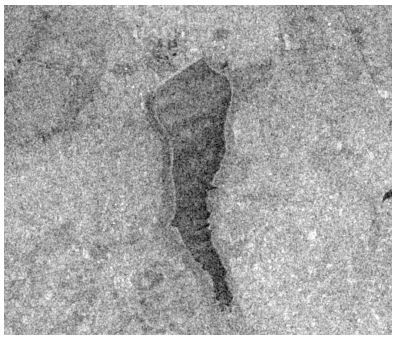

(a) Sentinel-1 Image

(b) Sentinel-2 Image

(c) VHVV Image

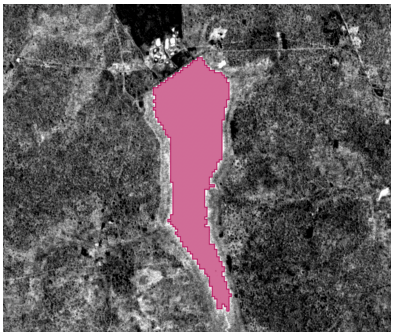

(d) Computed outline

Figure 5.46: Voggo 2020-05-10

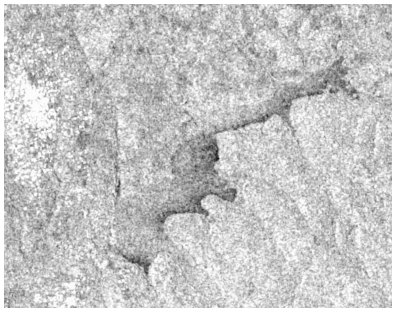

(a) Sentinel-1 Image

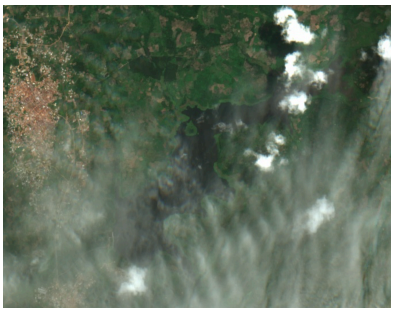

(b) Sentinel-2 Image

(c) VHVV Image

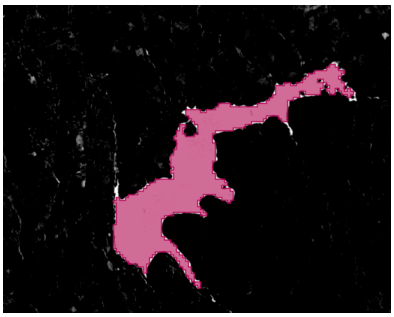

(d) Computed outline

Figure 5.47: Barekese 2020-05-28

(a) Sentinel-1 Image

(b) Sentinel-2 Image

(c) VHVV Image

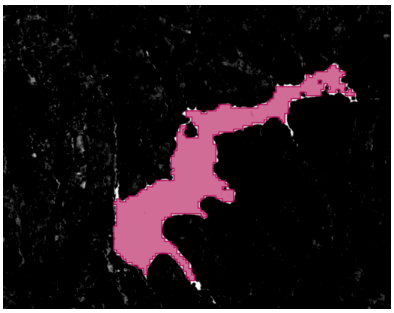

(d) Computed outline

Figure 5.48: Barekese 2021-01-29

In the images 5.36 to 5.48, the results of the outline compilation is provided. As was to be expected, the algorithm performs especially well for larger reservoirs, with smoother, regular outlines, such as the Bosomtwe lake. Here, small miss-identifications and boundary problems impact the final results to a

relatively smaller extent. For lake Bosomtwe, the algorithm performed especially well. The amount of wrongly identified water/land measured below 0.5% of total reservoir area. At its worst, the computed outline came short of the actual reservoir outline at only 45 m.

The Kpong reservoir proved exemplary for what circumstances can challenge the outline-finding algorithm, with the small, intertwining and delta-like structures of the streams in the north-western part of the reservoir. Due to this problem, a consequent shrinking and growing operation is applied to the computed outline geometry. This proved effective to remove smaller specks and inconsistencies still present in the geometry. In table 5.5, the accuracy of the outline-finding algorithm is summarized. In the collection of images in figures 5.36 to 5.48, the functioning of the algorithm is showed, using the Sentinel-1 and Sentinel-2 imagery on the selected date, computed VHVV image and the computed outline.

Table 5.5: Percentage incorrectly masked water surface

	Average % Classified Incorrectly
Bosomtwe	null
Kpong	1.71
Tono	6.94
Vea	1.24
Voggo	2.34
Barekese	1.37

When compared to the outlines and reservoir surface areas computed by using the classification results, a difference in surface area of 4.98% is observed. In conclusion, the original outline-finding algorithm yielded more accurate outline and surface area results, but lacks in terms of independence on additional user input and knowledge, as well as the fact that it can only be successfully employed on past (approximately two month old) imagery.

6

Discussion

This discussion consists of two parts. The first section, section 6.1 will evaluate the wider context in which the research takes place. Section 6.2 discusses the assumptions and choices that were made during the research, and to what extent they could have influenced the results and their accuracy.

6.1. Usage of Sentinel-1

This research aims to provide further insight in the automatic detection of Bragg scattering patches over reservoirs. The region of focus during this research was the West-African country of Ghana. For this purpose, an open-source code was written in the GEE environment, available through Github and GEE, that utilizes the freely available Sentinel-1 imagery in combination with the methodology developed in this thesis.

Research into this facet of remote sensing and water resource management contributes to the development of technology that is better able to automate the processing and interpretation of SAR imagery, which could greatly impact the manner in which un-gauged water resources can be managed and water quantities can be recorded. In addition, it contributes to the fundamental research on supervised image classification and delineation of reservoirs with remotely sensed radar data.

6.1.1. How does the performance of this model score?

The results of this research seem to confirm the hypothesis that applying a non-parametric Random Forest classifier over open-water reservoirs functions as the best option for the detection of Bragg scattering patches. The Random Forest classifier provided a higher Overall Accuracy (98.34%) and Kappa Coefficient (96.85%) than other inspected classifiers, such as a CART classifier or a SVM. The OA and KC scores for the CART and SVM classifiers were provided in section 5.2, table 5.1, as were the output results in figures 5.1 till 5.6.

6.1.2. What is the potential of Sentinel-1 data using a Random Forest classifier to identify Bragg scattering presence over open-water reservoirs in Ghana?

The classifications made by the Random Forest computed and trained in this research - constructed using 40 trees and using information from the Sentinel-1 VV and VH bands, as well as derivative products such as entropy and GLCM texture metrics - reached Overall Accuracies of (98.34%) and Kappa Coefficients of (96.85%). According to this accuracy assessment, which uses a confusion matrix, this would indicate the classification to be very successful.

However, judging by the classification images produced in chapter 5, there is still a certain amount of error present in the result that is not properly reflected in the outcome of the accuracy assessment and confusion matrix. The main reason for this issue is thought to be found in the uneven distribution of the three classes, with unaffected water and shore being much more abundantly present in the data than Bragg scattering.

6.2. Reflection on results

The results of this research show that the utilized method and collection of data provide a relatively accurate result compared to the intended classification goal. Naturally however, the research method is based on several assumptions. These assumptions influence the quality of the classification outcome. In this section, those assumptions are discussed in a critical manner and are placed in the context of previously published research.

6.2.1. Sentinel-1 data for Bragg scattering classification over reservoirs

A central point of discussions concerning this research is whether the phenomenon being studied is compatible with the chosen classification method. Other studies and papers on the subject published previously have underlined the complexity of Bragg scattering in the context of reservoir or water surface area delineation. This complexity mainly lies in the gradual nature in which Bragg scattering is present in radar imagery. As mentioned previously, Bragg scattering can present itself in different shades of intensity and different shapes, ranging from stark, distinct boundaries to fading feather-like edges. With this lack of clear Bragg scattering patches boundaries, there is a complexity in the assigning of classes.

In addition, the size of small reservoirs, present especially in the Northern part of Ghana, can provide difficulty. These reservoirs, which are relied on for fishing, irrigation, livestock watering and domestic and commercial purposes, are characterized by their small size (smaller than $100\ \mathrm{ha}$) and wide distribution [7]. With the given Sentinel-1 resolution of $10\ \mathrm{m}$, small reservoirs with surface areas up to $100\ \mathrm{ha}$ consist of up to $10\,000\ \mathrm{px}$ maximum.

With the presence of speckle and the usage of SNIC superpixels during the classification process, larger Bragg scattering patches on small reservoirs might quickly take up a large part of the reservoir. This might interfere with the used method that takes into account mean, median and standard deviation values for the SNIC superpixels to detect Bragg scattering. A workable solution could be to simply assign a smaller value to the 'size' parameter, but this would lead to computation time-outs when working with larger reservoirs.

6.2.2. Pre-Processing

The Sentinel-1 SAR GRD product has proven its reliability for image classification in various studies, given its independence in terms of day/night or the presence of clouds, as is the case with Sentinel-2 and other comparable optical products [57, 15, 74, 122, 19, 16, 109].

6.2.3. Speckle Filtering

One of the challenges in handling Sentinel-1 SAR data lies in the inherent presence of speckle, caused by the interference of waves reflected from many elementary scatterers. Speckle will present itself on SAR imagery as granular noise and can hence be a limiting factor in imaging systems. By applying multi-look processing in GEE, they try to correct standard noise and reduce the effect of speckle [68].

Since this study uses GEE multi-look processed Sentinel-1 data, a speckle filter was not applied. This might offer a partial explanation as to why Bragg scattering patches on larger lakes show a lower error and generally display a higher accuracy level, as we are dealing with larger-scale distinguishable features. This concept was previously noticed by Dasari et al., who detected that the same large-scale features that are distinguishable on images affected by speckle noise, can be severely compromised on a smaller scale [25]. Because we are working with SNIC superpixels, however, the effect of noise and speckle has already been limited.

6.2.4. Use of data for classification

Given that we are dealing with a supervised classification method, a collection of training and validation data is required. In any case, accuracy assessment is performed to assess the quality of the classification results. This accuracy assessment, which has been discussed previously, can be affected by various factors.

Quality of the reference data

As mentioned previously in chapter 5 on results, we are dealing with an unbalanced dataset, with an distribution that is unequal. Due to this, the machine learning algorithm may be biased [14]. Additionally,

we must consider that the training and validation data are not obtained using a randomly distributed sampling strategy. As this is the case, several studies have found that this can lead to an optimistic bias in classification and, more importantly, an inflated accuracy outcome [51].

These two biases have to be considered in the interpretation of the results and the accuracy assessment. As stated before, the training data consists of features selected from between 2018-2022. Given the rarity of Bragg scattering to occur, the training (and validation) sets are therefore unequally balanced in favor of clear imagery. This has the consequence that the model appears to be biased towards this most sampled class.

Feature selection of the classifier

In this study, a Random Forest classifier was utilized. In essence, this Random Forest functions like a black box model: it consists of an ensemble of single decision trees, each with a certain depth and a certain number of nodes, making analysis difficult. For full transparency as to how predictions and classification results are created, every single decision tree would have to be analyzed at an individual level. This was not done in this study, with the consequence that it is not clear on which basis or what information the Random Forest classifier assesses class.

It is assumed that the classification result is based on the difference in median, mean and standard deviation of the backscatter responses per SNIC superpixel, as well as the computed entropy and GLCM values. The classifier was analyzed to some extent during the tuning of the hyperparameters. But again, this was done while regarding the Random Forest as a black box, and these results were based on differences in Overall Accuracy and Kappa Coefficient, as well as the classification results provided as images.

6.2.5. Use of SNIC superpixels

During this research a superpixel-based classification method was used, rather than choosing a pixel-based approach. A pixel-based classification approach is generally significantly more affected by the presence of speckle. The superpixel-based approach usually uses the average values of all pixels inside the superpixel, and in this case utilizes the standard deviation and median values too, thus reducing the negative impact of speckle noise.

Superpixelsize greatly impacts the classification outcome of Bragg scattering detection and should be chosen carefully. If a superpixel is too large, the superpixel may contain both classes, reducing the classification accuracy. The other way around, Yang et al. found that choosing a superpixelsize that is too small will result in a reduced superpixel segmentation efficiency, and the resulting superpixel may only contain a few pixels, given the resolution of the used imagery. Since we are dealing with SAR imagery, and thus the presence of speckle should be taken into regards, choosing a superpixelsize that is too small could result in the classification of non-relevant speckle noise, rather than the Bragg scattering patches that we are actually interested in [124].

6.2.6. Use of the GEE environment

The methodology developed in this research was translated into code making use of the GEE environment to execute classification. The GEE is a cloud-based platform that allows for geo-spatial analysis, and was chosen for usage due to its ease of use and the lack of performance requirements for the users hardware. There are several drawbacks, as well as advantages to the usage of GEE, which will be discussed here.

The main advantage to the use of GEE lies in its easy usage and accessibility. As a cloud-based platform, it lessens the reliance on high speed processors or extensive storage capacities. With the large catalog of satellite imagery and derivative products available, there is a lot of pre-processing already provided, solving the problem of hectic and time-consuming processing steps. For the Sentinel-1 product, GEE hosts the GRD data pre-processed with ESA's SNAP software. With SAR products, the pre-processing can be especially complex, making the availability of pre-processed products a special advantage.

On the other hand, there are some serious limitations to the GEE platform. Most prominently and pressing: the training process of Machine Learning or Deep Learning algorithms is limited to 100MB

of data. This limit was not reached during this specific research, but with Deep Learning algorithms especially, where an even larger training data set is required, this limit might cause problems.

Additionally, and relevant to the current topic of research, image classification in Remote Sensing could potentially be improved considerably by the usage of object-based image analysis. However, currently there is not an efficient and accurate segmentation algorithm available within GEE. On the same topic of image classification, GEE is limited to selected data mining models for classification and regression algorithms, such as CART, RF and SVMs. Furthermore, in the context of algorithms, GEE utilizes a lot of algorithms that are not entirely transparent and, on a process level, function much like a black-box, making analysis difficult.

7

Conclusions and Recommendations

In this chapter, any conclusions that can be drawn from the analysis of the results are laid out and discussed in section 7.1. Based on these conclusions, recommendations are made for further research and the detection of Bragg scattering and monitoring of water reservoirs in section 7.2.

7.1. Conclusions

7.1.1. What is the potential of Sentinel-1 SAR data to map Bragg scattering over reservoirs?

The results of this research show that the used method provides a reasonably accurate result with regards to the intended classification goal. The various factors that contribute to this conclusions are discussed further.

Classification using a combination of the non-parametric RF, a SNIC approach and the additional use of the outline-finding algorithms discussed previously provide a higher Overall Accuracy (98.34%) and Kappa Coefficient (96.85%) than usage of a CART classifier or a SVM, which score 98.01% (OA) and 96.38% (KC) and 85.09% (OA) and 72.53% (KC) respectively. This conclusion is supported by the classification output, produced by the various tested classifiers and provided in the figures in chapter 5. Therefore, it appears that the RF classifier is preferred over the other classifiers for processing this type of data.

However, the Overall Accuracy has shown to be a biased classification accuracy assessor, due to the distribution of classes in the training and validation set. Hence, the results of the classification process were assessed visually too. These maps showed the RF output to be more coherent than CART output, and confirm that, generally, the RF is better able to detect the Bragg scattering patches over reservoirs than the CART classifier.

7.1.2. To what extent does the developed classifier contribute to the practice of reservoir delineation in Ghana?

The final classifier is able to relatively accurately detect Bragg scattering over water reservoirs in Ghana and differentiate between unaffected surface water, Bragg scattering patches and surrounding shore. With the computed classification results, we are thus able to determine the amount of Bragg scattering present in an SAR image, fulfilling the initial wish to automatically flag images that are severely affected by Bragg scattering.

Additionally, the classifier is able to take the computed classification output and vectorize this into a shoreline geometry that proved to be sufficiently accurate. In doing so, the final classifier is able to delineate reservoirs and compute reservoir surface area on a collection of images, regardless of the presence of Bragg scattering. In doing so, this allows for a more continuous monitoring of the small and medium reservoirs of Ghana that is not labor-intensive and free of cost.

Even if the final classifier is not applied to achieve this goal, the information and knowledge regarding the most relevant and effective GLCM features and the added value of applying SNIC superpixels can contribute to the effectivity and efficiency of future delineation algorithms.

7.1.3. To what extent is the GEE environment appropriate for this research?

As discussed previously, there are both advantages and disadvantages to employing the GEE environment. Given the type of classification performed and the type of classifiers used (CART, RF, SVM), the limitations do not severely impact the manner in which the research was conducted. However, it does impose a limit on which other options could be investigated while using the same GEE framework. The fact that Sentinel-1 imagery is made available in near real-time and with the appropriate pre-processing already applied allows for quick and easy analysis of new imagery within the same program.

Additionally, the ability for functionality for open-source fusion with a Python API and the Python Geemap package allows for relatively easy use within Python. This easy accessibility, in combination with the low performance requirements for the users computer make for the conclusion that the GEE platform is an appropriate choice for the research conducted.

7.2. Recommendations

Recommendations for identifying Bragg scattering patches over reservoirs in Ghana are provided in two areas: the first section discusses what has been researched to design the methodology in this study, and which, for various reasons, did not work. The second section suggests a few ways in terms of follow-up research that could improve upon the current classification strategy.

7.2.1. Development of the methodology

To design the methodology for this study, several other things were researched and attempted, which, for a variety of reasons, did not function and were hence not integrated in the final methodology. A quick listing of these attempts are given here.

Plotting of VV and VH backscatter intensities and comparing the characteristics of these VV versus VH plots was investigated. An example of the plots used in this approach is provided in figure 7.1. Additionally, using a more traditional, pixel-based approach (rather than the currently used SNIC-based approach) was employed to classify and delineate Bragg scattering patches. Also, using the readily available Sentinel-2 and Landsat imagery was tried, as to approximate reservoir outlines. These methods listed above have thus already been examined but have proven ineffective in regards of reaching the goal of Bragg scattering classification over Ghanaian reservoirs, or delivered results that were subpar to the methods currently employed. It is therefore not recommended to investigate these methods further in order to improve on the Bragg scattering classification problem.

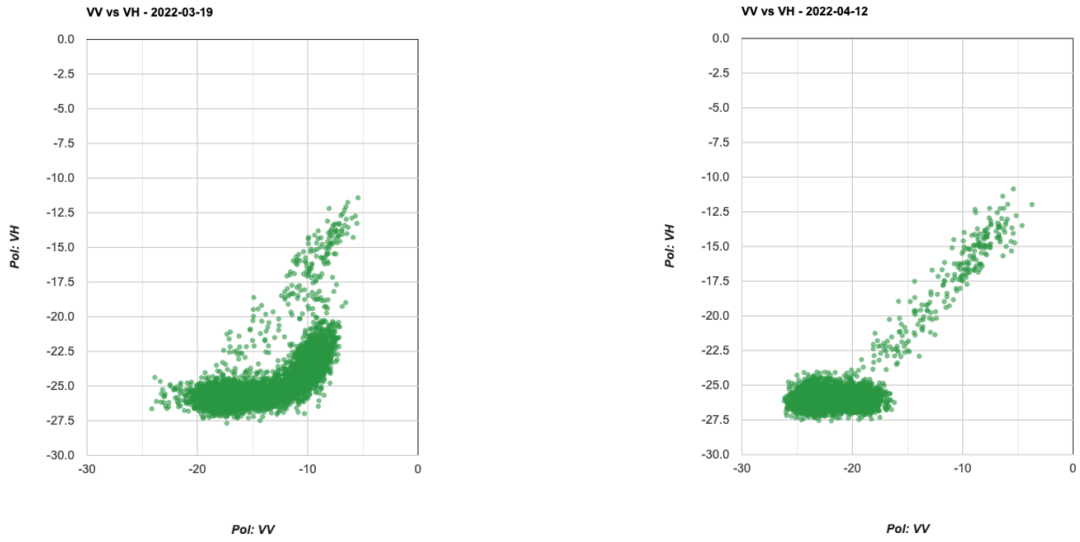

(a) VV vs. VH 2022-03-19

(b) VV vs. VH 2022-04-12

Figure 7.1: VV vs. VH Plots Examples

7.2.2. Further Research

Working with imbalanced data

The dataset used in this study is characterized by a high degree in variability, in terms of backscatter intensity and a binary classification label. As mentioned previously, the manner in which the two classification labels are distributed is imbalanced, as non-Bragg information is much more readily available than information in which Bragg scattering is present. The effect of this imbalance can be seen in the classification result and the accuracy assessment. More consideration could there be given to other, more advanced forms of image classification and accuracy assessments with imbalanced datasets.

It has been shown that dataset imbalance can exert a major impact on the value and meaning of accuracy and performance [77, 100]. Using a weighted confusion matrix for the RF ensemble classifier could be investigated. Apart form using a weighted confusion matrix that is better suited to an imbalanced dataset, other forms of accuracy assessment could be further researched. In a broader sense, using different sampling techniques could be investigated, that are especially suited to working with the imbalanced data, such as iterative sampling methods or sampling methods that work with the creation of synthetic data in order to provide a balanced distribution [30, 82].

A similar approach could be pursued on a classifier-level. In that manner, existing algorithms could be adapted to the problem of imbalanced datasets. To achieve that, more in-depth knowledge about the nature and predictors that cause its failure in minority class recognition is required. One such possibility could be further research into one-class classification, which in essence can learn the concepts of the minority class by treating majority objects as outliers [100].

Speckle filter for small areas

It would be recommended to look into the use of a more advanced speckle filter for the Sentinel-1 imagery. Because we are, even for the small reservoirs, dealing with relatively large objects, the required buffer zone required for speckle filters - usually consisting of only a few pixels - is not expected to cause a real loss of information. Filters that could be further investigated include the Lee filter, the refined Lee filter or a Boxcar filter. Naturally, other available filters or techniques to reduce the presence of speckle could also be researched [125, 67].

Integration of Sentinel-2 Imagery or Wind Data

It could be a possibility to further investigate using Sentinel-2 imagery. Usage of Sentinel-2 imagery was researched in the context of the outline-finding algorithm, but was not pursued in the context of general Bragg scattering detection. As the combination of Sentinel-1 and Sentinel-2 has previously been used plenty in the detection and delineation of reservoirs, further efforts to research the potential of using Sentinel-2 to better detect Bragg scattering on Sentinel-1 imagery could surely be worth it [125, 67].

For images in which a significant portion of the reservoir is covered by Bragg scattering, Sentinel-2 imagery could possibly be used to verify whether the classification result and derived reservoir outline is accurate, given that usable Sentinel-2 data at a date close to the date the Sentinel-1 image was taken is available.

Additionally, it could be investigated if integrating wind data from the TAHMO wind stations mentioned earlier is possible. Comparisons could be made on dates on which the classifier flags for a significant amount of Bragg scattering, to see if general rules-of-thumb could be made for wind speeds and orientations, to see if that yields a pattern.

Deep Learning

Due to the restrictions that working with the GEE environment poses, the available Machine Learning techniques applied are limited. The GEE is capable of processing large amounts of data and imagery, but he computations and application of Deep Learning models are not supported. Although decision tree models have shown to provide reasonably accurate results, research into Land Use and Land Cover (LULC) has shown that Deep Learning models, such as Convolutional Neural Networks (CNNs) and Recurrent Neural Networks (RNNs) provide even higher accuracies [90]. Especially CNNs proved to excel in the classification of water bodies in LULC research. In the adjacent fields of oil spill classification and water quality classification and prediction, the usage of CNNs is widely and successfully applied [39, 24, 83]. Using such Deep Learning techniques were naturally researched during the development of the methodology, but due to its unavailability in GEE it was not further pursued. Previous research by Li et al. [73] employed a methodology that combined the usage of local Deep Learning training and GEE cloud-based big data computing to empower GEE with Deep Learning computing power. Such methods could be further investigated.

References

[1] Radhakrishna Achanta and Sabine Susstrunk. “Superpixels and polygons using simple non-iterative clustering”. In: *Proceedings of the IEEE conference on computer vision and pattern recognition*. 2017, pp. 4651–4660.

[2] Radhakrishna Achanta et al. “Scale-adaptive superpixels”. In: *26th Color and Imaging Conference Final Program and Proceedings*. Society for Imaging Science and Technology. 2018, pp. 1–6.

[3] Daniel Acheampong et al. “Asssesing the effectiveness and impact of agricultural water management interventions: the case of small reservoirs in northern Ghana”. In: *Agricultural Water Management* 209 (2018), pp. 163–170.

[4] Mohammed Sarfaraz Gani Adnan et al. “Improving spatial agreement in machine learning-based landslide susceptibility mapping”. In: *Remote Sensing* 12.20 (2020), p. 3347.

[5] Ghana. Environmental Protection Agency. *Ghana’s Second National Communication to the UNFCCC.* Environmental Protection Agency, 2011.

[6] Douglas E Alsdorf, Ernesto Rodríguez, and Dennis P Lettenmaier. “Measuring surface water from space”. In: *Reviews of Geophysics* 45.2 (2007).

[7] FO Annor. “Small Reservoirs in Northern Ghana: Monitoring, Physical Processes, and Management”. In: (2023).

[8] Frank Ohene Annor et al. “Delineation of small reservoirs using radar imagery in a semi-arid environment: A case study in the upper east region of Ghana”. In: *Physics and Chemistry of the Earth, Parts A/B/C* 34.4-5 (2009), pp. 309–315.

[9] Felix A Asante and Franklin Amuakwa-Mensah. “Climate change and variability in Ghana: Stocktaking”. In: *Climate* 3.1 (2014), pp. 78–101.

[10] J Balajee and MA Saleem Durai. “Detection of water availability in SAR images using deep learning architecture”. In: *International Journal of System Assurance Engineering and Management* (2021), pp. 1–10.

[11] Donald E Barrick and William H Peake. *Scattering from surfaces with different roughness scales, analysis and interpretation*. Tech. rep. 1967.

[12] William Lawrence Bragg. “The Specular Reflection of X-rays.” In: *Nature* 90.2250 (1912), pp. 410–410.

[13] Facundo Bre, Juan M Gimenez, and Víctor D Fachinotti. “Prediction of wind pressure coefficients on building surfaces using artificial neural networks”. In: *Energy and Buildings* 158 (2018), pp. 1429–1441.

[14] Johannes Breidenbach et al. “Prediction of species specific forest inventory attributes using a nonparametric semi-individual tree crown approach based on fused airborne laser scanning and multispectral data”. In: *Remote Sensing of Environment* 114.4 (2010), pp. 911–924.

[15] B Brisco et al. “A semi-automated tool for surface water mapping with RADARSAT-1”. In: *Canadian Journal of Remote Sensing* 35.4 (2009), pp. 336–344.

[16] Brian Brisco. “Mapping and monitoring surface water and wetlands with synthetic aperture radar”. In: *Remote Sensing of Wetlands: Applications and Advances* (2015), pp. 119–136.

[17] Brian Brisco et al. “Water resource applications with RADARSAT-2–a preview”. In: *International Journal of Digital Earth* 1.1 (2008), pp. 130–147.

[18] Canada Centre for Mapping and Earth Observation. *Radar Polarimetry*. 2015. URL: `https://www.nrcan.gc.ca/maps-tools-and-publications/satellite-imagery-and-air-photos/satellite-imagery-products/educational-resources/tutorial-radar-polarimetry/9579` (visited on 01/12/2023).

[19] Han Cao et al. “Operational Lake Mapping on the Southern Tibet Using Sentinel-1 DATA”. In: *IGARSS 2019-2019 IEEE International Geoscience and Remote Sensing Symposium*. IEEE. 2019, pp. 4040–4043.

[20] Mark L Carroll et al. “A new global raster water mask at 250 m resolution”. In: *International Journal of Digital Earth* 2.4 (2009), pp. 291–308.

[21] Wei Chen et al. “Spatial prediction of landslide susceptibility using an adaptive neuro-fuzzy inference system combined with frequency ratio, generalized additive model, and support vector machine techniques”. In: *Geomorphology* 297 (2017), pp. 69–85.

[22] Richard W Conners, Mohan M Trivedi, and Charles A Harlow. “Segmentation of a high-resolution urban scene using texture operators”. In: *Computer vision, graphics, and image processing* 25.3 (1984), pp. 273–310.

[23] Corinna Cortes and Vladimir Vapnik. “Support-vector networks”. In: *Machine learning* 20 (1995), pp. 273–297.

[24] K Das, P Janardhan, and H Narayana. “Application of CNN based image classification technique for oil spill detection”. In: *Indian Journal of Geo-Marine Sciences (IJMS)* 52.01 (2023), pp. 05–14.

[25] Kiran Dasari et al. “Importance of speckle filtering in image classification of SAR data”. In: *2015 International Conference on Microwave, Optical and Communication Engineering (ICMOCE)*. IEEE. 2015, pp. 349–352.

[26] Neil N Davis et al. “The Global Wind Atlas: A high-resolution dataset of climatologies and associated web-based application”. In: *Bulletin of the American Meteorological Society* 104.8 (2023), E1507–E1525.

[27] Paco López Dekker. “Lecture Module 2: Synthetic Aperture Radar Fundamentals for CIE4609”. In: *Technical University Delft* (2021).

[28] Gennadii Donchyts et al. “High-resolution surface water dynamics in Earth’s small and medium-sized reservoirs”. In: *Scientific reports* 12.1 (2022), p. 13776.

[29] Dirk Eilander et al. “Remotely sensed monitoring of small reservoir dynamics: A Bayesian approach”. In: *Remote Sensing* 6.2 (2014), pp. 1191–1210.

[30] William Elazmeh, Nathalie Japkowicz, and Stan Matwin. “Evaluating misclassifications in imbalanced data”. In: *Machine Learning: ECML 2006: 17th European Conference on Machine Learning Berlin, Germany, September 18-22, 2006 Proceedings 17*. Springer. 2006, pp. 126–137.

[31] EO Portal. *ALOS-4 (Advanced Land Observing Satellite-4)*. 2022. URL: https://www.eoportal.org/satellite-missions/alos-4#palsar3 (visited on 01/18/2023).

[32] EO Portal. *COSMO-SkyMed - Second Generation*. 2014. URL: https://www.eoportal.org/satellite-missions/cosmo-skymed-second-generation#Cosmo2G.html.3 (visited on 01/18/2023).

[33] ESA. *Sentinel-1*. 2025. URL: https://www.esa.int/Applications/Observing_the_Earth/Copernicus/Sentinel-1 (visited on 04/26/2025).

[34] European Environment Agency. *ECRINS (European Catchments and RIvers Network System)*. 2012. URL: http://projects.eionet.europa.eu/ecrins (visited on 01/19/2024).

[35] European Space Agency. *About TerraSAR-X and TanDEM-X*. 2022. URL: https://earth.esa.int/eogateway/missions/terrasar-x-and-tandem-x (visited on 01/18/2023).

[36] European Space Agency. *Mission ends for Copernicus Sentinel-1B satellite*. 2022. URL: https://www.esa.int/Applications/Observing_the_Earth/Copernicus/Sentinel-1/Mission_ends_for_Copernicus_Sentinel-1B_satellite (visited on 01/15/2023).

[37] European Space Agency. *Sentinel-1 Observation Scenario*. 2022. URL: https://sentinels.copernicus.eu/web/sentinel/missions/sentinel-1/observation-scenario (visited on 01/15/2023).

[38] FAO. *Ghana at a glance*. URL: https://www.fao.org/ghana/fao-in-ghana/ghana-at-a-%glance/en/ (visited on 11/13/2023).

[39] David M Feinauer et al. “Oil spill identification using deep convolutional neural networks”. In: *2022 14th International Conference on Computational Intelligence and Communication Networks (CICN)*. IEEE. 2022, pp. 240–245.

[40] Alan H Fielding and John F Bell. “A review of methods for the assessment of prediction errors in conservation presence/absence models”. In: *Environmental conservation* 24.1 (1997), pp. 38–49.

[41] Federico Filipponi. “Sentinel-1 GRD preprocessing workflow”. In: *Multidisciplinary digital publishing institute proceedings* 18.1 (2019), p. 11.

[42] Giles M Foody. “Explaining the unsuitability of the kappa coefficient in the assessment and comparison of the accuracy of thematic maps obtained by image classification”. In: *Remote sensing of environment* 239 (2020), p. 111630.

[43] Benjamin Ghansah et al. “Mapping the spatial changes in Lake Volta using multitemporal remote sensing approach”. In: *Lakes & Reservoirs: Research & Management* 21.3 (2016), pp. 206–215.

[44] Benjamin Ghansah et al. “Mapping the spatial distribution of small reservoirs in the White Volta Sub-basin of Ghana”. In: *Remote Sensing Applications: Society and Environment* 9 (2018), pp. 107–115.

[45] Nick van de Giesen, Rolf Hut, and John Selker. “The trans-African hydro-meteorological observatory (TAHMO)”. In: *Wiley Interdisciplinary Reviews: Water* 1.4 (2014), pp. 341–348.

[46] Google Earth Engine. *Sentinel-1 Preprocessing*. 2022. URL: https://developers.google.com/earth-engine/guides/sentinel1#sentinel-1-preprocessing (visited on 01/19/2023).

[47] Google Earth Engine. *Sentinel-1 SAR GRD: C-band Synthetic Aperture Radar Ground Range Detected (log scaling)*. 2022. URL: https://developers.google.com/earth-engine/datasets/catalog/COPERNICUS_S1_GRD#description (visited on 01/19/2023).

[48] Noel Gorelick et al. “Google Earth Engine: Planetary-scale geospatial analysis for everyone”. In: *Remote sensing of Environment* 202 (2017), pp. 18–27.

[49] Government of Canada. *Radar Image Properties*. 2015. URL: https://www.nrcan.gc.ca/maps-tools-and-publications/satellite-imagery-and-air-photos/tutorial-fundamentals-remote-sensing/microwave-remote-sensing/radar-image-properties/9299 (visited on 02/13/2023).

[50] Thomas Hahmann and Birgit Wessel. “Surface water body detection in high-resolution TerraSAR-X data using active contour models”. In: *8th European Conference on Synthetic Aperture Radar*. VDE. 2010, pp. 1–4.

[51] TO Hammond and DL Verbyla. “Optimistic bias in classification accuracy assessment”. In: *International Journal of Remote Sensing* 17.6 (1996), pp. 1261–1266.

[52] Robert M Haralick, Karthikeyan Shanmugam, and Its’ Hak Dinstein. “Textural features for image classification”. In: *IEEE Transactions on systems, man, and cybernetics* 6 (1973), pp. 610–621.

[53] Simon Haykin. *Neural networks and learning machines, 3/E*. Pearson Education India, 2009.

[54] Kaiming He et al. “Deep residual learning for image recognition”. In: *Proceedings of the IEEE conference on computer vision and pattern recognition*. 2016, pp. 770–778.

[55] Floyd M Henderson and Anthony J Lewis. *Principles and applications of imaging radar. Manual of remote sensing, volume 2.* Wiley, 1998.

[56] FM Henderson. “Environmental factors and the detection of open surface water areas with X-band radar imagery”. In: *International Journal of Remote Sensing* 16.13 (1995), pp. 2423–2437.

[57] Laura L Hess, John M Melack, and David S Simonett. “Radar detection of flooding beneath the forest canopy: a review”. In: *International Journal of Remote Sensing* 11.7 (1990), pp. 1313–1325.

[58] Fred K Hoehler. “Bias and prevalence effects on kappa viewed in terms of sensitivity and specificity”. In: *Journal of clinical epidemiology* 53.5 (2000), pp. 499–503.

[59] MS Horritt, DC Mason, and AJ Luckman. “Flood boundary delineation from synthetic aperture radar imagery using a statistical active contour model”. In: *International Journal of Remote Sensing* 22.13 (2001), pp. 2489–2507.

[60] DA Hughes. “Facing a future water resources management crisis in sub-Saharan Africa”. In: *Journal of Hydrology: Regional Studies* 23 (2019), p. 100600.

[61] HydroSHEDS. *HydroLAKES*. 2024. URL: `https://www.hydrosheds.org/products/hydrolakes` (visited on 01/19/2024).

[62] Olena Kavats, Dmitriy Khramov, and Kateryna Sergieieva. “Surface Water Mapping from SAR Images Using Optimal Threshold Selection Method and Reference Water Mask”. In: *Water* 14.24 (2022), p. 4030.

[63] John R Kendra, Kamal Sarabandi, and Fawwaz T Ulaby. “Radar measurements of snow: Experiment and analysis”. In: *IEEE Transactions on Geoscience and Remote Sensing* 36.3 (1998), pp. 864–879.

[64] Alex Krizhevsky, Ilya Sutskever, and Geoffrey E Hinton. “Imagenet classification with deep convolutional neural networks”. In: *Advances in neural information processing systems* 25 (2012).

[65] Yann LeCun, Corinna Cortes, and CJ Burges. “MNIST handwritten digit database”. In: *ATT Labs [Online]. Available: http://yann.lecun.com/exdb/mnist* 2 (2010).

[66] Jong-Sen Lee and Eric Pottier. *Polarimetric radar imaging: from basics to applications*. CRC press, 2017.

[67] Jong-Sen Lee et al. “Polarimetric SAR speckle filtering and the extended sigma filter”. In: *IEEE Transactions on geoscience and remote sensing* 53.3 (2014), pp. 1150–1160.

[68] Jong-Sen Lee et al. “Speckle filtering of synthetic aperture radar images: A review”. In: *Remote sensing reviews* 8.4 (1994), pp. 313–340.

[69] Bernhard Lehner and Petra Döll. “Development and validation of a global database of lakes, reservoirs and wetlands”. In: *Journal of hydrology* 296.1-4 (2004), pp. 1–22.

[70] Bernhard Lehner et al. “High-resolution mapping of the world’s reservoirs and dams for sustainable river-flow management”. In: *Frontiers in Ecology and the Environment* 9.9 (2011), pp. 494–502.

[71] Stef Lhermitte. *Lecture Remote Sensing and Convolutional Neural Networks for CS4305TU*. Oct. 2021.

[72] Haifeng Li. *Smile*. `https://haifengl.github.io`. 2014.

[73] Kai Li et al. “Deep learning empowers the Google Earth Engine for automated water extraction in the Lake Baikal Basin”. In: *International Journal of Applied Earth Observation and Geoinformation* 112 (2022), p. 102928.

[74] Jens R Liebe et al. “Suitability and limitations of ENVISAT ASAR for monitoring small reservoirs in a semiarid area”. In: *IEEE Transactions on Geoscience and remote Sensing* 47.5 (2008), pp. 1536–1547.

[75] Jens Reiner Liebe. “Hydrology of small reservoirs in semi-arid northern Ghana”. In: (2009).

[76] Tsung-Yi Lin et al. “Microsoft coco: Common objects in context”. In: *Computer Vision–ECCV 2014: 13th European Conference, Zurich, Switzerland, September 6-12, 2014, Proceedings, Part V 13*. Springer. 2014, pp. 740–755.

[77] Amalia Luque et al. “The impact of class imbalance in classification performance metrics based on the binary confusion matrix”. In: *Pattern Recognition* 91 (2019), pp. 216–231.

[78] Masoud Mahdianpari, Bahram Salehi, and Fariba Mohammadimanesh. “The effect of PolSAR image de-speckling on wetland classification: introducing a new adaptive method”. In: *Canadian Journal of Remote Sensing* 43.5 (2017), pp. 485–503.

[79] Rodrigo Manzanas et al. “Precipitation variability and trends in Ghana: An intercomparison of observational and reanalysis products”. In: *Climatic change* 124 (2014), pp. 805–819.

[80] Samuel McCandless Jr. and Christopher Jackson. “Chapter 1. Principles of Synthetic Aperture Radar”. In: *Synthetic aperture radar: marine user’s manual*. United States, National Environmental Satellite, Data, Information Service., Office of Research, and Applications, 2004, pp. 110–127.

[81] Makarius Victor Mdemu. “Water productivity in medium and small reservoirs in the Upper East Region (UER) of Ghana”. PhD thesis. Universitäts-und Landesbibliothek Bonn, 2008.

[82] Andrew Mellor et al. “Using ensemble margin to explore issues of training data imbalance and mislabeling on large area land cover classification”. In: *2014 IEEE International Conference on Image Processing (ICIP)*. IEEE. 2014, pp. 5067–5071.

[83] Haobin Meng et al. “Classification of inland lake water quality levels based on Sentinel-2 images using convolutional neural networks and spatiotemporal variation and driving factors of algal bloom”. In: *Ecological Informatics* 80 (2024), p. 102549.

[84] Mathis Loïc Messager et al. “Estimating the volume and age of water stored in global lakes using a geo-statistical approach”. In: *Nature communications* 7.1 (2016), p. 13603.

[85] Franz Meyer. “Spaceborne Synthetic Aperture Radar: Principles, data access, and basic processing techniques”. In: *Synthetic Aperture Radar (SAR) Handbook: Comprehensive Methodologies for Forest Monitoring and Biomass Estimation* (2019), pp. 21–64.

[86] P Mohanaiah, P Sathyanarayana, and L GuruKumar. “Image texture feature extraction using GLCM approach”. In: *International journal of scientific and research publications* 3.5 (2013), pp. 1–5.

[87] Waytehad Rose Moskolaï, Wahabou Abdou, and Albert Dipanda. “A Workflow for Collecting and Preprocessing Sentinel-1 Images for Time Series Prediction Suitable for Deep Learning Algorithms”. In: *Geomatics* 2.4 (2022), pp. 435–456.

[88] Natural Resources Canada. *CanVec Hydrography: Waterbody Features.* 2013. URL: `ftp://ftp2.cits.rncan.gc.ca/pub/canvec/` (visited on 01/19/2024).

[89] Christopher Ndehedehe. “Remote Sensing Hydrology”. In: *Satellite Remote Sensing of Terrestrial Hydrology*. Springer, 2022, pp. 3–17.

[90] Anam Nigar et al. “Comparison of machine and deep learning algorithms using Google Earth Engine and Python for land classifications”. In: *Frontiers in Environmental Science* 12 (2024), p. 1378443.

[91] Thais Mayumi Oshiro, Pedro Santoro Perez, and José Augusto Baranauskas. “How many trees in a random forest?” In: *Machine Learning and Data Mining in Pattern Recognition: 8th International Conference, MLDM 2012, Berlin, Germany, July 13-20, 2012. Proceedings 8*. Springer. 2012, pp. 154–168.

[92] Kwadwo Owusu, Peter Waylen, et al. “Trends in spatio-temporal variability in annual rainfall in Ghana (1951-2000)”. In: *Weather* 64.5 (2009), p. 115.

[93] Kwadwo Owusu and Peter R Waylen. “The changing rainy season climatology of mid-Ghana”. In: *Theoretical and applied climatology* 112 (2013), pp. 419–430.

[94] Seth Owusu et al. “The significance of small reservoirs in sustaining agricultural landscapes in dry areas of West Africa: A review”. In: *Water* 14.9 (2022), p. 1440.

[95] Aniceto Panetti et al. “GMES Sentinel-1: Mission and satellite system overview”. In: *EUSAR 2012; 9th European Conference on Synthetic Aperture Radar*. VDE. 2012, pp. 162–165.

[96] Edward Park et al. “A pathway to the automated global assessment of water level in reservoirs with synthetic aperture radar (SAR)”. In: *Remote Sensing* 12.8 (2020), p. 1353.

[97] Amy L Parker et al. “Applications of satellite radar imagery for hazard monitoring: Insights from Australia”. In: *Remote Sensing* 13.8 (2021), p. 1422.

[98] Évelyn Márcia Pôssa and Philippe Maillard. “Precise delineation of small water bodies from Sentinel-1 data using support vector machine classification”. In: *Canadian Journal of Remote Sensing* 44.3 (2018), pp. 179–190.

[99] Mission Actuelles En Télédétection Par Radar and Á Synthése. “The dark side of Remote Sensing: Current SAR Remote Sensing missions and applications”. In: ().

[100] Duraisamy Ramyachitra and Parasuraman Manikandan. “Imbalanced dataset classification and solutions: a review”. In: *International Journal of Computing and Business Research (IJCBR)* 5.4 (2014), pp. 1–29.

[101] John William Strutt Baron Rayleigh. *The theory of sound*. Vol. 2. Macmillan, 1896.

[102] Olaf Ronneberger, Philipp Fischer, and Thomas Brox. “U-net: Convolutional networks for biomedical image segmentation”. In: *Medical Image Computing and Computer-Assisted Intervention–MICCAI 2015: 18th International Conference, Munich, Germany, October 5-9, 2015, Proceedings, Part III 18*. Springer. 2015, pp. 234–241.

[103] Jagabandhu Roy et al. “A novel ensemble approach for landslide susceptibility mapping (LSM) in Darjeeling and Kalimpong districts, West Bengal, India”. In: *Remote Sensing* 11.23 (2019), p. 2866.

[104] Floyd F Sabins Jr and James M Ellis. *Remote sensing: Principles, interpretation, and applications*. Waveland Press, 2020.

[105] Collecte Localisation Satellites. *Masking ”No-value” Pixels on GRD Products generated by the Sentinel-1 ESA IPF*. 2018.

[106] Jürgen Schuol et al. “Modeling blue and green water availability in Africa”. In: *Water resources research* 44.7 (2008).

[107] Ghana Statistical Service. *Ghana statistics development project (GSDP) annual report*. 2016.

[108] Hossein Shafizadeh-Moghadam et al. “Google Earth Engine for large-scale land use and land cover mapping: An object-based classification approach using spectral, textural and topographical factors”. In: *GIScience & Remote Sensing* 58.6 (2021), pp. 914–928.

[109] Guozhuang Shen et al. “Water Body Mapping Using Long Time Series Sentinel-1 SAR Data in Poyang Lake”. In: *Water* 14.12 (2022), p. 1902.

[110] Shobitha Shetty. “Analysis of machine learning classifiers for LULC classification on Google Earth Engine”. MA thesis. University of Twente, 2019.

[111] James A Slater et al. “The SRTM data “finishing” process and products”. In: *Photogrammetric Engineering & Remote Sensing* 72.3 (2006), pp. 237–247.

[112] Andrea Tassi and Marco Vizzari. “Object-oriented lulc classification in google earth engine combining snic, glcm, and machine learning algorithms”. In: *Remote Sensing* 12.22 (2020), p. 3776.

[113] Ramon Torres et al. “GMES Sentinel-1 mission”. In: *Remote sensing of environment* 120 (2012), pp. 9–24.

[114] U.S. Geological Survey. *National Hydrography Geodatabase: Alaska.* 2013. URL: `ftp://ftp2.cits.rncan.gc.ca/pub/canvec/` (visited on 01/19/2024).

[115] M Krishna Satya Varma et al. “Pixel-based classification using support vector machine classifier”. In: *2016 IEEE 6th International Conference on Advanced Computing (IACC)*. IEEE. 2016, pp. 51–55.

[116] J-P Venot, Charlotte de Fraiture, and Ernest Nti Acheampong. “Revisiting dominant notions: a review of costs, performance and institutions of small reservoirs in sub-Saharan Africa.” In: *International Water Management Institute* (2012).

[117] Jean-Philippe Venot and Maija Hirvonen. “Enduring controversy: small reservoirs in sub-Saharan Africa”. In: *Society & Natural Resources* 26.8 (2013), pp. 883–897.

[118] Charles J Vörösmarty et al. “Global threats to human water security and river biodiversity”. In: *nature* 467.7315 (2010), pp. 555–561.

[119] Robert C Weih and Norman D Riggan. “Object-based classification vs. pixel-based classification: Comparative importance of multi-resolution imagery”. In: *The International Archives of the Photogrammetry, Remote Sensing and Spatial Information Sciences* 38.4 (2010), p. C7.

[120] William Wolberg et al. “Breast Cancer Wisconsin (Diagnostic)”. In: (1995).

[121] Iain H Woodhouse. *Introduction to microwave remote sensing*. CRC press, 2017.

[122] Lin Wu et al. “An improved method of algal-bloom discrimination in Taihu Lake using Sentinel-1A data”. In: *2019 6th Asia-Pacific Conference on Synthetic Aperture Radar (APSAR)*. IEEE. 2019, pp. 1–5.

[123] BK Wylie et al. “Surface water intra-and inter-annual dynamics in the Yukon Flats of Alaska”. In: *AGU Fall Meeting Abstracts*. Vol. 2006. 2006, B21C–1038.

[124] Lingbo Yang et al. “High-resolution rice mapping based on SNIC segmentation and multi-source remote sensing images”. In: *Remote Sensing* 13.6 (2021), p. 1148.

[125] Aiyeola Sikiru Yommy, Rongke Liu, and Shuang Wu. “SAR image despeckling using refined Lee filter”. In: *2015 7th International Conference on Intelligent Human-Machine Systems and Cybernetics*. Vol. 2. IEEE. 2015, pp. 260–265.

[126] Xiaoguang Yuan et al. “Feature Importance Ranking of Random Forest-Based End-to-End Learning Algorithm”. In: *Remote Sensing* 15.21 (2023), p. 5203.

[127] Matthew D Zeiler and Rob Fergus. “Visualizing and understanding convolutional networks”. In: *Computer Vision–ECCV 2014: 13th European Conference, Zurich, Switzerland, September 6-12, 2014, Proceedings, Part I 13*. Springer. 2014, pp. 818–833.

[128] Wen Zhang, Baoxin Hu, and Glen S Brown. “Automatic surface water mapping using polarimetric SAR data for long-term change detection”. In: *Water* 12.3 (2020), p. 872.

[129] Mingmin Zhao, Peder Olsen, and Ranveer Chandra. “Seeing through clouds in satellite images”. In: *IEEE Transactions on Geoscience and Remote Sensing* 61 (2023), pp. 1–16.

[130] Lei Zhou et al. “Machine learning comparison and parameter setting methods for the detection of dump sites for construction and demolition waste using the google earth engine”. In: *Remote Sensing* 13.4 (2021), p. 787.

A

Overview SAR Missions

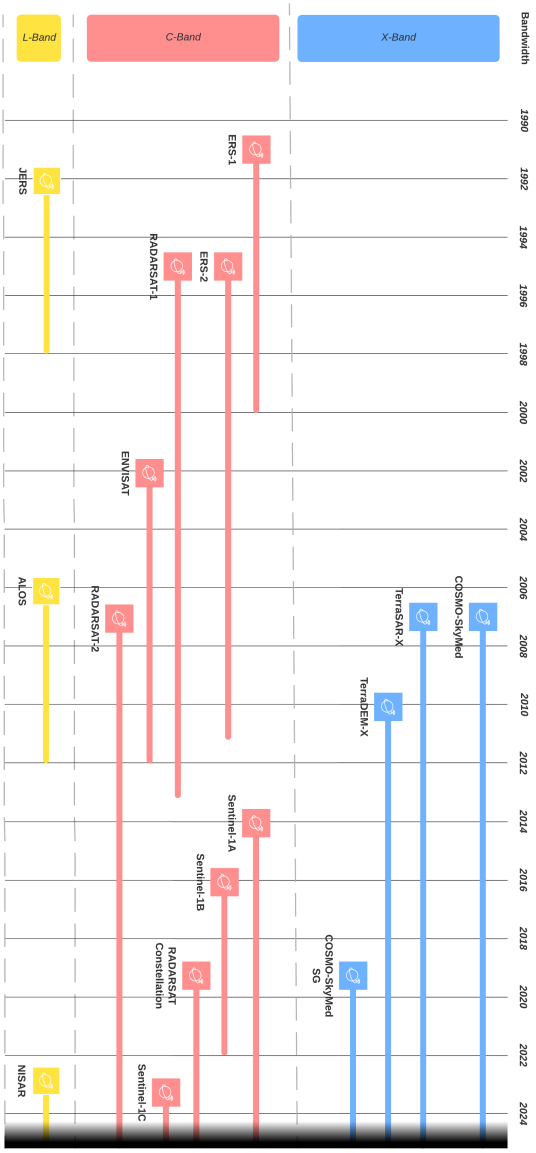

B

Conceptual Methodology

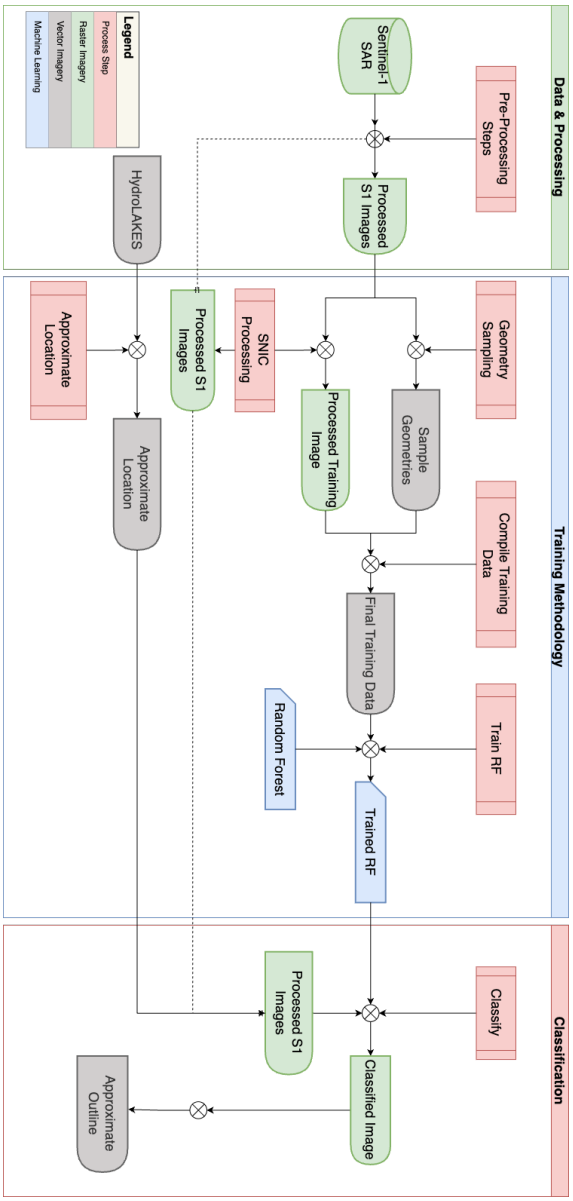

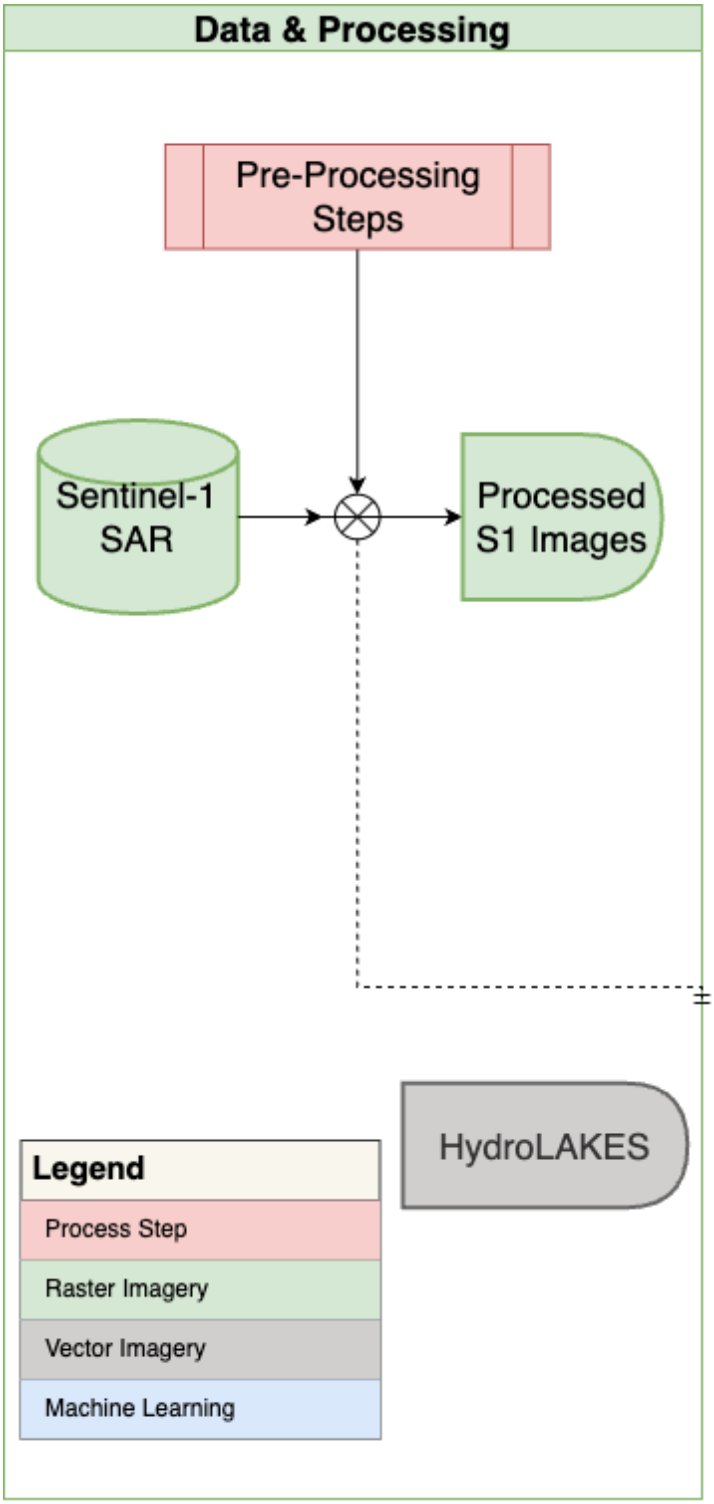
Data & Processing
Pre-Processing Steps
Sentinel-1 SAR
Processed S1 Images
HydroLAKES
Legend
Process Step
Raster Imagery
Vector Imagery
Machine Learning

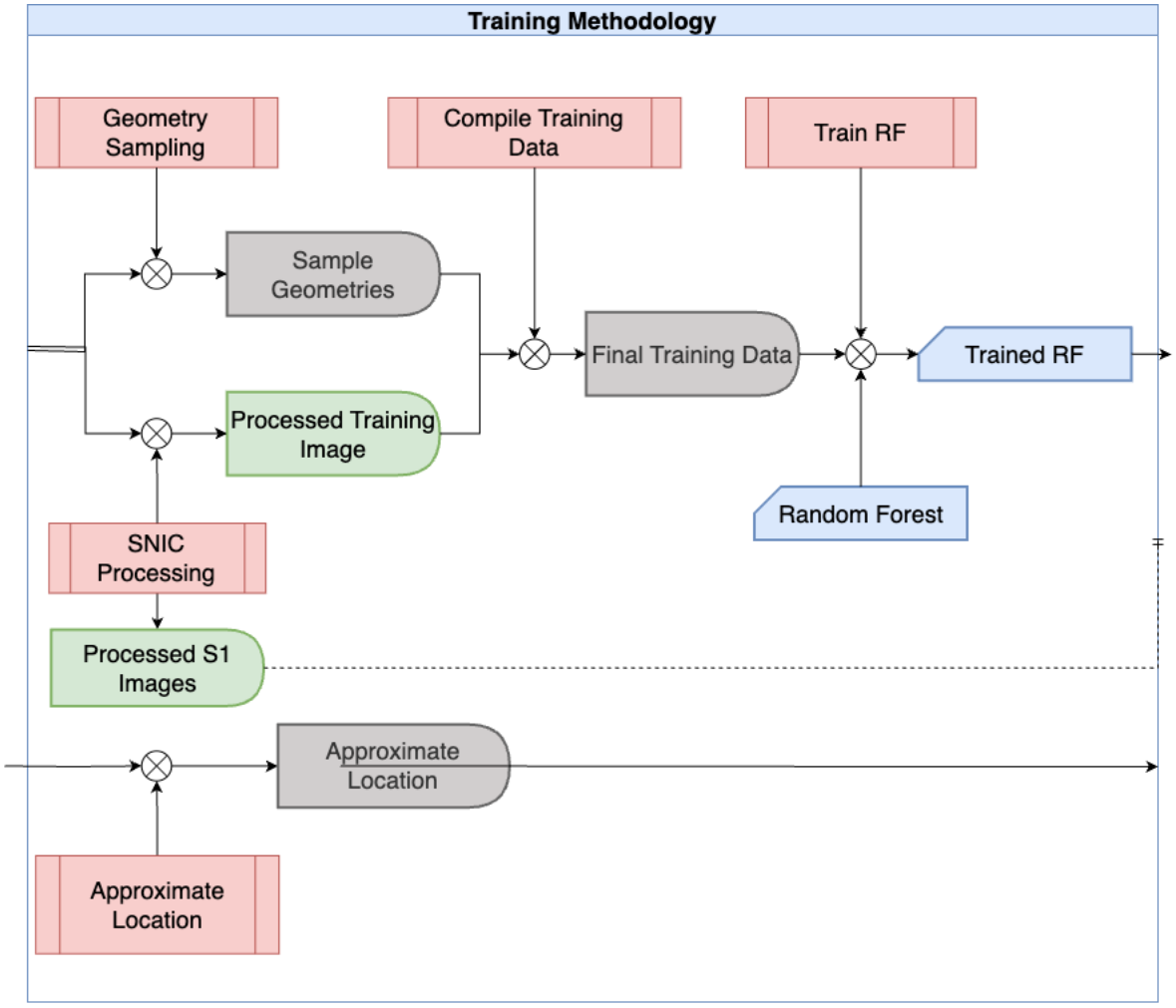
Training Methodology
Geometry Sampling
Compile Training Data
Train RF
Sample Geometries
Final Training Data
Trained RF
Processed Training Image
Random Forest
SNIC Processing
Processed S1 Images
Approximate Location
Approximate Location

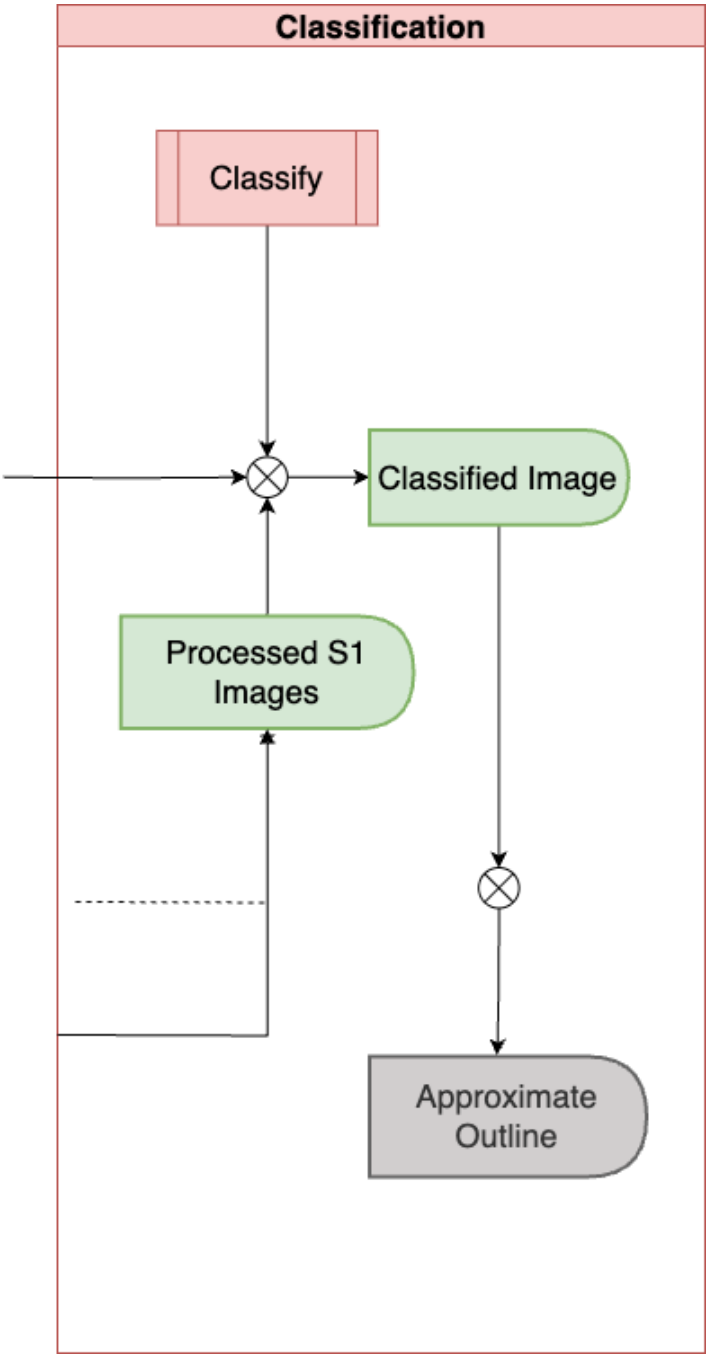
Classification
Classify
Classified Image
Processed S1 Images
Approximate Outline